Phase separation of polydisperse fluids

de Castro, Pablo

Awarding institution:
King's College London

Doctoral Thesis

Phase separation of polydisperse fluids

Pablo Souza de Castro Melo

Department of Mathematics

King's College London

A thesis submitted in fulfilment of the requirements for the degree of

Doctor of Philosophy

Supervisor

Professor Peter Sollich

May, 2019

Declaration of Authorship

I, Pablo Souza de Castro Melo, declare that this thesis titled, “Phase separation of polydisperse fluids” and the work presented in it are my own. I confirm that:

- This work was done wholly or mainly while in candidature for a research degree at this University.
- Where any part of this thesis has previously been submitted for a degree or any other qualification at this University or any other institution, this has been clearly stated.
- Where I have consulted the published work of others, this is always clearly attributed.
- Where I have quoted from the work of others, the source is always given. With the exception of such quotations, this thesis is entirely my own work.
- I have acknowledged all main sources of help.
- Where the thesis is based on work done by myself jointly with others, I have made clear exactly what was done by others and what I have contributed myself.

Abstract

The constituent particles of soft matter systems typically exhibit variation in terms of some attribute such as their size, charge, etc. Examples of these so-called "polydisperse" systems are everywhere, including colloids, liquid crystals, and polymers. Understanding the physical consequences of polydispersity, however, is a considerable challenge.

We explore qualitative aspects of polydisperse phase behaviour on two fronts. We first study the dynamics of phase separation in polydisperse colloidal systems by developing, analysing, and simulating a dynamical mean-field theory for the Polydisperse Lattice-Gas (PLG) model. In particular we test effects of fractionation, where mixture components are distributed unevenly across coexisting phases. Our results provide strong theoretical evidence that, due to slow fractionation, (i) dense colloidal mixtures phase-separate in two stages and (ii) the denser phase contains long-lived composition heterogeneities. We also provide a practical method to determine whether such heterogeneities are indeed present in a given phase-separating mixture.

Moreover, we study colloidal mixtures phase separating after a *secondary* temperature quench into the two- and three-phase coexistence regions. We found several interesting effects (mostly associated with the extent to which crowding effects can slow down composition changes), including long-lived regular arrangements of secondary domains; interrupted coarsening of primary domains; wetting of fractionated interfaces by oppositely fractionated layers; 'surface'-directed spinodal 'waves' propagating from primary domain interfaces; and filamentous morphologies arising out of secondary domains.

Secondly, we analyse the critical gas-liquid phase equilibrium behaviour of arbitrary fluid mixtures in the coexistence region, focussing on settings which are relevant for polydisperse colloids. Our analysis uses Fisher's complete scaling formalism and thus includes 'pressure mixing' effects in the mapping from the fluid's thermodynamic fields to the 3D Ising effective fields. Because of fractionation, the behaviour is remarkably rich. We give scaling laws for a number of new and conventional important loci in the phase diagram. In particular we identify new suitable observables for detecting pressure mixing effects. Our predictions are checked against numerics by using mapping parameters fitted to Lennard-Jones simulation data, allowing us to highlight crossovers where pressure mixing becomes relevant close to the critical point.

Acknowledgements

The acknowledgments and the people to thank are several. In particular, my supervisor Prof Peter Sollich for all wisdom, knowledge, true genius, and patience. Above all, my wife Jéssyca, my mother Zélia, my father Castro, my brother Tiago and my sisters Talita and Paloma. In hard times their support kept me walking. In the happiest times, however, we shared great joy. Not only them, but also my dear friends in Brazil, were constantly in my mind: Celé, Rafael, Cícero, and my Dillema mates, to name a few. I am also thankful to my second supervisor Dr Chiara Cammarota for the guidance and encouraging words, and to the Brazilian National Council for Scientific and Technological Development—CNPq—for the financial support (GDE No. 202399/2014-1). I thank my friends from my previous academic port, the Departamento de Física at UFPE in Recife, and particularly my Master's supervisor Fernando Parisio. "My" house in Manchester, where Chico, Débi, and João live, proved to be, as expected, a fortress of love, happiness, and music, which kept alive my best thoughts about home. My beloved friends in the UK, in particular in London, were responsible for making my life full of pleasant interactions and situations over these four years. I am extraordinarily grateful to Double Xote, the "forró pé-de-serra" band I joined with my Recife mates in London, and to ObáObá, the Brazilian party series that we have created here, and to everyone else we connected together through both. Thank you to the canteen's staff, in particular to Linda, for being such an incredible person, always very caring. My lunchtime all these years would not have been so good without you and our chats in Portuguese. Ryan, Edgar, Robin, and Davide, plus my other office mates, thanks for all the laughs, for each Beer Grand Prix, and for other kinds of help. I am very glad to have met many great people on the streets of London. All my love to them. You will always have a place to stay in Brazil.

Contents

List of Figures

List of Tables

Jéssyca, Zélia, Castro, Paloma, Talita e Tiago.

Chapter 1

Introduction

1.1 Polydisperse phase behaviour

Traditionally, thermodynamics and statistical mechanics deal with systems composed of identical particles, also called *monodisperse* systems. However, nature is often more complex: many soft matter systems, such as biological and industrial fluids (in the form of colloidal dispersions, liquid crystals, polymer solutions, etc.), are *polydisperse* in the sense that their constituent particles exhibit variation in terms of one (or several) attribute(s) [1–15]. This *polydisperse attribute*, denoted here by σ, can be particle size, shape, charge, molecular weight, chemical nature, etc. [16]. In the thermodynamic limit, these systems are usually regarded as having effectively an infinite number of *components* (although the theory that will be presented here applies to systems with an *arbitrary* number of components) [17,18]. Everyday and not-so-everyday examples include blood, paint, milk, clay, photonic crystals, shampoo, viruses, globular proteins, pharmaceuticals, and even sewage, among many others [19–28]. Therefore, understanding the impact of polydispersity on the **phase behaviour** of many-body systems is of fundamental, commercial, and practical interest [29]. For instance, knowing under what conditions (and how) a multicomponent fluid will demix may be essential in determining the shelf life of a product [30, 31]. On the fundamental end of the range, it is believed that (symmetry-breaking) phase transitions have occurred in the early universe via nucleation of vacuum-field bubbles, thus generating the different fundamental forces of nature; despite having a different sort of fluid dynamics and not being in the scope of the present work, it is interesting that the early-universe hot plasma can also be seen as a multicomponent fluid [32, 33]. Our focus here is on colloidal fluids,

for which the fluid particles are influenced by the thermal agitation from the solvent in which they are suspended, and quantum effects can be neglected. (See Ref. [34] for an introduction to polydisperse colloidal systems and their phase behaviour.)

The state of a polydisperse system (or any of its phases) is described by a density distribution $\rho(\sigma)$, defined such that $\rho(\sigma)d\sigma$ is the number density of particles with σ-values in the range $[\sigma, \sigma + d\sigma]$. One can also consider a multicomponent system, composed of a finite number M of particle species (each one labelled by its own value of σ). Each component has concentration p^α, with $\alpha = 1, 2, \ldots, M$. (Note that the α here is a superscript, not an exponent.) The continuous approach can be thought of as the limit $M \to \infty$, leading to $p^\alpha \to \rho(\sigma_\alpha)d\sigma$, where σ_α is the value of σ associated with species α. In either case, the system has an overall *composition*, which specifies the ratios of the densities of different species. The simplest example is the one of a binary system, i.e. $M = 2$: its composition could then be specified by the ratio p^A/p^B, for instance. We will often specialize to this binary case for ease of explanation.

Similarly to monodisperse fluids, polydisperse fluids can phase-separate into regions with higher and lower concentrations of particles. The typical experiment is to decrease the temperature of a homogeneous system to a value within the coexistence region, setting off a dynamical evolution towards separation into two (or more) equilibrium phases. (See Fig. 1.1 and the animation provided in the ESI—Electronic Supplementary Information—for our work in Ref. [35].) In polydisperse phase separation, however, these phases will not just differ in density but generally also in composition. This process is called *fractionation* (or *partitioning*) [17] because it implies that particles of different species distribute themselves unevenly into the new phases. Fractionation is responsible for much of the complexity in the phase behaviour of polydisperse systems [17, 36–38]; for instance, its effect on phase-separation kinetics will be one of our main focuses.

Let us explain fractionation in more detail using the $M = 2$ example. Fig. 1.2 shows a schematic example of a phase diagram of a binary fluid at a fixed temperature. The purple (middle) point indicates the species densities (p^A, p^B) of the *parent phase*, i.e. of the initial homogeneous system. Any other phase of the same composition would lie on the dashed line through the parent and the origin. This is called the *dilution line* because in a

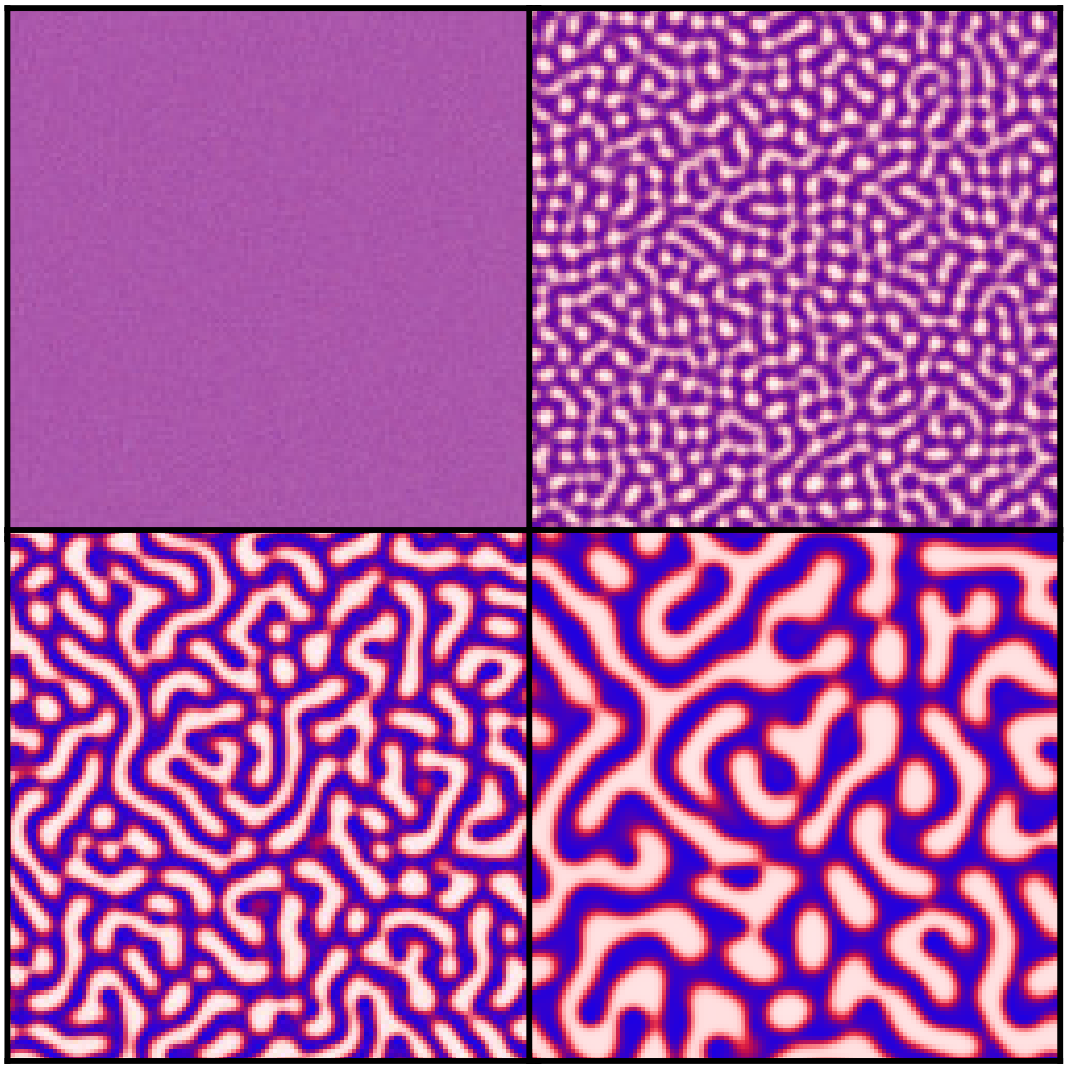

FIGURE 1.1: Phase separation snapshots (from top left to bottom right) for a binary mixture (generated with our equations)—see text for details, particularly Section 2.5.1.

colloidal fluid such phases can be prepared by adding or removing solvent.[1] Phase separation can occur into pairs of coexisting phases – identified from the requirements of equal pressure and species chemical potentials – that are shown as end points of tielines. Due to particle conservation, the overall system composition must remain unchanged during phase separation, so the actual *daughter phases* generated must lie on the tieline passing through the parent. In the generic case these daughter phases both lie off the dilution line so have a composition that is different from the parent (and from each other). This is the phenomenon of fractionation.

[1]Notice that $M = 2$ gives a binary mixture in the sense that there are two colloidal species, but it could also be thought as a 'ternary' system if one counts the solvent as a component. Nonetheless, we will keep the nomenclature based on the number of colloidal components only.

In the case of general M similar considerations apply. Here the parent is specified by a density distribution $\rho^{(0)}(\sigma)$. This can be decomposed as $\rho^{(0)}(\sigma) = \rho_0^{(0)} f^{(0)}(\sigma)$, where $\rho_0^{(0)} = N/V$ is the overall particle number density and $f^{(0)}(\sigma)$, the normalized parent shape function, specifies the composition. As $\rho_0^{(0)}$ is varied, $\rho^{(0)}(\sigma)$ traces out the dilution line in density distribution space. To obtain phase diagrams one needs to project from this M-dimensional space. Often only the density of coexisting phases is recorded, to recover the polydisperse analogue of a monodisperse density–temperature phase diagram (see Fig. 2.1).

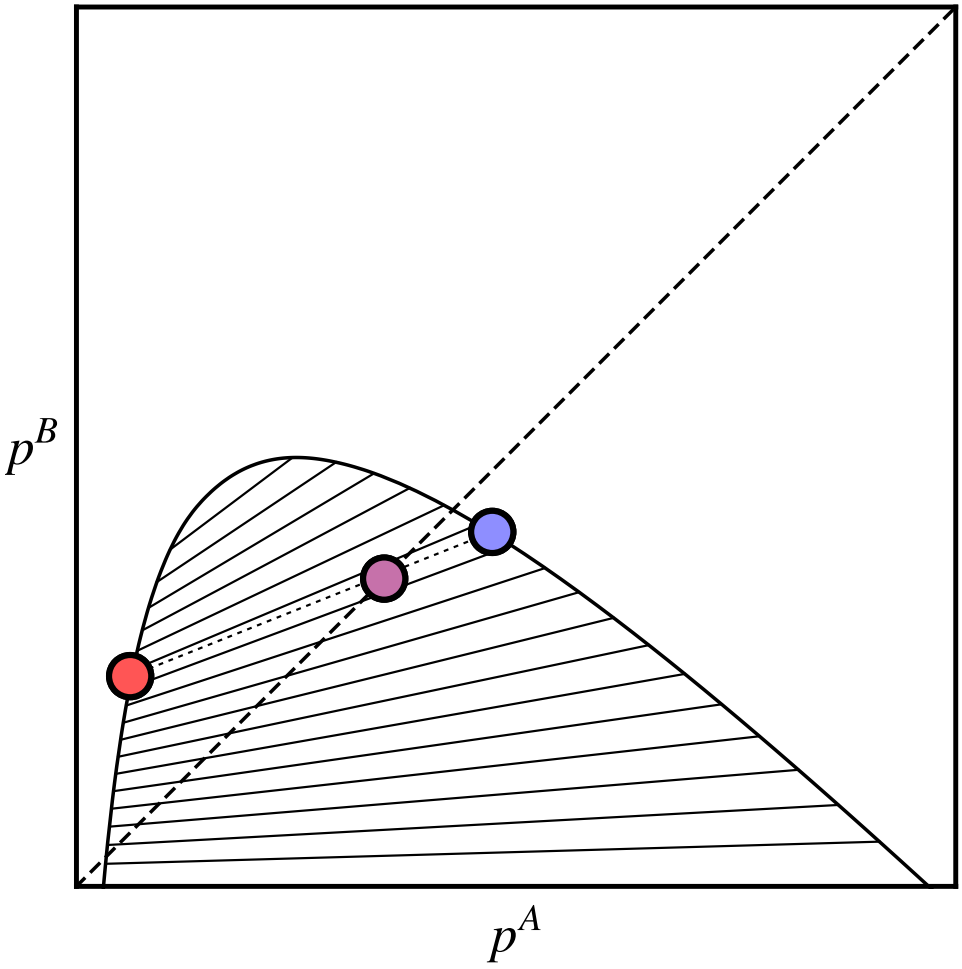

FIGURE 1.2: Sketch of a binary fluid phase diagram at fixed temperature. The purple (centre) point represents the parent phase. The points to the right and to the left (high- and low-density phases, respectively) are the two daughter phases. A *tieline* connects the daughter phases, defining the *equilibrium fractionation direction*; it passes through the parent phase. A number of other example tielines are shown. The end points of all tielines, taken together, form the boundary of the coexistence region.

Fractionation causes the equilibrium phase behaviour of polydisperse systems to be

much richer than that of their monodisperse counterparts [17]. To see why, note that for large M, the classical tangent plane procedure used to find phase coexistence from a given free energy becomes awkward both conceptually and computationally. Also, the number of coexisting phases allowed by Gibbs' phase rule grows with M, and becomes arbitrary in the limit $M \to \infty$. These challenges have been tackled using a number of theoretical methods, uncovering many qualitatively novel effects of polydispersity on phase behaviour. [17,39–41]. For instance, Evans has developed a perturbative approach for narrow distributions of the polydisperse attribute [16,37,42–44]. This predicts that the difference in mean particle size between the two daughter phases is proportional to the variance of the parent distribution. It can also predict specific trends, e.g. that in the fluid-solid coexistence of size-disperse colloidal hard spheres, the solid (crystalline) phase contains on average larger particles than the fluid [37]. Going beyond perturbative approaches, the full equilibrium phase diagram for polydisperse hard spheres has been found via accurate free energy expressions for the fluid and solid phases, showing very different equilibrium properties already for moderate particle size spreads [45]. The physical intuition behind this is the fact that particles of different sizes cannot easily fit into a regular crystal lattice. These results were derived using a moment projection method [17, 46–48]. This exploits a mapping of the full density distribution space onto *moment densities*, defined as $\rho_n \equiv \int \sigma^n \rho(\sigma) d\sigma$, where one integrates over all possible values of σ. Note that the zeroth moment density ρ_0 is just the overall density N/V. Another important parameter, the standard deviation of the polydisperse attribute σ normalized by its mean, can be expressed in terms of moment densities as $[(\rho_2\rho_0/\rho_1^2) - 1]^{1/2}$. It is often referred to as *degree of polydispersity* or simply *polydispersity*.

Having set out some of the basis issues in the physics of polydisperse fluids, we shall defer to the following thesis chapters a review of further literature and a discussion of more advanced concepts, including the notions of 'cloud' and 'shadow' curves, fractionation dynamics, and 'annealed' and 'quenched' spinodals.

1.2 Aim

The main aim of the present work is to explore the effects of polydispersity in the liquid-gas separation of fluid systems, particularly those in soft matter. In the context of nonequilibrium phenomena, this is done by using a simplified model of compressible colloidal fluids. Time-evolving properties such as the density for each component are determined in our analytical studies (early stages) and given by computational 'experiments' (early and late stages) performed to simulate the fluid's behaviour. When studying critical equilibrium properties that exist only in polydisperse systems, we analytically derive expansions near the critical point by mapping from known critical behaviour in the same universality class. Expansion coefficients can then be fitted to polydisperse equilibrium simulation data in the existing literature, allowing us to solve our equations numerically in order to verify our results.

Therefore my goal is to theoretically investigate how polydisperse systems progress towards equilibrium (predicting the importance of some nonequilibrium features to the equilibrium phase behaviour of real systems) and how their equilibrium properties are affected by the approach to a critical point.

The natural existence of model and time limitations implies that only a subset of all features of polydisperse phase behaviour that have previously been discussed in the literature can be further investigated in this thesis, but we will generally try to focus on the most important ones. This will be pointed out whenever appropriate.

1.3 Structure of the thesis

The remainder of this thesis is laid out as follows. In Chapter 2 we develop a dynamical theory for phase-separating polydisperse colloids; in particular we look at Warren's two-stage scenario proposal (see Section 2.1). To do so we use the Polydisperse Lattice-Gas model (Section 2.2), finding initially its mean-field phase diagram. This models gives a simplified description of polydisperse colloids (with either an arbitrary finite number of species or continuous polydispersity) by incorporating a hard-core repulsion combined with polydispersity in the strength of the attraction between neighbouring particles. We

provide general moment-based expressions for spinodals of two types (one that prohibits fractionation and one without this restriction) and the critical point. Numerical results for the 'cloud' and 'shadow' curves are shown. In Section 2.3 we develop our theory by setting up a kinetic model that includes two elementary processes: particle-solvent and particle-particle exchanges. We derive differential equations for the local evolution of species densities. Section 2.4 brings an analysis of the early-time spinodal dynamics and general moment-based expressions for the largest growth rates. We exemplify these for the case of bell-shaped polydisperse continuous distributions. In Section 2.5 we show our simulation results for the late-time dynamics obtained by numerical integration of the theory. We first look at the binary case and obtain new insights into phase separation dynamics of mixtures, in particular into the role of fractionation. Then we provide evidence that the features found are generic for arbitrary polydisperse systems, by obtaining qualitatively identical numerical results for three- and four-component systems, with the support of our general early-time analytical results. Section 2.6 summarizes the conclusions from this part of our work; Appendices 2.A and 2.B provide detailed derivations of some mathematical results.

In Chapter 3 we use the framework developed in Chapter 2 to investigate certain kinetic effects associated with slow composition changes. Going beyond the observations in Chapter 2, we turn the focus to more complicated situations, as explained in detail in Section 3.1. We start by showing how nonequilibrium features manifest themselves, and what their consequences are, in the context of phase separation via two-step temperature quenches (see Section 3.2). These insights are then connected to the similar behaviour of slab-like liquid domains surrounded by vapour (Section 3.3), where additional phenomena can be seen clearly. Finally, in Section 3.4 we show and discuss our simulations of phase separation with a second quench into the three-phase region. The chapter concludes with a summary and outlook in Section 3.5.

In Chapter 4 we move to the critical gas-liquid phase equilibrium behaviour of arbitrary fluid mixtures in the coexistence region, focussing on settings that are relevant for polydisperse colloids. Section 4.1 gives an overview of the relevant critical scaling results by reviewing the literature. In Section 4.2 we introduce the 'complete scaling' approach

used. This relates Ising 3D criticality to fluid criticality using expansions around the critical point in terms of the thermodynamic fields. Our results for the coexistence conditions and coexisting density distributions, in the context of the Ising-fluid mapping, are derived in Section 4.3. Then we present in Section 4.4 results for phase diagram lines with arbitrary constant fractional volume. These are less conventional but not less relevant, as we show. Section 4.5 brings a discussion of why the monodisperse case is different. The more conventional coexistence curves are discussed in Section 4.6, where new results are presented. In Section 4.7 we verify our results using expansion coefficients fitted to Lennard-Jones data. Conclusions and a thorough summary of the various new scaling laws are given in Section 4.8. Appendices 4.A–4.D contain mathematical derivations and numerical details, including a novel method that 'maps' systems with different numbers of species onto one another.

Finally, Chapter 5 draws conclusions based on the research carried out within the thesis, generally reviews the contributions that this thesis has made and discusses how this work can be extended in the future.

1.4 Previously published work

1. de Castro, P. & Sollich, P. (2017). "Phase separation dynamics of polydisperse colloids: a mean-field lattice-gas theory". Physical Chemistry Chemical Physics, 19, 22509-22527. Royal Society of Chemistry.

2. de Castro, P. & Sollich, P. (2018). "Critical phase behaviour in multi-component fluid mixtures: complete scaling analysis". The Journal of Chemical Physics, 149, 204902. American Institute of Physics.

Author contributions: PdC and PS conceived the studies. PdC and PS carried out the research, PdC developed the simulations, carried out the analytical calculations and prepared the figures. PdC and PS interpreted the data and shaped the study. All authors wrote and reviewed the manuscripts.

Published papers 1 and 2 cover the contents of Chapters 2 and 4.

Chapter 2

Phase separation dynamics of polydisperse colloids

2.1 Introduction

The present chapter focuses on the *dynamics* towards equilibrium. Warren proposed that the phase-separation kinetics in polydisperse systems should proceed in two stages [49]. To understand this two-stage scenario, he starts by considering an initially homogeneous system suddenly placed within a two-phase region. The classical picture predicts two types of phase-separation kinetics. If placed not too far from the phase boundary encompassing the two-phase region in the phase diagram, the system would phase-separate via *nucleation and growth*. However, if placed further away from the boundary phase separation would proceed via *spinodal decomposition*. Lying entirely below the coexistence curve, the classical spinodal curve separates the two types of kinetics. In the case of phase separation via spinodal decomposition, arbitrarily small fluctuations in the homogeneous system decrease the free energy, and thus grow exponentially before eventually being limited by nonlinear effects. Warren highlights the fact that, although the spinodal curve is a convention that does not rigorously survive in a correct statistical mechanical treatment, it is a rough guide to the transition region between the two types of kinetic behaviour. He proceeds by asking what the effect of polydispersity is on this classical picture. Assuming that in dense systems, fractionation is potentially a very slow process, he suggests that two stages of kinetics might be expected. In a first stage, the system might phase-separate by relaxing the overall density to a phase equilibrium dictated by 'quenching' (i.e.

'fixing') the polydisperse distribution in any phase to the one in the parent phase. Over longer timescales, the system might then gradually redistribute particles between coexisting phases to reflect the possibility of further lowering the free energy by fractionating. Therefore, a second stage would begin when the system started to significantly fractionate. Referring to the polydisperse density distribution as the size distribution, Warren says: 'During this slow process, the particle number density would be able to adjust itself continually to follow the current stage of the size partitioning process. The argument for this [two-stage] scenario is based on the observation that, *in a dense system*, the overall density can be much more easily relaxed by collective particle motion (collective diffusion), than can the size distribution be adjusted by individual particle rearrangements (self diffusion)' (p. 2199). Experimental measurements of self- and collective diffusion constants support this picture [50].

Warren's two-stage scenario is certainly physically reasonable: density fluctuations can be created by moving groups of particles 'in sync' to form regions of higher density. Fractionation, on the other hand, requires particles from different species to 'push past each other' in opposite directions. The scenario also makes an interesting connection to moment densities: the zeroth moment ρ_0, which gives the total number density of all species, should relax much more rapidly at a local level than the higher moments, whose equilibration requires interdiffusion of different particle species. This suggests that moment densities can remain useful in understanding the kinetics of phase separation, and our results in this chapter provide some support for this.

Existing theoretical approaches to polydisperse phase-separation dynamics have focussed primarily on polymeric systems. One can make some progress by binning the range of σ, which reduces the problem to the dynamics of a finite mixture. This approach of course becomes numerically challenging as the number of bins grows. Clarke has shown that the method is nonetheless useful for investigating the early-time phase-separation dynamics of polydisperse polymers [17, 51]. Again in the context of polymeric materials, Pagonabarraga and Cates developed an analysis of the dynamics based on time evolution equations for polymer densities driven by chemical potential gradients. The form of these equations had been proposed phenomenologically in Clarke's work, but the approach of

Ref. [52] allowed the associated mobility coefficients to be derived explicitly. Apart from the case of length polydispersity, where the results were more subtle, Pagonabarraga and Cates studied the case of chemical polydispersity, where different polymer chains have different monomer compositions and hence different interaction strengths. For this scenario the coupled dynamical equations could be fully solved in certain cases. Pagonabarraga and Cates [52] also studied the mode spectrum of the various density fluctuations in a system undergoing spinodal decomposition; from this analysis, they concluded that depending on where in the phase diagram the system is placed the kinetics will proceed in accordance with Warren's two-stage scenario.

Compared to the polymeric case, there is a lack of theoretical work designed to model fractionation effects in the phase-separation dynamics of spherical *colloids* (but see Ref. [42] discussed below). The present work is designed to fill this gap. The approach we use to investigate the phase-separation dynamics of mixtures is the theory described in Refs. [53] and [54] by Plapp and Gouyet. These studies were, however, concerned with *binary metallic alloys*. In this context they addressed rather different questions from ours, based on assumptions about the dynamics and the particle interactions that are quite distinct from the colloidal case. Nonetheless, our development of the mean-field dynamical equations has close similarities with the methods of Refs. [53] and [54].

There are a few other theoretical investigations of polydisperse colloidal dynamics in the literature, where simulations are implemented and some aspects of fractionation investigated [43, 55, 56]. As a result, the dynamics of phase separation in polydisperse colloids remains a challenging (and mostly unsolved) problem. One of the difficulties is that the kinetics of phase separation could be so slow as to make the actual equilibrium phase compositions unobservable in experiments [17]. It has been argued that this is the case for polydisperse hard-sphere crystals: once particles join to a crystal nucleus growing from the hard-sphere fluid, they essentially no longer diffuse on experimental timescales [42]. The size distribution of particles in the crystal will thus 'freeze in', and will be determined by the mechanism of crystal growth rather than the conditions of thermodynamic equilibrium. Although recent advances have been made [57], such non-equilibrium effects on the experimentally observed phase behaviour of colloidal systems are definitely not fully

understood.

In this chapter we present a mean-field theory for the Polydisperse Lattice-Gas (PLG) model, which has been proposed as a simple description of polydisperse colloids [36]. In Section 2.2 we present the model and its mean-field phase diagram. In Section 2.3 we endow the model with an appropriate dynamics and derive the mean-field evolution equations for this. Section 2.4 gives an early-time regime analysis of our equations. Then, in Section 2.5, we go beyond the spinodal regime and study the full late-time dynamics of our model. Section 2.6 summarizes our results and outlines some directions for future research.

2.2 PLG mean-field phase diagram

2.2.1 PLG model

Hereafter we use the PLG model to investigate the phase-separation dynamics in polydisperse colloidal systems [36]. The model is described by the Hamiltonian

$$H = -\sum_{\langle i,j\rangle}\sum_{\alpha,\beta}\sigma_\alpha\sigma_\beta n_i^\alpha n_j^\beta \tag{2.1}$$

where i runs over the sites of a periodic lattice $i = 1,\ldots,L^D$, assumed simple cubic and D-dimensional in this work, with lattice spacing $a = 1$, unless otherwise stated; the sum runs over all pairs $\langle i,j\rangle$ of nearest-neighbour sites; σ_α is the value of the polydisperse attribute associated with particle species α, which controls the strength of interparticle interactions; it is a positive number for attractive interactions as considered here. We consider a mixture with M species, with the summations over α and β therefore running from 1 to M. The (occupation) variable n_i^α simply counts the number of particles of species α at site i, for which a hard-core constraint is imposed:

$$\sum_{\gamma=0}^{M} n_i^\gamma = 1 \quad \forall i \tag{2.2}$$

where n_i^0 refers to *vacancy*, i.e. $n_i^0 = 1$ indicates the presence of a vacancy at site i, or, equivalently, a solvent particle. Note that the solvent particles are 'passive' [52] in this

framework, in such a way that any non-hydrodynamic effect caused by them has already been effectively included in the interaction between the particles as described by the model Hamiltonian. We also neglect the fact that colloidal particles may interact with one another via hydrodynamic interactions mediated by the solvent. We therefore use the term vacancy in the following, rather than solvent particle. Observe that n_i^0 can be expressed in terms of the other n_i^α, from Eq. (2.2). In summary, each lattice site may be either vacant or occupied by a single colloidal particle of polydisperse attribute σ_α. The instantaneous density distribution follows as $p^\alpha = L^{-D}\sum_i n_i^\alpha$. We will use the letter γ as the species index for summations running from 0 to M, while for summations running from 1 to M, we use α (or β), unless otherwise specified.

Note that in the Hamiltonian (2.1) the interaction strength between any two neighbouring particles is assumed to be $\sigma_\alpha\sigma_\beta$, i.e. the product of their polydisperse attributes, though to preserve generality we will often write this in the form $\varepsilon_{\alpha\beta} = \sigma_\alpha\sigma_\beta$. Thus the role of polydispersity in this model is to engender a spread of possible interaction strengths between particles, a situation which contrasts with the single interaction strength characterizing the simple Ising lattice-gas model. As observed in Ref. [36], this allows the PLG model to capture the essential qualitative features that distinguish polydisperse fluids from their monodisperse counterparts. Nonetheless one has to bear in mind that, in real colloids, polydispersity often occurs in the *size* of the particles. This will have additional consequences, e.g. on the local packing of particles in dense regions, that a lattice model cannot account for. In principle one could extend the approach by allowing particles to occupy several contiguous lattice sites, thus explicitly representing their size. This is not a trivial extension as particle moves would then correspond to simultaneous changes of potentially many n_i^α, but may be an interesting avenue for future work.

2.2.2 Mean-field phase diagram

We next present the mean-field phase diagram for the PLG model. This will serve as a useful reference point for our later discussion of the phase-separation dynamics. We first explain how to obtain the relevant curves of the diagram, starting from the spinodals and then moving on to the cloud ('binodal') and shadow curves.

Free energy and spinodals

Phase separation via spinodal decomposition occurs when the system is placed in a region of the phase diagram that is *unstable* to fluctuations; fluctuations of any size will then lead to phase separation. This contrasts with the case of nucleation and growth, where finite fluctuations – corresponding to a nucleus of a critical size – are required for the system to escape from a *metastable* state.

For the phase diagram of monodisperse systems, the spinodal curve (i.e. the curve below which spinodal decomposition occurs) can be calculated by joining up the inflection points of the free energy curve at each temperature. For the spinodal curve of a polydisperse system, one likewise needs to identify points where the free energy develops negative curvature.

In order to obtain an expression for the Helmholtz (inhomogeneous) free energy of the polydisperse lattice gas, $F = \langle H \rangle - TS$, we use a variational mean-field approximation. This is obtained from the Gibbs–Bogoliubov–Feynman variational bound [58, 59], using a variational approximation to the equilibrium distribution that is factorized over lattice sites. The latter is fully characterized by local densities $p_i^\alpha = \langle n_i^\alpha \rangle$. For the PLG Hamiltonian (2.1), this leads to

$$F = -\sum_{\langle i,j \rangle} \sum_{\alpha,\beta} \varepsilon_{\alpha\beta} p_i^\alpha p_j^\beta + T \sum_i \sum_{\gamma=0}^{M} p_i^\gamma \ln p_i^\gamma \tag{2.3}$$

where the Boltzmann constant has been set equal to 1. Recalling that the volume of the system is equal to the total number of sites ($V = L^D$) and applying Eq. (2.3) to a homogeneous configuration, the *free energy density* $f = F/V$ can be written as

$$f(\{p^\alpha\}, T) = -\frac{z}{2} \sum_{\alpha,\beta} \varepsilon_{\alpha\beta} p^\alpha p^\beta + T \sum_{\gamma=0}^{M} p^\gamma \ln p^\gamma \tag{2.4}$$

where z is the lattice coordination number [i.e. $z = 4$ for the square lattice (in $D = 2$)] and p^α is the overall density of particles of species α. Here the hard-core constraint (2.2) means that in the second, entropic term, $p^0 = 1 - \sum_\alpha p^\alpha$. For a monodisperse system (i.e. $M = 1$), the free energy density reduces to a function $f = f(\rho, T)$, where $\rho = N/V \equiv p^1$ is the overall density of particles. Here and in the following we drop the 0-subscript from

our previous notation ρ_0 where the meaning is clear from the context. (Confusion with the density distribution $\rho(\sigma)$ should not arise as this is always written with its polydisperse attribute argument σ.) In this monodisperse case, the spinodal density at any temperature T would be found from the equation $\frac{\partial^2 f}{\partial \rho^2} = 0$. In the more general, polydisperse, case one needs to consider the Hessian matrix S with elements

$$S_{\alpha\beta} = \frac{\partial^2 f}{\partial p^\alpha \partial p^\beta} \tag{2.5}$$

and then solve the equation $\det(S) = 0$ (or the equivalent spinodal criterion as written in Ref. [48]) to obtain the spinodal curve.

For polydisperse systems, one can, in the spirit of Warren's two-stage scenario, define two types of spinodals [49]. The first is the *annealed* spinodal curve, which is precisely the one given by $\det(S) = 0$. For the PLG model, this leads to a simple expression in terms of the moment densities:

$$T = z\left(\rho_2 - \rho_1^2\right). \tag{2.6}$$

The *quenched* spinodal curve, on the other hand, is defined as the spinodal curve that is calculated by assuming that the system is *not* allowed to fractionate. In other words, one treats the composition as fixed, and the overall density ρ as the only variable. To calculate this, note that the free energy given by Eq. (2.4) is a function of all densities p^α. At fixed composition these are proportional to the overall density ρ, e.g. for $M = 2$ one would have $p^A = p^B = \rho/2$ if the dilution line $p^A/p^B = 1$ is considered. Inserting these ρ-dependencies into the free energy gives the quenched free energy, as a function of ρ; call this $f_Q(\rho, T)$, for example. To find the quenched spinodal one then only has to solve $\frac{\partial^2 f_Q}{\partial \rho^2} = 0$, which in our case yields

$$T = z\left(\frac{\rho_1}{\rho}\right)^2 \left(\rho - \rho^2\right). \tag{2.7}$$

One can easily check that this coincides with Eq. (2.6) for monodisperse systems, where $\rho_2/\rho = (\rho_1/\rho)^2$.

The above distinction between two types of spinodal will prove useful later because, if Warren's two-stage scenario holds, one would expect that the dynamics of phase separation would proceed, at least initially, as if the system 'did not know' it could further

lower its free energy by fractionating. Therefore, one could expect that the early-stage dynamics of a system operating in the two-stage scenario should proceed in accordance with the quenched spinodal instead of the annealed one.

For completeness we note that the critical point lies on the (annealed) spinodal curve and is identified by an additional condition. This can be obtained using the methods of Ref. [48] and reads $2\rho_1^3 - 3\rho_1\rho_2 + \rho_3 = 0$.

Cloud and shadow curves

Because of fractionation, the conventional vapour-liquid binodal (or coexistence curve) of a monodisperse system splits into a *cloud curve*, marking the onset of (polydisperse) phase coexistence, and a *shadow curve*, giving the density of the incipient phase. The critical point appears at the intersection of these curves, rather than at the maximum of either [17]. This splitting is seen in experiments on polydisperse fluids (see e.g. Ref. [60]). Similarly to the spinodal curve, we can define annealed and quenched cloud curves. These will be distinct because the onset of phase coexistence will be delayed to lower temperature if the system is not allowed to lower its free energy by fractionation.

Our numerical data for cloud and shadow curves are determined by solving the equations for two-phase (bulk) phase equilibrium. (Three-phase coexistence can also occur in the PLG, but at lower temperatures than we consider here. See Section 3.4.) In the binary case ($M = 2$), the phase equlibrium conditions at given T are equality of the chemical potentials μ^A, μ^B and the pressure between the two phases $(p_{\mathrm{I}}^A, p_{\mathrm{I}}^B)$ and $(p_{\mathrm{II}}^A, p_{\mathrm{II}}^B)$. Here the chemical potentials μ^A and μ^B are given by the partial derivatives of the free energy density $f(p^A, p^B, T)$ with respect to p^A and p^B, respectively, and the pressure is $P = -f + \mu^A p^A + \mu^B p^B$. For $M > 2$, the generalization is straightforward, giving $M + 1$ coexistence equations to solve. (Alternatively, one could use the moment free energy method, since our free energy density (2.4) is *truncatable* [48].) The cloud temperature for a given parent density is found by lowering T and checking when phase coexistence with the parent as one of the coexisting phases first occurs. The shadow curve identifies the density of the second coexisting phase, which at this point is present only in an infinitesimal fraction of the system volume. In a monodisperse system, cloud and shadow curve

coincide and are then identical to the conventional binodal curve.

Phase diagram

Fig. 2.1 shows our results for the phase diagram of a binary mixture. We chose the dilution line $p^A = p^B$ and σ-values given by $\sigma_A = 1 + d$ and $\sigma_B = 1 - d$, where d is a number between 0 and 1. (Note that the greater the d, the greater the polydispersity in this bidisperse case.) The plot shows the annealed cloud and shadow curves, with the critical point at their intersection; the quenched binodal curve; and the annealed and quenched spinodal curves. Qualitatively these curves look as one would expect them to on general grounds [17].

For our discussion of phase-separation dynamics most relevant are the cloud curve as it signals the onset of phase coexistence, and the spinodal curve. The annealed and quenched versions of each of these two curves divide the phase diagram into distinct regions where Warren's hypothesis predicts different sequences of phase-separation dynamics. Inside the quenched spinodal, the system should initially phase-separate by spinodal decomposition in density only; between the quenched spinodal and quenched binodal the first stage should be nucleation and growth of density fluctuations. The second stage would then involve fractionation, again by spinodal decomposition or nucleation and growth depending on the position relative to the annealed spinodal.

As an example, Fig. 2.2 shows a zoomed-in portion of the phase diagram. Starting at $\rho = 0.5$ and moving towards higher densities at constant temperature $T = 0.94$, one visits four distinct regions with respect to the annealed and quenched cloud and spinodal curves. Labelling these by R1, R2, R3, R4 with increasing density gives the predictions in Table 2.1, where we have used the term 'size' generically to refer to the polydisperse attribute σ. In this chapter we develop a mean-field theory that excludes stochastic fluctuations and therefore does not capture nucleation and growth dynamics. Hence we will focus on the distinction between different spinodal regions, i.e. region R1 versus R2/R3. Note that we will use the term 'early-time dynamics' throughout to refer to the onset of phase-separation dynamics, irrespective of the relevant time scale. In particular, in region R2/R3 the early-time dynamics should be stage 2 spinodal decomposition, which happens on a slow time scale because it involves fractionation.

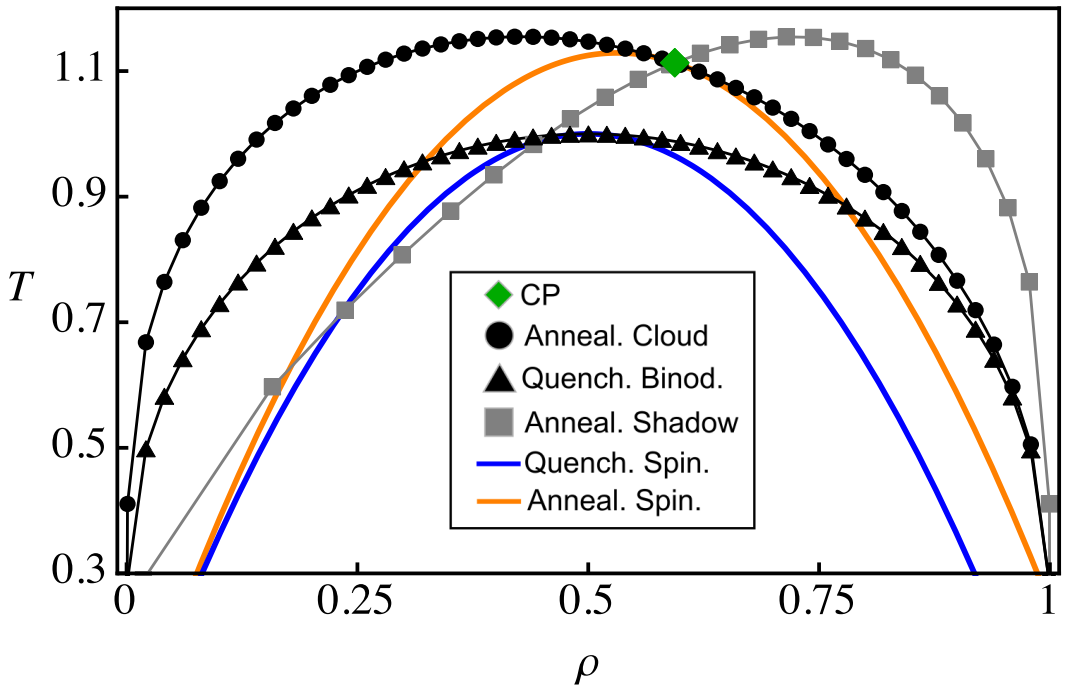

FIGURE 2.1: Phase diagram of a binary PLG mixture for $d = 0.25$ and dilution line $p^A = p^B$. (CP stands for Critical Point.) These choices allow all the relevant qualitative features to be seen clearly.

Region	Stage 1	Stage 2
R1	SD in density	SD of 'sizes'
R2	NG of density fluctuations	SD of 'sizes'
R3	————	SD of 'sizes'
R4	————	NG of 'size' fluctuations

TABLE 2.1: Abbreviations: SD = Spinodal Decomposition; NG = Nucleation and Growth.

2.3 Kinetic PLG model

In this section we present the kinetics that we assume for the PLG model with an arbitrary number of species M, and derive our mean-field dynamical equations.

We model the dynamics as resulting from jumps of particles to nearest-neighbour sites. This can be described in the general form of a master equation

$$\frac{\partial P(C,t)}{\partial t} = \sum_{C'} \left[W(C',C)P(C',t) - W(C,C')P(C,t) \right] \tag{2.8}$$

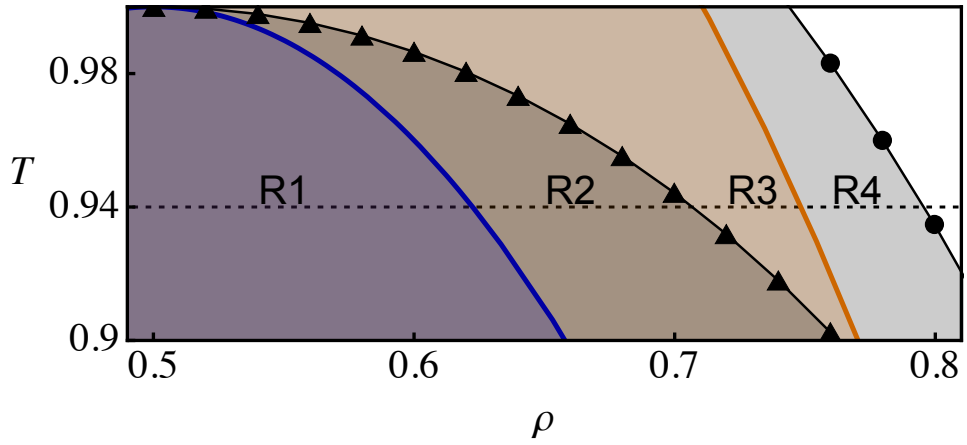

FIGURE 2.2: Zoomed-in portion of the phase diagram in Fig. 2.1. Starting at $\rho = 0.5$ and moving towards higher ρ along a reference horizontal dotted line (at $T = 0.94$), one visits four distinct phase coexistence regions with respect to the positions of the cloud/binodal and spinodal curves. According to Table 2.1, each of these regions corresponds to a distinct dynamical behaviour.

where $P(C,t)$ is the probability of finding the system in a configuration

$$C = \{n_i^1, n_i^2, \ldots, n_i^M; i = 1, \ldots, L^D\}$$

at time t, and $W(C,C')$ is the transition rate from a configuration C to another one C'. One can then define a time-dependent average for any observable $Q(C)$ as

$$\langle Q \rangle(t) = \sum_C Q(C) P(C,t) \tag{2.9}$$

In particular we define a time-dependent local density for each species as $p_i^\alpha(t) = \langle n_i^\alpha \rangle(t)$. From the master equation it can be shown that each species follows a conservation law of the form

$$\frac{dp_i^\alpha}{dt} = -\sum_{j \in \partial i} J_{ij}^\alpha \tag{2.10}$$

where we have introduced the notation $j \in \partial i$, meaning that the summation has to be performed over all nearest-neighbour sites j of site i; the current of α-particles across the link $i \to j$ is given by

$$J_{ij}^\alpha = \sum_{\gamma=0}^{M} \left\langle n_i^\alpha n_j^\gamma w_{ij}^{\alpha\gamma} - n_j^\alpha n_i^\gamma w_{ji}^{\alpha\gamma} \right\rangle \tag{2.11}$$

where $w_{ij}^{\alpha\gamma}$ is the *jump rate* for an α-particle at site i to exchange positions with a γ-particle

at site j (or with a vacancy, if $\gamma = 0$). Observe that, effectively, we are considering a kinetic model equipped with two elementary processes: (i) the jump of a particle from an occupied lattice site to an empty one, and also (ii) the direct interchange between two particles from arbitrary species. In each of these processes, the configuration of the system changes, but the overall number of particles of each species remains constant, which is the physical origin of the conservation law (2.10). It is worth noting that the physical elementary processes are the jumps to empty sites, i.e. particle-vacancy exchanges (a particle is not expected to actually cross through the inside of another). However, for the subsequent analysis it is useful to include also direct particle-particle swaps, so that we develop the theory initially for generic $w_{ij}^{\alpha\gamma}$.

Note that the prefactors of $w_{ij}^{\alpha\gamma}$ in Eq. (2.11) ensure the target site is occupied by a γ-particle (or empty, if $\gamma = 0$) and the start site is occupied by an α-particle. This is similar to the theory described by Plapp and Gouyet in Ref. [53], but there they did not consider direct interchange of particles, and the number of species M was set equal to 2 (as previously mentioned); moreover, they considered Arrhenius law jump rates, which was argued to be more suitable in their context of phase separation in binary metallic alloys. Here, we use Glauber-like jump rates:

$$w_{ij}^{\alpha\gamma} = w^{\alpha\gamma}\left[\frac{1}{1+\exp\left(\Delta H_{ij}^{\alpha\gamma}/T\right)}\right] \tag{2.12}$$

where $\Delta H_{ij}^{\alpha\gamma} = H(C') - H(C)$ is the energy difference associated with the jump, i.e. it is the energy difference between the configuration before the jump (C), in which there is an α-particle at site i and a γ-particle at site j, and after the exchange (C'); note that C and C' are identical except for the exchange between α and γ. The prefactor $w^{\alpha\gamma}$ is an 'attempt rate'. This gives the actual jump rate $w_{ij}^{\alpha\gamma}$ when the energy change $\Delta H_{ij}^{\alpha\gamma}$ is large and negative, while it is reduced exponentially for large positive energy changes.

Let us write the energy of the system for the configuration before the jump, isolating only the contributions involving the two particles α and γ that are swapping:

$$H(C) = -\varepsilon_{\alpha\gamma} - \sum_{\beta}\sum_{k\in\partial i\setminus j}\varepsilon_{\alpha\beta}n_k^{\beta} - \sum_{\beta}\sum_{l\in\partial j\setminus i}\varepsilon_{\gamma\beta}n_l^{\beta} + \ldots \tag{2.13}$$

Here the first term on the right-hand side is the contribution only from the interaction between the two particles that are swapping. The second term is the contribution from the interactions between the α-particle at site i and all of its neighbours except the one at site j. The third term similarly accounts for the interactions of the γ-particle. Similarly, we have that

$$H(C') = -\varepsilon_{\alpha\gamma} - \sum_{\beta} \sum_{k\in\partial i\setminus j} \varepsilon_{\gamma\beta} n_k^{\beta} - \sum_{\beta} \sum_{l\in\partial j\setminus i} \varepsilon_{\alpha\beta} n_l^{\beta} + \dots \tag{2.14}$$

is the energy of the system after the exchange. The energy change is then

$$\Delta H_{ij}^{\alpha\gamma} = \sum_{\beta} \left(\sum_{k\in\partial i\setminus j} \varepsilon_{\alpha\beta} n_k^{\beta} - \sum_{l\in\partial j\setminus i} \varepsilon_{\alpha\beta} n_l^{\beta} \right) - \sum_{\beta} \left(\sum_{k\in\partial i\setminus j} \varepsilon_{\gamma\beta} n_k^{\beta} - \sum_{l\in\partial j\setminus i} \varepsilon_{\gamma\beta} n_l^{\beta} \right). \tag{2.15}$$

We now invoke a mean-field approximation to evaluate the currents (2.11). In this we neglect fluctuations of $\Delta H_{ij}^{\alpha\gamma}$, i.e. we replace this quantity by its average. This can be justified by thinking about a high-dimensional limit, where the number of nearest neighbour sites z of any lattice site is large enough for the local 'fields' appearing in $\Delta H_{ij}^{\alpha\gamma}$ to average out fluctuations. In the same spirit we also drop the restrictions on the sums in $\Delta H_{ij}^{\alpha\gamma}$, which only changes the local fields by a relative amount $1/z$. It then only remains to perform the average of the kinetic prefactors, which with a mean-field decoupling becomes $\langle n_i^{\alpha} n_j^{\gamma} \rangle \approx p_i^{\alpha} p_j^{\gamma}$. Inserting the resulting approximation for the currents into (2.10), we obtain the mean-field kinetic equations

$$\frac{dp_i^{\alpha}}{dt} = -\sum_{j\in\partial i} \sum_{\gamma=0}^{M} \left[\frac{p_i^{\alpha} p_j^{\gamma} w^{\alpha\gamma}}{1+\exp\left(\langle \Delta H_{ij}^{\alpha\gamma} \rangle / T\right)} - \frac{p_j^{\alpha} p_i^{\gamma} w^{\alpha\gamma}}{1+\exp\left(\langle \Delta H_{ji}^{\alpha\gamma} \rangle / T\right)} \right] \tag{2.16}$$

where – within the mean-field approximation –

$$\langle \Delta H_{ij}^{\alpha\gamma} \rangle = \sum_{\beta} \left(\sum_{k\in\partial i} \varepsilon_{\alpha\beta} p_k^{\beta} - \sum_{l\in\partial j} \varepsilon_{\alpha\beta} p_l^{\beta} \right) - \sum_{\beta} \left(\sum_{k\in\partial i} \varepsilon_{\gamma\beta} p_k^{\beta} - \sum_{l\in\partial j} \varepsilon_{\gamma\beta} p_l^{\beta} \right). \tag{2.17}$$

These kinetic equations are – in spite of the rather different method of derivation – consistent with the mean-field free energy (2.3) in the sense that they always decrease it over time, $dF/dt \leq 0$. (This consistency is what requires the approximation step we have taken above, of dropping the restrictions on the sums defining $\Delta H_{ij}^{\alpha\gamma}$ [61].) This is as one would

expect in a closed system, where there are no currents crossing boundaries [54]. We defer the derivation of the result dF/dt to Appendix 2.A, which generalizes similar derivations discussed elsewhere in the literature [54] to include the case of direct particle-particle swapping.

From the fact that $dF/dt \leq 0$ it follows that the dynamics leads to a state which minimizes the mean-field free energy. This final state may be the ground state (global minimum) or a metastable state (local minimum). The monotonic decrease of the free energy also implies that the mean-field kinetic equations cannot describe nucleation events. Capturing these would require introducing fluctuations, e.g. by adding Langevin noise to our deterministic Eqs. (2.16). (This is further discussed in Section 2.6.)

2.4 Early-time spinodal dynamics

In this section, we will present a linearized version of our theory: it describes the growth of small fluctuations around an initial homogeneous state (via spinodal decomposition), within the framework of our mean-field kinetic equations. It will be shown that the maximum spinodal growth rates can be expressed in terms of only three moments of the polydisperse distribution. More importantly, we will use the result for the spinodal growth rates to test Warren's two-stage hypothesis.

We begin by considering a homogeneous system of overall composition described by a list of densities: $\{p^\alpha \mid \alpha = 1,\ldots,M\}$. The system is perturbed by small fluctuations of the densities:

$$p_i^\alpha = p^\alpha + \delta_i^\alpha \tag{2.18}$$

where $\delta_i^\alpha \ll 1$. As shown in Appendix 2.B, linearization of (2.16) leads to the following equation:

$$\frac{d\delta_i^\alpha}{dt} = \sum_{\gamma=0} \mathcal{M}^{\alpha\gamma}\Delta_{\mathrm{d}}\left(\mu_i^\alpha - \mu_i^\gamma\right) \tag{2.19}$$

where we define the *homogeneous mobilities* as

$$\mathcal{M}^{\alpha\gamma} \equiv \frac{w^{\alpha\gamma}}{2T} p^\alpha p^\gamma \tag{2.20}$$

We have also introduced the local chemical potentials $\mu_i^\alpha = \partial F / \partial p_i^\alpha$. These are given explicitly by

$$\mu_i^\alpha = -\sum_{j\in\partial i}\sum_\beta \varepsilon_{\alpha\beta} p_j^\beta + T \ln\left(p_i^\alpha / p_i^0\right) \tag{2.21}$$

for $\alpha = 1,\ldots,M$, while $\mu_i^0 = 0$. These expressions are derived from the free energy expression (2.3) with the explicit substitution $p_i^0 = 1 - \sum_\alpha p_i^\alpha$. Finally in Eq. (2.19) we use the *discrete Laplacian* Δ_d, which is defined by

$$\Delta_\mathrm{d} g_i = \sum_{j\in\partial i} (g_j - g_i) \tag{2.22}$$

for any site-dependent quantity g.

Note that, so far, the theory applies for completely generic attempt rates $w^{\alpha\gamma}$. Furthermore, if these attempt rates are set such that the right-hand side of Eq. (2.19) contains only the particle-vacancy term (i.e. no direct interchanges of particles are allowed), and one considers only the $M = 2$ case, then Eq. (2.19) has the same form as Eq. (27) in Plapp and Gouyet's work [54]. The only difference is that their expression for the homogeneous mobility is different from (2.20), as Plapp and Gouyet used Arrhenius jump rates. Their choice reflects the physical assumption for alloys that the elementary particle moves have an energy barrier effectively equivalent to removing a particle from the system. For the colloidal case Glauber rates are rather more plausible.

To solve the linearized mean-field equations, one exploits that a homogeneous system is invariant under translation with respect to the lattice vectors. Solutions are therefore superpositions of time-dependent Fourier modes

$$\delta_j^\alpha = \delta p^\alpha \exp\left[i\mathbf{k}\cdot\mathbf{x}_j + \omega t\right] \tag{2.23}$$

(as will be clear, the i in the exponents refers to the imaginary unit $i \equiv \sqrt{-1}$). Here $\mathbf{k}$ is the fluctuation wave vector and $\mathbf{x}_j$ is the position vector in real space of lattice site j. Moreover, ω is the *growth rate* of the mode and δp^α indicates the amplitude of the fluctuation associated with species α. By inserting Eq. (2.23) into (2.19) one finds an eigenvalue equation with eigenvalue ω, with the δp^α being the components of the corresponding

M-dimensional eigenvector. [See Eq. (2.49) in Appendix 2.B.] Thus we have a stability spectrum with M branches. A branch can be stable (ω is negative for all wave vectors) or unstable, with ω being positive in some range of $|\mathbf{k}|$, typically for small $|\mathbf{k}|$. We will be interested in the *maximum growth rate* $\omega_{\max}$ over all branches and wave vectors, which identifies the dominant growing fluctuation mode. Outside of the spinodal region this maximum growth rate becomes zero because the system is stable to all small fluctuations there.

To be able to evaluate the maximum growth rate we need to make specific assumptions about the attempt rates $w^{\alpha\gamma}$. We will set $w^{\alpha 0} = w_0$ and $w^{\alpha\beta} = w_s$, for any $\alpha \neq 0$ and $\beta \neq 0$, where w_0 and w_s are constant attempt rates associated with particle-vacancy and particle-particle exchanges, respectively. (The '0' subscript is for vacancy, and the 's' is for *swapping*.) In principle, one could imagine that $w^{\alpha\beta}$ might not be the same for all pairs α and β, or that it depends on the temperature. However, our simple choice for the values of $w^{\alpha\gamma}$ is enough to distinguish between particle-vacancy and particle-particle kinetic mechanisms. Moreover, we will see later that the dependence on temperature would be irrelevant for our purposes. Also, Plapp and Gouyet say in Ref. [54] that, in their case with particle-vacancy dynamics only (where $M = 2$ and Arrhenius rates are used), numerical results indicate that qualitative phase-separation behaviour is unaffected by the attempt rate ratio w^{A0}/w^{B0} as long as it is not too far from unity.

For the above choice of $w^{\alpha\gamma}$ we show in Appendix 2.B that the (largest branch of) growth rates can be expressed as

$$\begin{aligned}\omega = \frac{A(\mathbf{k})}{4T}&\left\{T\left[(2-\rho)w_0 + w_s\rho\right] - (A(\mathbf{k})+z)\left[w_0(1-\rho)\rho_2 + w_s\left(\rho\rho_2 - \rho_1^2\right)\right]\right\} \\ &- \frac{A(\mathbf{k})}{4T}\Big[\left(T(w_0-w_s)\rho\right)^2 + (A(\mathbf{k})+z)^2\left(w_0(1-\rho)\rho_2 + w_s\left(\rho\rho_2-\rho_1^2\right)\right)^2 \\ &+2T(w_0-w_s)(A(\mathbf{k})+z)\left(w_0(1-\rho)\left(\rho\rho_2-2\rho_1^2\right) + w_s\rho\left(\rho\rho_2-\rho_1^2\right)\right)\Big]^{1/2}\end{aligned} \tag{2.24}$$

where $A(\mathbf{k})$ is essentially the Fourier transform of the Laplacian. Equation (2.24) is valid for any spatial dimension given the appropriate expression for $A(\mathbf{k})$, with e.g. for a two-dimensional lattice $A(\mathbf{k}) = -4\sin^2(k_x a/2) - 4\sin^2(k_y a/2)$. The moment densities in the above expressions are, in the discrete representation, $\rho_n = \sum_\alpha \sigma_\alpha^n p^\alpha$.

In the monodisperse limit ($M = 1$), expression (2.24) does not depend on w_s. This of course should be so as swaps between identical particles do not change the system configuration and hence cannot contribute to the dynamics. To find the maximum growth rate, one needs to maximize ω with respect to $\mathbf{k}$. As in the regime of interest the maximum occurs for small wavevectors, this can be done by expanding ω as a function of $\mathbf{k}$ around $|\mathbf{k}| = 0$ up to the fourth order in $|\mathbf{k}|$, and then maximising the resulting expression analytically. One can also carry out numerically the maximization of the full $\omega(\mathbf{k})$, with essentially indistinguishable results (see Figures 2.3a and 2.6a), but we use the expansion procedure to obtain a closed-form expression for $\omega_{\max}$. (This is nonetheless too long to be displayed here.)

Because of the moment structure of (2.24), our linear theory can be applied to a fully polydisperse (i.e. $M \to \infty$) system, using an experimentally-reasonable distribution like the Schulz-Gamma form [62]

$$f^{(0)}(\sigma) = \frac{1}{g!}\left(\frac{g+1}{\bar{\sigma}}\right)^{g+1} \sigma^g \exp\left[-\left(\frac{g+1}{\bar{\sigma}}\right)\sigma\right]. \tag{2.25}$$

In the following we set the mean interaction strength $\bar{\sigma} = 1$ as we did in the binary case. The parameter g controls the polydispersity of the distribution, which is given by $1/\sqrt{g+1}$. This means that e.g. the choice $g = 15$ produces a standard deviation of σ that is 25% of the mean. With these choices, the moments appearing in the growth rates (2.24) can be expressed in terms of the density as $\rho_1 = \bar{\sigma}\rho = \rho$, $\rho_2 = \bar{\sigma}^2\rho[1 + 1/(g+1)] = \rho(g+2)/(g+1)$. Note that because only moments up to second order appear in our mean-field spinodal rates, other distributions with the same mean and variance would give identical results.

Let us now see what our linear theory says about Warren's scenario as applied to the spinodal dynamics. Fig. 2.3a shows the maximum growth rate as a function of the overall density, for reasonably dense systems. Here and in the following we fix the overall timescale by setting $w_0 = 1$. The vertical lines indicate the upper limits of the annealed and quenched spinodal regions, respectively. As expected, the maximum growth rate becomes zero beyond the annealed spinodal, where the system is stable to all density fluctuations. More remarkable is that the maximum growth rate increases only very slowly as density is

decreased below this point, and only begins to rise substantially at the *quenched* spinodal. This is exactly in line with what would be expected from Warren's two-stage hypothesis: inside the quenched spinodal region, the system has fast (stage 1) spinodal dynamics driven by the instability with respect to density fluctuations. (This corresponds to region R1 in Table 2.1.) Outside the quenched spinodal, on the other hand, there is no spinodal decomposition in stage 1 (corresponding to regions R2/R3) and the spinodal dynamics is produced by the much slower growth of composition fluctuations in stage 2. To the extent that stage 2 dynamics, which involves local fractionation, is slow compared to stage 1, $\omega_{\max}$ should therefore be small between quenched and annealed spinodals, as compared to its values inside the quenched spinodal region. This is exactly what we find.

Graphically, the above reasoning means that $\omega_{\max}(\rho)$ should have a kink at the quenched spinodal, where it crosses over from small (stage 2) to large (stage 1) values. The situation in Fig. 2.3a is quite close to such an ideal two-stage scenario. The kink can be seen more clearly by looking at the *second derivative* of $\omega_{\max}$ with respect to ρ, which would be large around a kink. Fig. 2.3b shows that this second derivative does indeed have a maximum, and this is positioned close to, if not exactly at, the quenched spinodal density. Note that this happens even though our calculation of $\omega_{\max}$ did at no point involve any restriction to quenched dynamics, i.e. fixed composition. In other words, the full, unrestricted dynamics of the system nonetheless 'feels' the presence of the quenched spinodal. This provides strong support for Warren's two-stage scenario.

Since the physics of Warren's two-stage scenario requires the system to be *dense*, we expect it to break down at lower densities. To check this, we first investigate the behaviour of $\omega_{\max}(\rho)$ around the *lower* end of the spinodal region. In Fig. 2.4, it is clear that the second derivative does not have any signatures around the (lower) quenched spinodal density, instead increasing smoothly towards the annealed spinodal. Secondly, returning to the kink in $\omega_{\max}$ at the upper quenched spinodal density, we can consider its dependence on temperature. At higher temperatures, the upper spinodal densities become lower, so that the two-stage scenario should be less pertinent. To check this, we show in Fig. 2.5 the density where the maximum in the second derivative of $\omega_{\max}$ occurs, for a range of temperatures. We can see that the density at the maximum moves away from the quenched

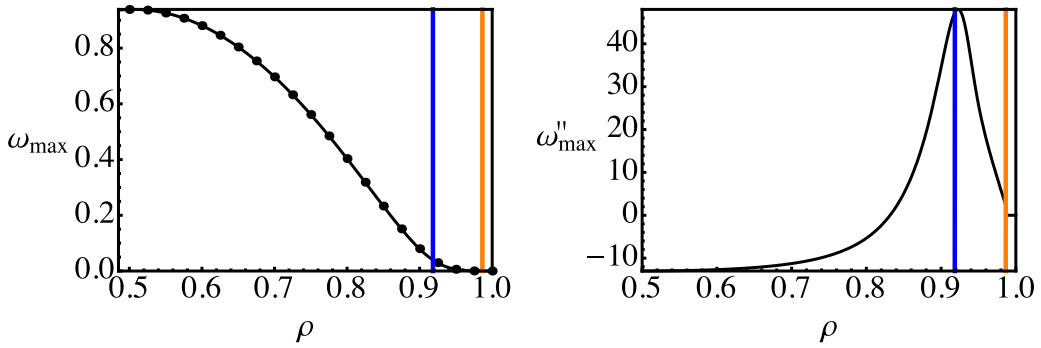

(A) (B)

FIGURE 2.3: (a) $\omega_{\max}$ as function of ρ for $T = 0.3$, $g = 15$ (standard deviation: 25% of the mean), and $w_s = 0$. The vertical lines indicate the (upper) quenched and annealed spinodal densities, from left to right. For comparison, we show the points obtained by numerically maximising $\omega(\mathbf{k})$ and the curve obtained analytically from small-$|\mathbf{k}|$ expansion; these agree very well. (b) Second density derivative of $\omega_{\max}$ as function of ρ. The vertical lines are the same as in (a). Note that $\omega_{\max}$ almost has a kink at the quenched spinodal density, as indicated by the maximum in the second derivative.

spinodal curve and towards the annealed spinodal as T increases, as expected. More usefully, we can read off from the figure that the two-stage scenario gives a good account of the position of the kink for densities above $\rho \approx 0.9$, so for the given polydispersity this is the threshold where the system becomes sufficiently dense to make fractionation slow.

We now perform a second test that detects directly whether the behaviour we are seeing – namely the near-kink in $\omega_{\max}(\rho)$ – is in fact due to fractionation being slow. We do this by turning on direct particle swaps, using a nonzero swap attemp rate w_s. Fractionation is then possible even in dense systems, without relying on mediation by rare vacancies. The signatures of the two-stage scenario that we have found should therefore disappear as we increase w_s. Indeed, Fig. 2.6 shows that for $w_s = 0.5$, $\omega_{\max}$ increases smoothly as density is decreased from the annealed spinodal, rather than remaining small until the quenched spinodal. Likewise the second derivative of $\omega_{\max}(\rho)$ is now featureless around the quenched spinodal and simply increases gradually towards its value at the annealed spinodal. Essentially, this is evidence that the two-stage scenario has been destroyed.

So far we have focussed on a system with fixed polydispersity of 25%. As Warren's argument does not rely on specific features of the σ-distribution, one would however expect qualitatively similar results also for other polydispersities. To assess this quantitatively

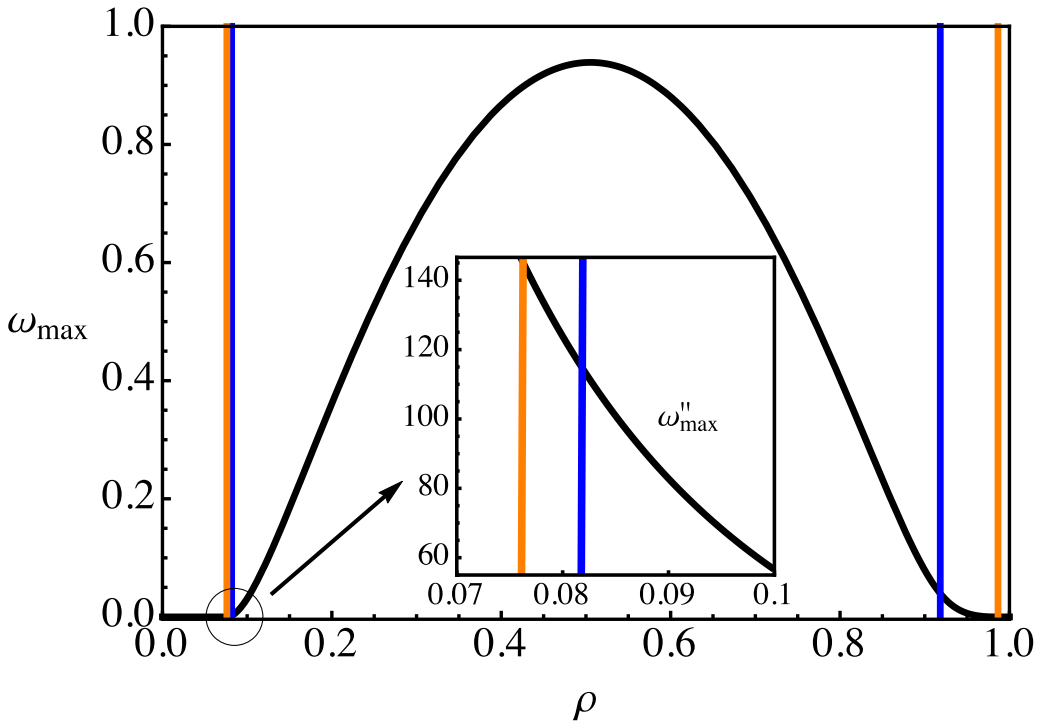

FIGURE 2.4: Behaviour of ω_{max} across the full density range, for the same parameters as in Fig. 2.3. The inset shows that the second derivative of ω_{max} shows no special feature at the lower quenched spinodal density, where fractionation is too fast for Warren's two-stage scenario to apply.

one needs to account for the fact that the separation in density between quenched and annealed spinodals grows with polydispersity. This can be done by considering the density difference between the maximum of ω''_{max} and the quenched spinodal, normalized by the difference between the annealed and quenched spinodal densities. When this ratio is $\ll 1$, the kink of ω_{max} is close to the quenched spinodal as the two-stage scenario predicts. Upon varying temperature, density and polydispsersity we find (data not shown) that the ratio is indeed dependent mostly on density and largely independent of polydispersity, becoming small at high densities as it should.

Summarizing the discussion in this section thus far, our mean-field theory for the spinodal dynamics of polydisperse colloids provides strong support for Warren's two-stage hypothesis, in the appropriate regime of high densities. It is worth noting that previous support for the two-stage scenario, both in Warren's original paper [49] and in the study by Pagonabarraga and Cates [52], was obtained in the context of polymers, whereas here we have polydispersity in the interaction strength in a context that is more easily connected

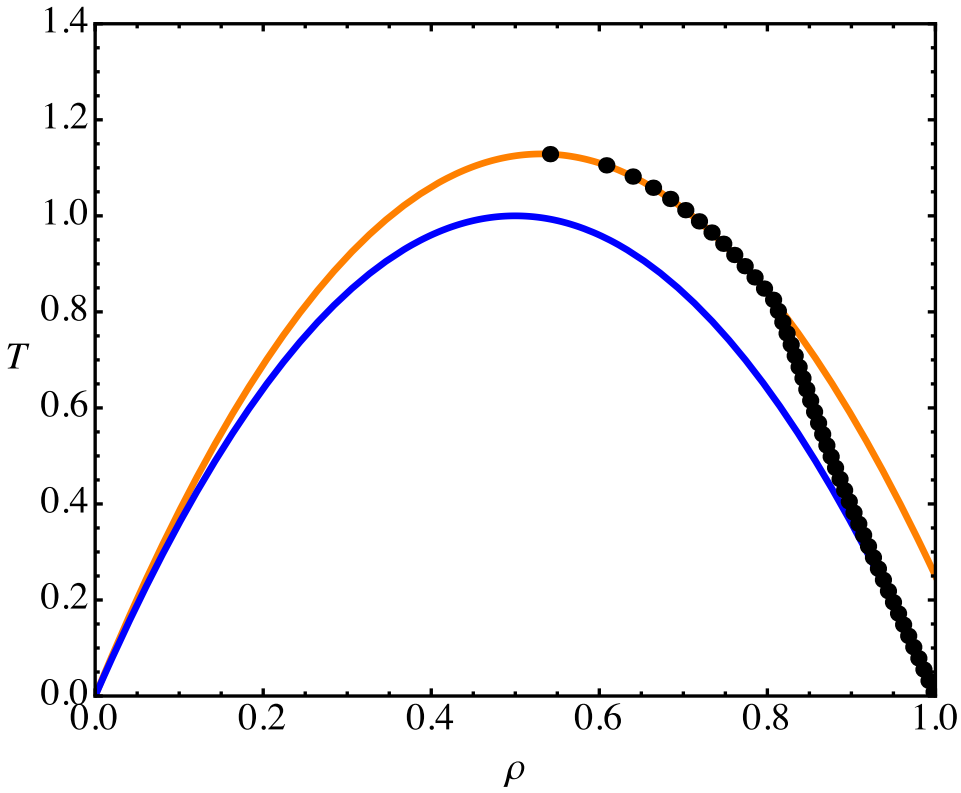

FIGURE 2.5: Position of the maximum of the second derivative of $\omega_{\max}$, shown on the x-axis, versus temperature on the y-axis (points). Other parameters as in Fig. 2.3. The curves give the quenched (lower curve) and annealed (upper curve) spinodals. Note that the second derivative maximum agrees closely with the quenched spinodal throughout the high density (above $\rho \approx 0.9$) region.

with the physics of colloids. This indicates that Warren's scenario may be a general feature of the non-equilibrium dynamics of dense fluid mixtures.

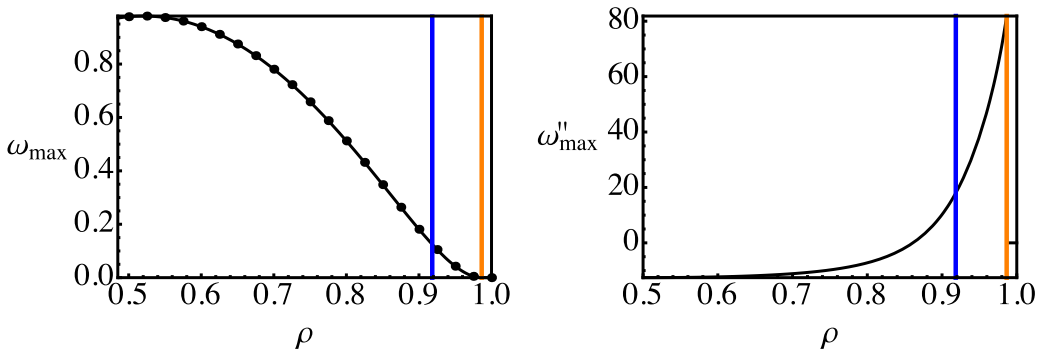

(A) (B)

FIGURE 2.6: As Fig. 2.3, but for $w_s = 0.5$. Note that the maximum in the second density derivative of $\omega_{\max}$ is now at the annealed spinodal density.

We next briefly discuss the temperature dependence of the maximum growth rates, returning to the physical value $w_s = 0$. The maximum growth rates are then directly proportional to w_0. So far we have taken constant $w_0 = 1$, though the results of Fig. 2.5 would remain the same for any temperature-dependent w_0: this is because we always consider the second derivative $\omega''_{\max}$ with respect to density, at fixed temperature. With constant w_0, we find that the typical maximum growth rates (say, in the middle of the spinodal region) increase towards low temperatures as $\sim 1/T$. This temperature dependence comes from the use of Glauber rates: linearizing the factors of $\exp(\Delta H/T)$, with energy changes from particle moves that are of temperature-independent magnitude, gives a factor of $1/T$ in all growth rates. For quantitative modelling of spinodal growth rates one would therefore want to choose a w_0 that goes to zero as $T \to 0$, e.g. $w_0 \sim T$, which would be consistent with the picture of an underlying diffusive dynamics causing attempted particle moves. This would then give constant maximum growth rates for low T.

We conclude this section with a discussion of the amplitudes δp^α of the mode that grows fastest in the spinodal dynamics, with rate $\omega_{\max}$. These amplitudes define the relative strength of density fluctuations for each species. As a vector in density space, they identify the early-time (non-equilibrium) fractionation direction, or simply *spinodal direction*. As discussed above, combining Eqs. (2.19) and (2.23) leads to an eigenvalue equation with eigenvalue ω, and the δp^α are the M components of the eigenvector corresponding to $\omega_{\max}$. This eigenvector can be calculated by solving the eigenvalue equation numerically, or one can derive a closed-form expression in terms of ω, ρ, and the attempt rates. We will denote the angle between the spinodal direction and the dilution line by $\theta_{\max}$. This quantity is of interest because in an ideal two-stage scenario, it should be zero inside the quenched spinodal region, where the initial dynamics corresponds to stage 1, i.e. pure density fluctuations; it should then rise as one moves from the quenched spinodal density to the annealed one, where the spinodal dynamics corresponds to stage 2. Our numerical data for $\theta_{\max}(\rho)$ (not shown) follow this scenario fairly closely in dense systems, providing further support for Warren's hypothesis. As our system is not ideal in the sense that fractionation is not infinitely slow, we find inside the quenched spinodal region a $\theta_{\max}$ that is constant but not quite zero, indicating that even in stage 1 the dominant spinodal mode

contains a fractionating component in addition to pure density fluctuations. Likewise the transition to larger values of $\theta_{\max}$ is not a sharp kink but a crossover, though importantly this remains located around the quenched spinodal density. As in the case of $\omega_{\max}$, we have tested that when direct particle swaps ($w_s > 0$) are introduced, this crossover disappears and is replaced by a featureless increase of $\theta_{\max}$ across the entire annealed spinodal region. This confirms that the crossover in the physical system ($w_s = 0$) arises from fractionation being a slow process.

2.5 Beyond the spinodal regime

In order to see what happens after the end of the spinodal regime, and hence investigate the full phase-separation dynamics, we integrate our mean-field kinetic Eqs. (2.16) numerically using a forward Euler method, with periodic boundary conditions. The method returns the evolution of the local densities for all species. For ease of visualization and reduction of computation time, spatial dimension $D = 2$ was chosen. Firstly, we examine what happens for binary mixtures ($M = 2$), and then extend the analysis to $M > 2$. We set the jump attempt rates as before, i.e. $w^{\alpha 0} = w_0$ and $w^{\alpha\beta} = w_s$, for any $\alpha \neq 0$ and $\beta \neq 0$. More specifically we concentrate on the physical setting $w_s = 0$, unless otherwise stated. To find the evolution of a system whose overall composition is given by a list of densities $\{p^\alpha \mid \alpha = 1, \ldots, M\}$, we firstly created an initial homogeneous state defined by $p_i^\alpha = p^\alpha$ for all sites i. To trigger the phase separation, we added small fluctuations to the initial state of each species by generating L^D random numbers, normally distributed, with mean zero and standard deviation 1%. We then subtracted the average of these random numbers, to ensure that the overall density of every species remains unchanged. The time step used was limited by the numerical stability of the algorithm, and typically equal to 0.1; we checked that this value is small enough to give us effectively the solution of the continuous-time equations by running the numerics for exactly the same initial configuration with a time step smaller by a factor of 5 and verifying that the results were virtually the same. When we used 50×50 lattice sites and $M = 2$, for instance, our program (written in C) performed $8,000$ time steps in approximately 100 seconds (running at 2.6 GHz processor speed), which in many instances was enough time to grow relatively large domains.

2.5.1 Binary fluids

Fig. 2.7 shows snapshots of the phase-separation dynamics for $M = 2$, with $\sigma_A = 1 + d$ and $\sigma_B = 1 - d$. For these binary case numerics we chose $d = 0.25$. Thus the first and second moment densities (normalized by ρ), i.e. ρ_1/ρ and ρ_2/ρ, are the same as in the continuous distribution analysis presented in Section 2.4, where the Schulz parameter was $g = 15$; also, the same temperature $T = 0.3$ was used. Therefore the spinodal growth rates are also the same as in the fully polydisperse case and we expect, at a given density ρ, to see a very similar initial dynamics. We chose $\rho = 0.82$, which places the system within the quenched spinodal region. To determine the colour of a site i, we used a colour scheme in which the colours red, green, and blue are blended together. The intensity of each of these colours at a given site varies from 0 to 1. In our scheme, red, green, and blue intensities are given exactly by $1 - p_i^A, p_i^0, 1 - p_i^B$, respectively. (Remember the notation for the local concentration of vacancies, i.e. $p_i^0 = 1 - p_i^A - p_i^B$.) This leads to the colour key shown in the top-left part of Fig. 2.7. It is plotted in triangular colour space in $(p^A, p^B, 1 - p^A - p^B)$, dropping the site index i. For example, if the concentration of particles of species A at one site is high (low), and the concentration of particles of species B at the same site is low (high), then the site colour will tend towards blue (red); if the concentrations of all species are all low, then the site colour will tend to white.

The snapshots in Fig. 2.7 show the growth of lighter regions of the system that represent gas bubbles. These bubbles are surrounded by a B-rich (red) interface separating them from an A-rich (blue) continuous liquid phase. Walking from the centre of a gas bubble along an arbitrary direction, one therefore initially sees low concentrations of both particle types, then a high concentration of the particle species with the smallest σ, i.e. B-particles, and eventually one reaches the bulk liquid that contains predominantly A-particles, for which σ is the largest. (Video showing the full-time evolution of the phase separation process is provided as an animation in the ESI for Ref. [35].)

Of course as we decrease ρ our numerical results show larger vapour fractions. Changing ρ can also lead to more complicated morphologies such as in Fig. 1.1, which was generated using $T = 0.4$, $p^A = p^B = 0.33$, $d = 0.3$, $w_s = 0$, $L = 128$, with the last snapshot taken at $t = 6000$. Because the value of ρ here is closer to the critical density one observes

bicontinuous domains of gas and liquid. The intuition is the same as in a one-species Ising lattice-gas system, where because of the particle-hole (vacancy) symmetry, in a system at the critical density neither gas or liquid can 'win' to form bubbles or droplets. Instead, finger-like bicontinuous structures are formed. Moving away from the critical point, one expects these to survive for a certain time until the system 'notices' which phase is going to be the majority phase, and forms bubbles or droplets of the minority phase.

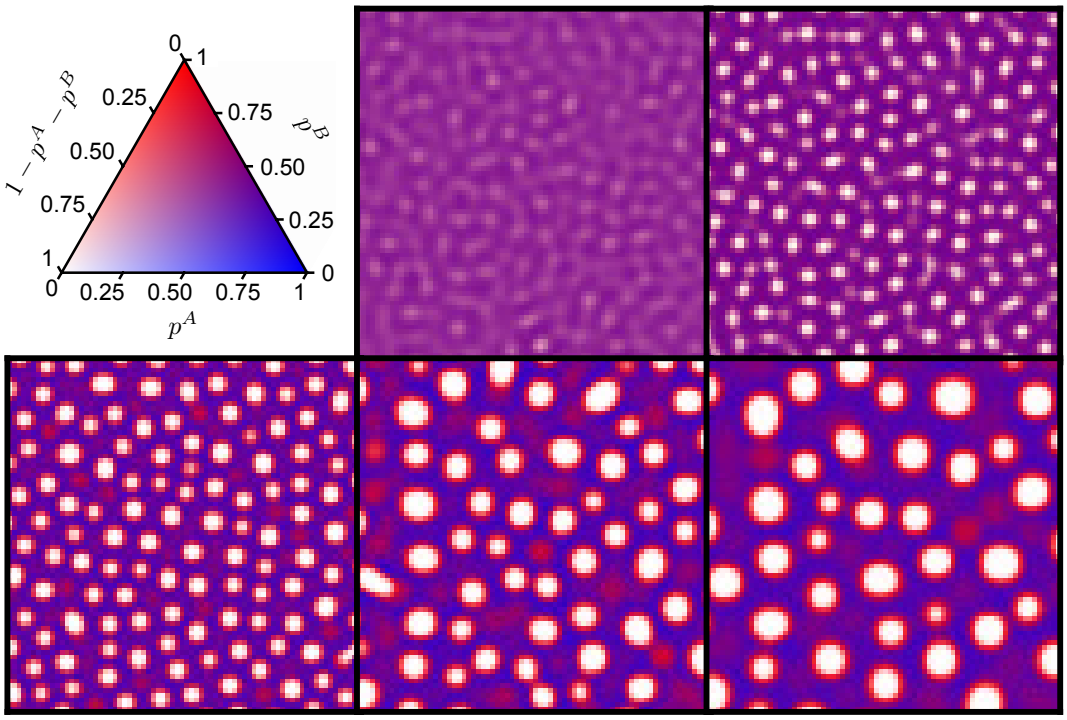

FIGURE 2.7: Time snapshots showing the local compositions throughout the system, as from numerics. The colour scheme is based on the RGB colour model, leading to the colour key shown in the top-left corner; see text for details. The lighter portions of the system are gas bubbles, which are surrounded by a B-rich interface separating them from an A-rich continuous liquid phase. Parameters: $p^A = p^B = 0.41$, $T = 0.3$, $d = 0.25$, $w_s = 0$, and $L = 150$. (Only a 75×75 region of the system is shown here.) From top centre to bottom right, the snapshots are taken at $t = 8$, 16, 316, 4850 and 16200.

In Figs. 2.8 and 2.9 we introduce a different representation of the time evolution that will prove to be quite revealing. We show two-dimensional *density histograms*, in species density space, i.e. in the (p_i^A, p_i^B)-plane that contains all the possible density combinations an arbitrary site i can have; the physically accessible region in this plane is a triangle bounded by $p_i^A \geq 0$, $p_i^B \geq 0$ and $p_i^A + p_i^B \leq 1$. What the histogram counts is the number of lattice sites i that have species densities (p_i^A, p_i^B) inside each two-dimensional bin. The results were normalized by the total number of lattice sites L^D. Such a density histogram can

then be viewed as a dynamic analogue of an equilibrium phase diagram as sketched in Fig. 1.2 above. In a density histogram, the parent phase lies on the dilution line (shown dashed in Figs. 2.8 and 2.9) as before. The low- and high-density daughter phases calculated from the equilibrium phase diagram lie off this dilution line, with the parent on the connecting tieline; the latter defines the equilibrium fractionation direction. At the temperature we are considering, this equilibrium fractionation direction deviates only slightly from the dilution line. From the histograms, we can clearly see different dynamical regimes: initially, the histogram spreads linearly from the parent along the spinodal direction as expected for spinodal dynamics. As nonlinear effects kick in, a curved path of compositions connecting a gas and a liquid phase is then formed. This clearly delineated 'arc' contains the compositions of the different parts of the system: as one moves in space from a gas bubble into the bulk liquid, one passes through a series of compositions within the interface between these two phases.

Beyond this generic structure, there are several interesting observations we can make from Figs. 2.8 and 2.9. The density histograms reveal that gas-liquid interfaces are strongly fractionated, with the arc being well away from the dilution line, in the B-rich part of the density plane. Physically, the reason is that B-particles have smaller σ_B and hence interact more weakly; they therefore pay a smaller energy penalty for sitting at an interface, where they have fewer neighbouring particles. Interfaces also have a well-defined sequence of density combinations as can be seen from the fact that the gas-liquid arc is quite narrow.

For further analysis it is useful to switch to the two-dimensional density histogram representation in Fig. 2.10. This shows the same data as in Fig. 2.9 but now seen from the top, with different heights corresponding to different colours. The peak in the high-density region of the histogram is also marked; this gives the majority composition of the bulk liquid at that time instant. It is interesting to observe that this peak, having started out at the parent composition and 'walked' along the spinodal direction initially, does not subsequently move straight away towards the liquid equilibrium composition. Instead, the liquid phase composition stays away from its equilibrium optimum for a long time. In fact, for the dynamics shown in Fig. 2.10 the liquid peak moves *away* from its equilibrium point for a long transient period beyond the initial spinodal decomposition dynamics.

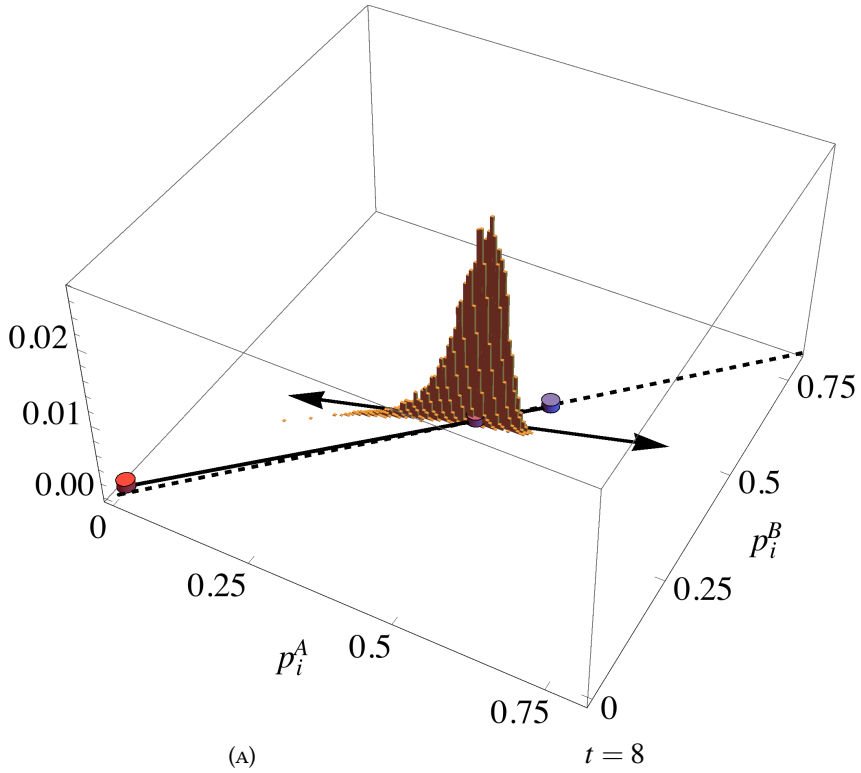

(A) $t = 8$

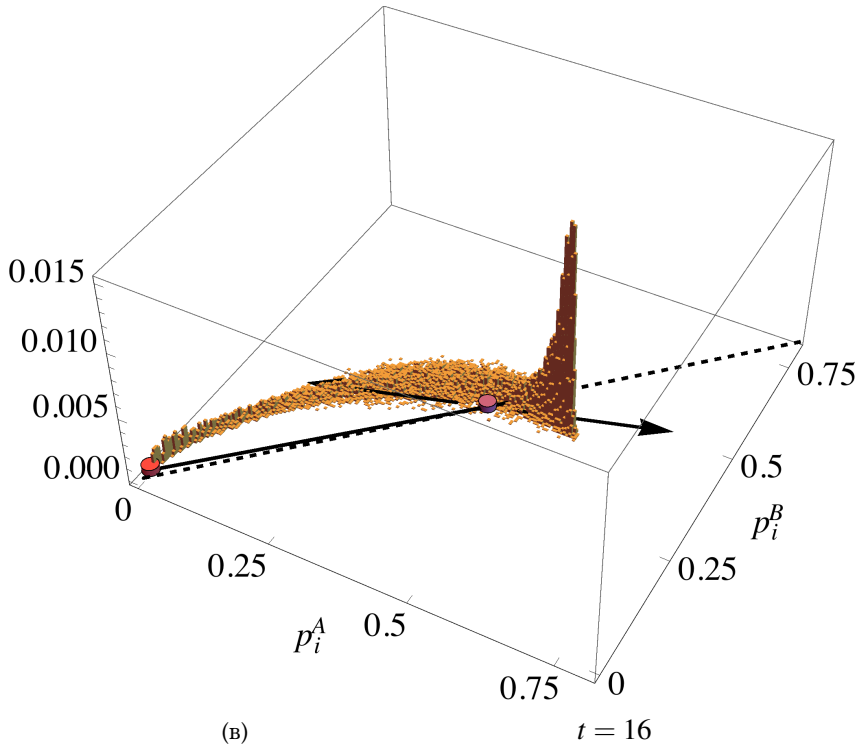

(B) $t = 16$

FIGURE 2.8: Time evolution of two-dimensional density histograms, in the (p_i^A, p_i^B)-plane, for the data used in Fig. 2.7; see text for details. The bin width along each dimension is 0.005. The parent phase lies on the dilution line (dashed). The red and blue dots off the dilution line mark the low- and high-density daughter phases obtained from our equilibrium numerics. The connecting tieline contains the parent and defines the equilibrium fractionation direction. The spinodal direction, which was obtained from our early-time analysis, is shown by the double-headed arrow.

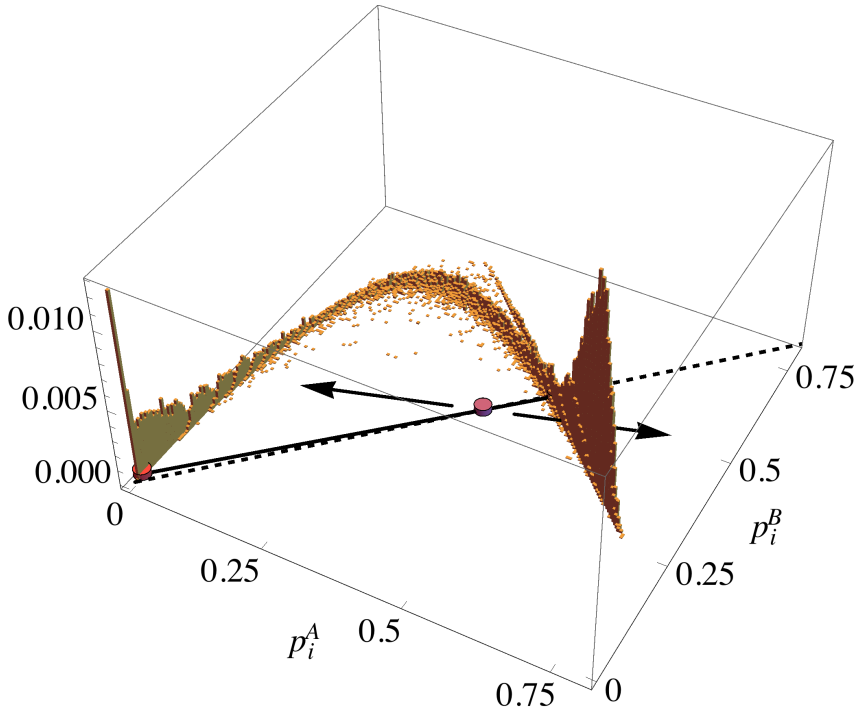

FIGURE 2.9: Same as in Fig. 2.8 but for $t = 316$.

This arises because the gas-liquid interfaces are strongly enriched in B-particles, leaving an unusually A-rich bulk liquid. Of course at very long times the equilibrium prediction and the dynamics must eventually agree, and we have verified that the density histogram peaks then indeed centre on the calculated equilibrium compositions while the arc with the interface compositions contains only a small ($\sim W/L$, where W is the interfacial width) fraction of probability. (See also the evolution of two-dimensional density histograms in the animation in the ESI for Ref. [35].)

A final, intriguing feature of the dynamics we observe is the inhomogeneity of the bulk liquid: in the last two snapshots in Fig. 2.7 one can clearly see well-defined liquid regions that are unusually enriched in B-particles. In the density histograms of Figs. 2.9 and 2.10 and also Fig. 2.11, which shows results at a higher temperature, these regions manifest themselves as an 'arm' at high density that is quite distinct from the arc arising from gas-liquid interfaces.

Looking at Fig. 2.7 carefully, one notices that the origin of the B-rich liquid regions lies in the evaporation of gas bubbles. As these shrink, so do their interfaces, eventually forming dense patches. Because the interfaces are strongly fractionated, these dense patches

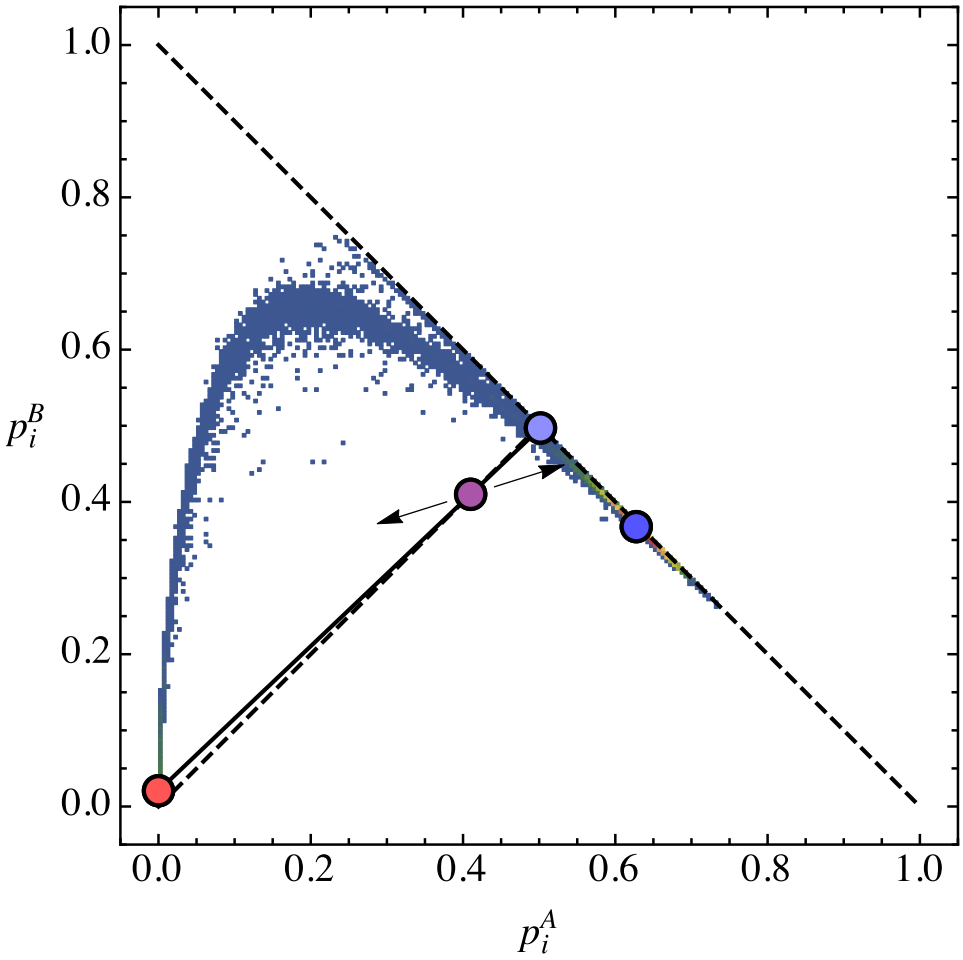

FIGURE 2.10: Same histogram as in Fig. 2.9, but now as seen from the top; different heights are represented by different colours. Additionally, we show the high-density peak of the histogram, which gives the majority composition of the bulk liquid.

are strongly enriched in B-particles. While the density of the patches can rapidly equilibrate to the bulk liquid—as shown by the fact that the arm almost coincides with a line of constant total number density $p^A + p^B$, as seen from Figs. 2.9, 2.10, and 2.11—it requires inter-diffusion of particles to equilibrate their composition. Hence the composition heterogeneities formed by these patches are unusually long-lived. We thus have here, in the long-time dynamics, another striking manifestation of Warren's hypothesis, in its general form which says that equilibration of composition is slow in dense systems. In order to check this interpretation we turned on w_s; as expected, the arm then disappears, and in the real-space images the liquid is clearly homogeneous (Fig. 2.12).

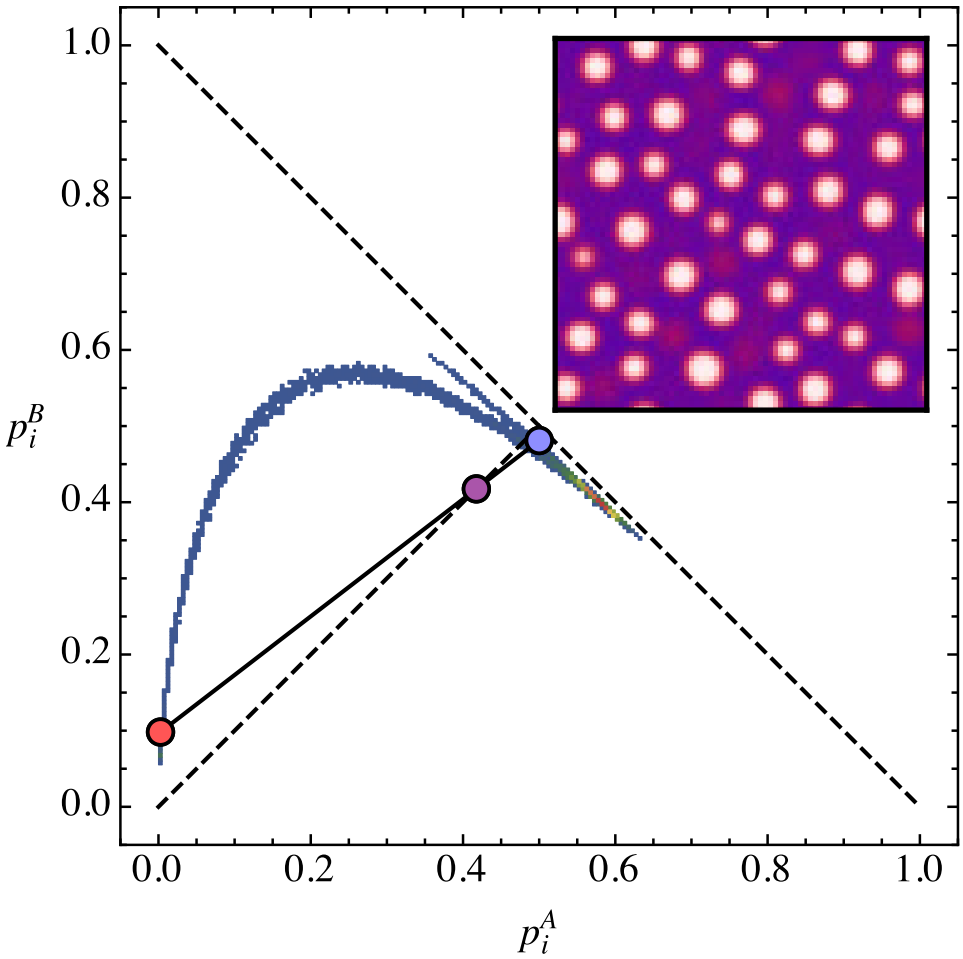

FIGURE 2.11: Density histogram showing a clear 'arm', a composition heterogeneity in the bulk liquid. This feature arises from the evaporation of gas bubbles: the remnants of their interfaces rapidly equilibrate to the liquid density but only slowly relax their composition, producing the B-rich patches (red) visible in the inset. Parameters: $p^A = p^B = 0.4175$, $T = 0.5$, $d = 0.25$, $w_s = 0$, and $L = 75$, at $t = 1110$. The inset shows the corresponding snapshot in real space.

2.5.2 Multicomponent fluids

Finally, we show now that a similar two-dimensional density histogram analysis can be performed even when one considers *arbitrary* M. A full density histogram in $(p_i^1, \ldots, p_i^M)$-density space would be M-dimensional, so one needs to project down to a manageable low-dimensional representation. The obvious choice for the new histogram axes are (the local versions of) low-order moment densities, which can be used for arbitrary M. We choose the local analogues of $\bar{\sigma}\rho_0 - \rho_1$ and ρ_0. The reason for this choice is that in the

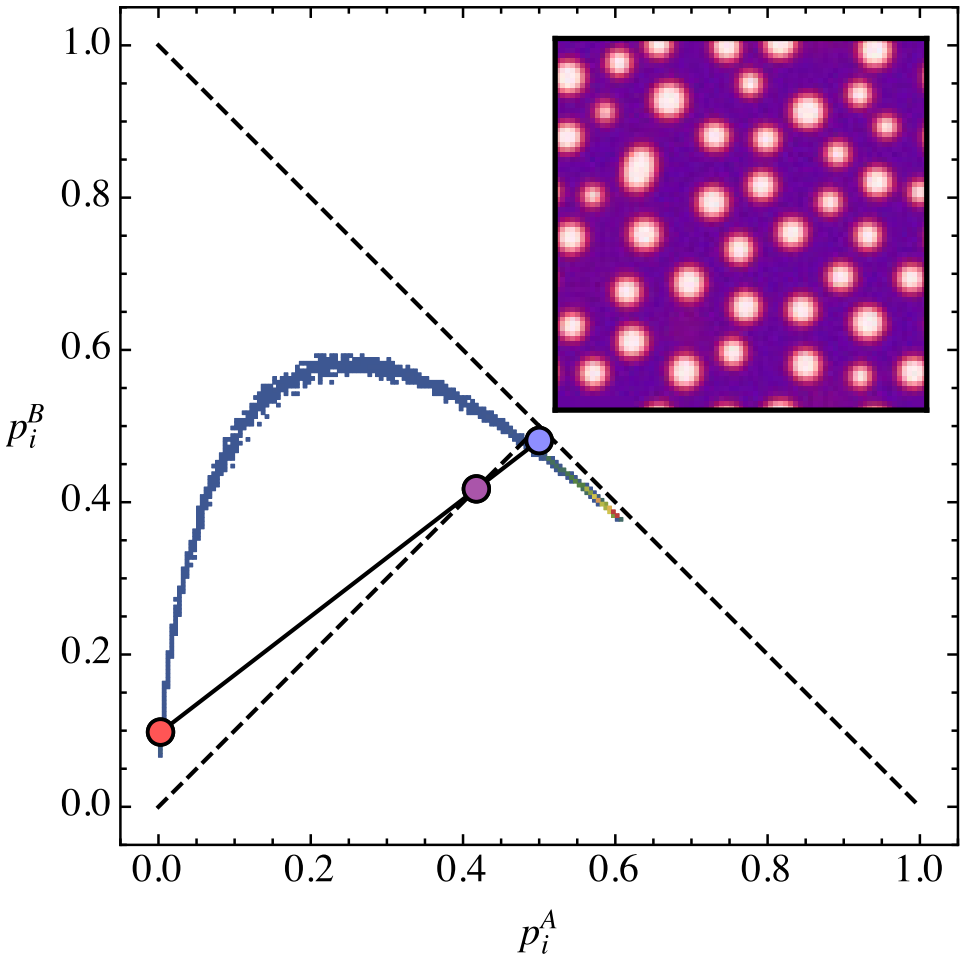

FIGURE 2.12: Same as Fig. 2.11, but now $w_s = 0.5$.

bidisperse case ($M = 2$),

$$\bar{\sigma}\rho_0 - \rho_1 = (\bar{\sigma} - \sigma_A)p^A + (\bar{\sigma} - \sigma_B)p^B = d(p^B - p^A) \tag{2.26}$$

while $\rho_0 = p^A + p^B$, so that the new histogram axes are just a rotated version (by 45°) of the ones we have used so far.

One can now use these quantities to plot two-dimensional density histograms for an arbitrary polydisperse system. It turns out that all the features that had been previously observed in the (p^A, p^B)-plane density histogram (i.e. the clearly delineated curved arc of interfaces compositions, the 'arm', etc.) remain qualitatively identical in this new coordinate system. Fig. 2.13 shows our results for systems with two, three, and four species. For $M = 3$, we used $\sigma \in \{1-d, 1, 1+d\}$, with relative densities (composition) given by $\{1/4, 1/2, 1/4\}$, whereas for $M = 4$ we chose $\sigma \in \{1-d, 1-d/2, 1+d/2, 1+d\}$ with

composition $\{1/6, 1/3, 1/3, 1/6\}$. We then identified values of d for each M that give the same set of moment densities (ρ_0, ρ_1, and ρ_2) as we had in Section 2.5.1. (Thus the spinodal growth rates are also all the same and hence results at the same t are comparable—but similar results were found using different parameter sets chosen by the same method.) Even though these histograms are now projections of M-dimensional histograms to two dimensions, we still get thin arcs between daughter phases, showing that there is still a well-defined sequence of compositions in the interfaces. We have performed checks over a larger parameter range, where we find that long-lived composition heterogeneities also appear in situations where one expects a pronounced slowing down of fractionation, exactly as we saw for $M = 2$; correspondingly, they disappear (data not shown) when direct particle swaps are turned on.

The fact that the density histograms for different M in Fig. 2.13 are so similar is quite remarkable. This similarity is surprising because the mean-field dynamical equations (2.16) do not in general reduce to closed dynamical equations for local moments like ρ_0 and ρ_1, due to nonlinear dependences on particle size σ in the Glauber rates. Nonetheless our numerical results suggest that degrees of freedom not captured by these moments only influence the dynamics weakly, so that they could provide a useful way of thinking about the dynamics even for $M \to \infty$.

2.6 Conclusions

In this work we investigated the dynamics of how colloidal polydisperse systems phase-separate, by introducing new kinetic equations based on the Polydisperse Lattice-Gas model [36]. As a baseline for our mean-field approach to the dynamics we calculated the mean-field equilibrium phase diagram of the model, including cloud and shadow curves as well as spinodals. To test Warren's two-stage scenario [49], we obtained both the annealed and quenched versions of the phase diagram, the latter referring to a system that can only change its density but has fixed composition. We analysed the linearized dynamical equations to understand the dynamics of spinodal decomposition, and found clear evidence in support of Warren's proposal. For the late-stage dynamics, we introduced a

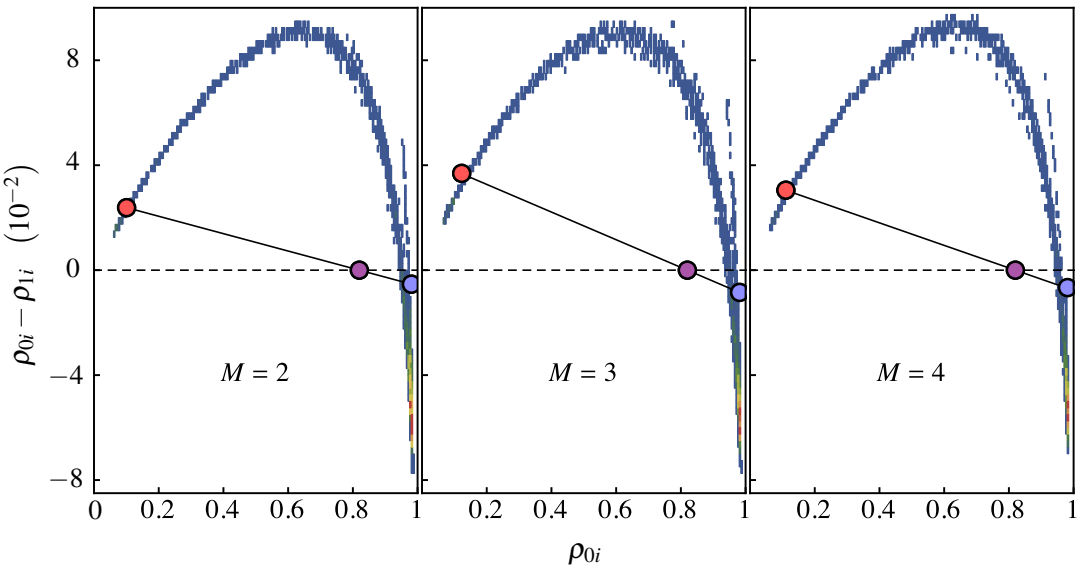

FIGURE 2.13: Density histogram for different number of species $M = 2, 3, 4$. The set of moment densities ρ_0, ρ_1, and ρ_2 is the same in all three cases. (This was achieved by appropriate choice of the parameter d, which was set to 0.25, 0.354, and 0.354, respectively; see text for details.) The other parameters are $\rho = 0.82$, $T = 0.5$, $w_s = 0$, and $L = 50$, at $t = 760$. The bin widths along the axes ρ_{0i} and $\rho_{0i} - \rho_{1i}$ are 0.005 and 0.0025, respectively.

two-dimensional density histogram method that allows fractionation effects in the phase-separation dynamics to be clearly visualized. This revealed strongly fractionated interfaces between gas and liquid. It also helped us to detect the existence of long-lived composition heterogeneities in the bulk liquid, which are a further manifestation of the fact that fractionation dynamics is slow as suggested by Warren. This prediction may be amenable to experimental verification in dense colloidal systems. The whole analysis was performed for an arbitrary number of particle species, although much of it was presented in the binary mixture context for the sake of simplicity and ease of visualization.

Our main assumptions were that the dynamics can be described by a kinetic lattice model, and that a mean-field approximation is at least qualitatively accurate. One could ask whether non-mean-field effects in the equilibrium phase diagram of the PLG might cause significant changes in the phase-separation dynamics. This could be tested by deploying higher order approximations beyond our dynamical mean-field theory (DMFT), such as the Path Probability Method (PPM) [63]. One might expect that the PPM would not necessarily lead to new qualitative outcomes for the analysis presented here, since no differences were observed in a previous comparison between PPM and DMFT, though in

the somewhat different context of relaxation dynamics in porous materials [64]. Direct Kinetic Monte Carlo (KMC) simulations could be used to directly probe the dynamics of the PLG model and so assess the effects of our mean-field approximation. Such simulations were performed in Ref. [65] for similar systems consisting of two species plus vacancies, where $p^A = p^B$ and the Hamiltonian is given by

$$H = -\sum_{\langle i,j \rangle} \sum_{\alpha,\beta} \varepsilon_{\alpha\beta} n_i^\alpha n_j^\beta \tag{2.27}$$

with $\alpha = A, B$. This setting includes the PLG Hamiltonian (for $M = 2$) given by Eq. (2.1) but allows more generic interactions $\varepsilon_{\alpha\beta}$. Also using a mean-field phase diagram as a reference, the authors of Ref. [65] investigated segregation kinetics with particle-particle swaps forbidden (corresponding to $w_s = 0$ in our notation) or highly energetically suppressed. They focussed on the existence of different domain growth morphologies in various parameter regimes. However, their choices for the interaction strengths $\varepsilon_{\alpha\beta}$ were rather different from ours. Our separable assignment $\varepsilon_{\alpha\beta} = \sigma_\alpha \sigma_\beta$ makes liquid-gas phase separation the dominant physical process, for which we then study the effects of polydispersity. On the other hand, the authors of Ref. [65] look at much less attractive (and even repulsive) AB interactions, always with $\varepsilon_{AA} = \varepsilon_{BB}$. This leads to distinct physical effects, including the condensation of vacancies at interfaces between A- and B-rich phases.

KMC simulations could also be used to fit our model parameters to experimental systems. Ref. [66] explains that one way of obtaining a physically reasonable value for the particle-vacancy jump attempt rate w_0 is by comparing the estimated ($\hat{D}$) and experimental (D_s) self-diffusion coefficients. If $\hat{D}$ is obtained from KMC simulations in dimensionless units, the desired correspondence would be $D_s = \hat{D} a^2 w_0$, where a is the lattice spacing. Therefore, fixing the value of a, an estimate of w_0 can be obtained. (In principle, one could try to develop a similar scheme to obtain a value for w_s.)

Coming to the limitations of the PLG model itself, one obvious shortcoming is the fact that a lattice model cannot capture gradual increases in density that are possible in an off-lattice setting, where even in an already fairly dense system collective motion can reduce the typical distance between particles. In a lattice model, on the other hand, density increases have to come from localized filling in of vacancies, or equivalently vacancies

diffusing away. As we explain below the presence of vacancies also enables fractionation. Because both relaxation of density and of composition are then tied to the presence of vacancies, it is clear that the latter cannot become arbitrarily slow compared to the former. In a continuum model, however, one would expect that large pockets of free volume that are required for the interchange of particles of different species become rare quickly at high density while collective motion to relax density still remains possible. Therefore, if anything, we expect the slowing down of fractionation compared to density relaxation at high densities to be *more* pronounced than in our lattice model. Hence the effects we observe should be stronger in more realistic, off-lattice models, getting closer to an ideal two-stage scenario for the phase-separation kinetics.

We illustrate how vacancies enable fractionation in Fig. 2.14, which shows a sketch of a *vacancy-mediated* interchange between two particles of different species. A sequence of 4 particle moves within the small lattice portion shown (2×2 lattice sites) is sufficient to interchange the blue and red particle in the lattice row above the initial vacancy. (Note that in this sequence the two blue particles have also interchanged their positions, but as they are indistinguishable this is immaterial.) Therefore, as fractionation requires interdiffusion of particles of different species, it will be able to proceed locally as long as vacancies are present. As a particle swap can be accomplished with a moderate number of elementary particle moves, fractionation cannot become arbitrarily slow compared to density relaxation–which locally requires a single particle move–as claimed above. This is the likely reason why we do not see an 'ideal' two-stage scenario, including e.g. the fact that at early times the spinodal dynamics within the quenched spinodal region already has a component of fractionation rather than consisting of the growth of pure density fluctuations.

Of course off-lattice models at the particle level are difficult to deal with theoretically, so before studying phase-separation dynamics one would aim to derive from them approximate representations in terms of a continuum field theory such as the so-called Model B or rather a polydisperse variant thereof [67,68]. For a monodisperse system and with stochastic fluctuations neglected, this would give an equation of the (generalized) Cahn–Hilliard

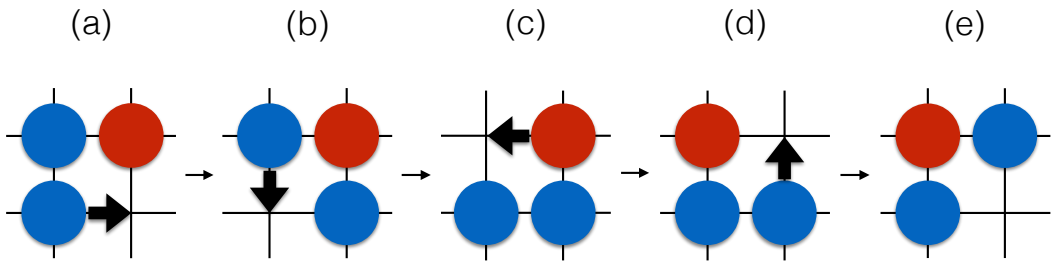

FIGURE 2.14: Sketch of vacancy-medidated interchange between two particles of different species. In the first configuration a red particle is on the top-right site of the 2×2-lattice region, whereas a blue particle sits on the top-left site. In order for the subsystem to reach a configuration where one has instead a blue particle top-right and a red one top-left, four particle moves (particle-vacancy swaps) are required, as shown by the sequence (a)–(e).

type [69]

$$\frac{\partial \rho(\mathbf{r},t)}{\partial t} = \nabla \cdot \left[\mathcal{M}(\rho(\mathbf{r},t)) \nabla \frac{\delta F[\rho(\mathbf{r},t)]}{\delta \rho(\mathbf{r},t)} \right] \tag{2.28}$$

where F is the free energy functional, $\rho(\mathbf{r},t)$ is the continuous density field, and $\mathcal{M}(\rho(\mathbf{r},t))$ is a density-dependent mobility; within a simple approximation scheme [70] one finds $\mathcal{M}(\rho(\mathbf{r},t)) = \rho(\mathbf{r},t)$.

In the polydisperse case, the analogue of Eq. (2.28) involves a mobility matrix with $M \times M$ entries. (In fact, our kinetic Eq. (2.16) can be cast in the form of a discrete Cahn–Hilliard equation, generalized to polydisperse fluids and inhomogeneous mobilities; in the linear version, Eq. (2.19), the generalized Cahn–Hilliard form is clear.) Determining such an entire mobility matrix from an off-lattice model is a considerable challenge, also because the results might differ for size versus interaction polydispersity (similarly to the differences found in the mobility coefficients between systems with length and chemical polydispersity, in Ref. [52]). One route to deriving such Cahn-Hilliard-like equations would be dynamical density functional theory (DDFT); it should be possible to adapt this to a fully polydisperse scenario and then use it to test Warren's two-stage scenario [71, 72].

A further theoretical challenge is the incorporation of stochastic effects, in order to be able to describe nucleation and growth dynamics. The simplest way of achieving this would be to add Langevin noise to either our lattice dynamics (2.16) or a continuum description like Eq. (2.28). This however requires a consistent, quantitative way of adding

multiplicative Langevin noise to the deterministic equations. The need for a quantitative accurate stochastic description lies in the fact that one wants to *compare* equilibration timescales between systems placed in different regions of the phase diagram, which means one has to assess the competition between nucleation and growth dynamics on the one hand and spinodal decomposition on the other. For instance, for systems placed within R2 (see Table 2.1) one would like to compare the timescale for nucleation and growth in stage 1 (which should have a fast intrinsic time scale because it does not require fractionation, but could be slowed down by large nucleation barriers) to spinodal dynamics in stage 2 (intrinsically slow because it requires fractionation, but not affected by activation barriers). A model being able to describe quantitatively both types of phase ordering dynamics would clearly be valuable here. This could potentially be obtained from the lattice-based theory presented here via systematic coarse-graining [73]. Alternatively, fluctuating hydrodynamics [74–77] is a possible avenue for deriving models incorporating stochasticity, though whether this can be implemented for polydisperse dynamics and would give a reasonable quantitative account of the physics remains an open question.

In addition to stochastic effects we have also neglected hydrodynamic interactions due to the solvent. This is commonly done throughout the literature on polydisperse dynamics, but in the case of dense systems, which are especially pertinent in the context of the two-stage phase-ordering scenario, they may play an important role [71].

Our work in this chapter could be extended to investigate the relaxation dynamics of polydisperse fluids in porous materials, generalising previous work done by Peter Monson and others [78–80]. In fact, although the dynamical mean-field theory calculations developed in those papers are restricted to $M = 1$ and $M = 2$, they are very similar to the ones presented here. For application to porous materials, we would mainly need to adapt our approach to cover given pore geometries. In this scenario, a natural question would be 'what is the impact of slow fractionation on the relaxation dynamics in porous materials?'. This is potentially one of the simplest future research topics to pursue if one uses our current theory as a starting point.

Finally, we point out that one could use the framework developed here to investigate

yet other problems, e.g. the dynamics of polydisperse wetting or the phase-separation behaviour of polydisperse systems of active particles. It would also be interesting to develop perturbative or scaling approaches for the dynamics of systems with small polydispersity, and to consider alternative ways of obtaining mean-field approximations, for example by explicitly taking the limit of high spatial dimension or considering a Kac-like setup with long-range interactions [37, 81–83].

Appendices

2.A Monotonic decrease of the free energy

Here we show that in the kinetic PLG model with both particle-vacancy and direct particle swaps (with Glauber-like rates, arbitrary M, arbitrary overall composition, and arbitrary attempt rates) the free energy obeys $dF/dt \leq 0$. As we will see, the derivation is not as straightforward as in the case of a binary mixture without direct particle swapping, which was discussed in Ref. [54]. The beginning is identical, though. As the free energy F is a function of all dynamical variables p_i^α we can write

$$\frac{dF}{dt} = \sum_i \sum_\alpha \frac{\partial F}{\partial p_i^\alpha} \frac{dp_i^\alpha}{dt} \tag{2.29}$$

which, combined with the definitions for the chemical potential and for the current, can be rewritten as

$$\frac{dF}{dt} = -\sum_\alpha \sum_i \sum_{j \in \partial i} \mu_i^\alpha J_{ij}^\alpha \;=\; -\sum_\alpha \sum_{\langle i,j \rangle} (\mu_i^\alpha J_{ij}^\alpha + \mu_j^\alpha J_{ji}^\alpha). \tag{2.30}$$

Using the fact that $J_{ij}^\alpha = -J_{ji}^\alpha$ we can write

$$\frac{dF}{dt} = -\sum_\alpha \sum_{\langle i,j \rangle} \left(\mu_i^\alpha - \mu_j^\alpha\right) J_{ij}^\alpha. \tag{2.31}$$

Defining a two-species current $J_{ij}^{\alpha\gamma}$ in the obvious way using

$$J_{ij}^\alpha = \sum_{\gamma \geq 0} J_{ij}^{\alpha\gamma} \tag{2.32}$$

transforms this further into

$$\frac{dF}{dt} = -\sum_{\langle i,j\rangle}\sum_{\alpha,\gamma} J_{ij}^{\alpha\gamma}\left(\mu_i^\alpha - \mu_j^\alpha\right). \tag{2.33}$$

The sum can be extended to $\alpha \geq 0$ because $\mu_i^0 = 0, \forall i$. Also note that $J_{ij}^{\alpha\gamma}$ is antisymmetric under interchange of α and γ. After adding the same expression with α and γ swapped and using this antisymmetry, we have

$$\frac{dF}{dt} = -\frac{1}{2}\sum_{\langle i,j\rangle}\sum_{\alpha,\gamma} J_{ij}^{\alpha\gamma}\left[\left(\mu_i^\alpha - \mu_j^\alpha\right) - \left(\mu_i^\gamma - \mu_j^\gamma\right)\right] \tag{2.34}$$

However, the term in square brackets can be written as $\ln(C_i^\alpha C_j^\gamma) - \ln(C_j^\alpha C_i^\gamma)$ (except of a T) by defining the local chemical activity C_i^α as $C_i^\alpha = \exp(\mu_i^\alpha/T)$. This has the same sign as $J_{ij}^{\alpha\gamma}$ because the two-species current can be written as a positive quantity multiplied by $C_i^\alpha C_j^\gamma - C_j^\alpha C_i^\gamma$. [This fact can be seen from the mean-field expression for the energy change, Eq. (2.17), which enters the rates via $\exp(\Delta H_{ij}^{\alpha\gamma}/T) = p_i^\alpha p_j^\gamma C_i^\gamma C_j^\alpha/(p_i^\gamma p_j^\alpha C_i^\alpha C_j^\gamma)$. Remember Eq. (2.21) for the local chemical potential of a species.] Therefore, each link $\langle i,j\rangle$ and each pair of (α,γ) makes a negative contribution to dF/dt. One can also phrase the last step in the other direction, i.e. by writing

$$J_{ij}^{\alpha\gamma} = -\mathcal{M}_{ij}^{\alpha\gamma}\left[\left(\mu_j^\alpha - \mu_i^\alpha\right) - \left(\mu_j^\gamma - \mu_i^\gamma\right)\right] \tag{2.35}$$

and checking that the site-dependent mobility $\mathcal{M}_{ij}^{\alpha\gamma}$ is positive. This makes sense because a particle swap is driven by how the difference in α-chemical potential between sites i and j compares to the corresponding difference in γ-chemical potential. Note that while the factor $1/2$ in Eq. (2.34) may look somewhat unexpected, antisymmetry of the current $J_{ij}^{\alpha\gamma}$ again shows that (α,γ) and (γ,α) make the same contribution, so one could eliminate the $1/2$ again and restrict the summation to ordered pairs of species labels, say $\alpha < \gamma$.

2.B Derivation of growth rates

In this appendix we derive the linearized mean-field equations of motion and determine from them the expressions for the spinodal growth rates. Consider a homogeneous system of overall composition defined by a list of species densities $\{p^\alpha \mid \alpha = 1,\dots,M\}$. The system is perturbed by small fluctuations of the densities:

$$p_i^\alpha = p^\alpha + \delta_i^\alpha \quad \forall\alpha \tag{2.36}$$

where $\delta_i^\alpha \ll 1$. In a linear expansion we can write Eq. (2.17) as

$$\left\langle \Delta H_{ij}^{\alpha\gamma} \right\rangle = \sum_\beta \left(\sum_{k\in\partial i} \varepsilon_{\alpha\beta}\,\delta_k^\beta - \sum_{l\in\partial j} \varepsilon_{\alpha\beta}\,\delta_l^\beta \right) - \sum_\beta \left(\sum_{k\in\partial i} \varepsilon_{\gamma\beta}\,\delta_k^\beta - \sum_{l\in\partial j} \varepsilon_{\gamma\beta}\,\delta_l^\beta \right). \tag{2.37}$$

Now remember our kinetic Eqs. (2.16)

$$\frac{dp_i^\alpha}{dt} = -\sum_{j\in\partial i}\sum_{\gamma=0}^{M} \left[\frac{p_i^\alpha p_j^\gamma w^{\alpha\gamma}}{1+\exp\left(\left\langle \Delta H_{ij}^{\alpha\gamma}\right\rangle/T\right)} - \frac{p_j^\alpha p_i^\gamma w^{\alpha\gamma}}{1+\exp\left(\left\langle \Delta H_{ji}^{\alpha\gamma}\right\rangle/T\right)} \right].$$

Using a simplified notation in which we drop the superscripts α and γ, the expression in the square brackets can be written as

$$\frac{A_{ij}}{1+\exp\left(\Delta E_{ij}/T\right)} - \frac{A_{ji}}{1+\exp\left(\Delta E_{ji}/T\right)} \tag{2.38}$$

where $A_{ij} = w^{\alpha\gamma} p_i^\alpha p_j^\gamma$ and $\Delta E_{ij} = \left\langle \Delta H_{ij}^{\alpha\gamma} \right\rangle$. As a consequence of linearization, the arguments in the exponentials are also small; hence, each sigmoid linearizes as $1/\left(1+\exp\left(x\right)\right) = \left(1/2\right)\left(1-x/2+\dots\right)$, and then we can write (2.38) in linearized form as

$$\frac{1}{4}\left[2\left(A_{ij}-A_{ji}\right) - \frac{\Delta E_{ij}}{T}\left(A_{ij}+A_{ji}\right) \right] \tag{2.39}$$

where we have used the fact that $\Delta E_{ij} = -\Delta E_{ji}$. Now Eq. (2.16) becomes

$$\frac{d\delta_i^\alpha}{dt} = -\sum_{j\in\partial i}\sum_{\gamma=0}^{M} \frac{w^{\alpha\gamma}}{4} \left\{ 2\left(p_i^\alpha p_j^\gamma - p_j^\alpha p_i^\gamma\right) - \frac{\left\langle \Delta H_{ij}^{\alpha\gamma}\right\rangle}{T}\left(p_i^\alpha p_j^\gamma + p_j^\alpha p_i^\gamma\right) \right\}. \tag{2.40}$$

As $\left\langle \Delta H_{ij}^{\alpha\gamma} \right\rangle$ is already linear in δ's, the last factor can be replaced by $2p^\alpha p^\gamma$. Linearizing also the first term then gives for the time evolution of the fluctuations

$$\frac{d\delta_i^\alpha}{dt} = -\sum_{j\in\partial i}\sum_{\gamma=0}^{M}\frac{w^{\alpha\gamma}}{4}\left\{2\left[p^\alpha\left(\delta_j^\gamma-\delta_i^\gamma\right)-p^\gamma\left(\delta_j^\alpha-\delta_i^\alpha\right)\right]-\frac{\left\langle\Delta H_{ij}^{\alpha\gamma}\right\rangle}{T}2p^\alpha p^\gamma\right\}. \tag{2.41}$$

The first part can be rewritten as

$$-\sum_{j\in\partial i}\sum_{\gamma=0}^{M}\frac{w^{\alpha\gamma}}{4}\left\{2\left[p^\alpha\left(\delta_j^\gamma-\delta_i^\gamma\right)-p^\gamma\left(\delta_j^\alpha-\delta_i^\alpha\right)\right]\right\} = -\Delta_{\mathrm{d}}\sum_{\gamma=0}^{M}\frac{w^{\alpha\gamma}}{2T}p^\alpha p^\gamma\left(\frac{T}{p^\gamma}\delta_i^\gamma-\frac{T}{p^\alpha}\delta_i^\alpha\right) \tag{2.42}$$

where Δ_{d} is the discrete Laplacian, defined for any site-dependent quantity g as $\Delta_{\mathrm{d}}g_i = \sum_{j\in\partial i}(g_j-g_i)$. For the second part, one can obtain

$$-\sum_{j\in\partial i}\sum_{\gamma=0}^{M}\frac{w^{\alpha\gamma}}{4}\left\{-\frac{\left\langle\Delta H_{ij}^{\alpha\gamma}\right\rangle}{T}2p^\alpha p^\gamma\right\} = \Delta_{\mathrm{d}}\sum_{\gamma=0}^{M}\frac{w^{\alpha\gamma}}{2T}p^\alpha p^\gamma\sum_\beta\left(\varepsilon_{\gamma\beta}-\varepsilon_{\alpha\beta}\right)\left(\Delta_{\mathrm{d}}+z\right)\delta_i^\beta \tag{2.43}$$

where z is the lattice coordination number and we used the fact that

$$\sum_{j\in\partial i}\left(\sum_{k\in\partial i}\delta_k^\beta-\sum_{l\in\partial j}\delta_l^\beta\right) = -\Delta_{\mathrm{d}}\left(\Delta_{\mathrm{d}}\delta_i^\beta+z\delta_i^\beta\right) \tag{2.44}$$

which can be easily derived in a few steps. Bearing in mind that summations over β do *not* include $\beta=0$ and defining a homogeneous mobility $\mathcal{M}^{\alpha\gamma}=\frac{w^{\alpha\gamma}}{2T}p^\alpha p^\gamma$, we have altogether

$$\frac{d\delta_i^\alpha}{dt} = \Delta_{\mathrm{d}}\sum_{\gamma=0}^{M}\mathcal{M}^{\alpha\gamma}\sum_\beta\left\{-\frac{T}{p^\gamma}\delta_{\gamma\beta}+\frac{T}{p^0}\delta_{\gamma 0}+\frac{T}{p^\alpha}\delta_{\alpha\beta}+\left(\varepsilon_{\gamma\beta}-\varepsilon_{\alpha\beta}\right)\left(\Delta_{\mathrm{d}}+z\right)\right\}\delta_i^\beta. \tag{2.45}$$

Note that the second term in the curly braces here comes from the identity $\delta_i^0=-\sum_\beta\delta_i^\beta$, which is a consequence of the local hard core constraint (2.2).

Alternatively, using the local chemical potential (2.21) linearized about the homogeneous state,

$$\frac{d\delta_i^\alpha}{dt} = \sum_{\gamma=0}\mathcal{M}^{\alpha\gamma}\Delta_{\mathrm{d}}\left(\mu_i^\alpha-\mu_i^\gamma\right). \tag{2.46}$$

We can now proceed to solve the linearized dynamical equations of motion. As a homogeneous system is invariant under translation with respect to the lattice vectors,

solutions of the linearized equations are superpositions of solutions of this form

$$\delta_j^\alpha = \delta p^\alpha \exp\left[i\mathbf{k}\cdot\mathbf{x}_j + \omega t\right] \tag{2.47}$$

where $\mathbf{k}$ is the fluctuation wave vector and $\mathbf{x}_j$ is the position in real space of a lattice site j. Moreover, ω is the spinodal decomposition growth rate and δp^α is the amplitude of the spinodal fluctuation associated with species α. Inserting this form of the solution into our Eq. (2.46) will give us an equation for ω. In order to have a useful relation, however, the application of the discrete Laplacian operator Δ_d to a δ_j^α needs to be translated into some commutative operation so that we can deal with the $\exp\left[i\mathbf{k}\cdot\mathbf{x}_j + \omega t\right]$ properly, as follows:

$$\begin{aligned}
\Delta_\mathrm{d}\delta_j^\alpha &= \delta p^\alpha \exp(\omega t) \sum_{l\in\partial j} \left[\exp(i\mathbf{k}\cdot\mathbf{x}_l) - \exp(i\mathbf{k}\cdot\mathbf{x}_j)\right] \\
&= \delta p^\alpha \exp(i\mathbf{k}\cdot\mathbf{x}_j + \omega t)\left[\sum_{l\in\partial j} \exp(i\mathbf{k}\cdot\mathbf{x}_l - i\mathbf{k}\cdot\mathbf{x}_j) - z\right] \\
&= \delta p^\alpha \exp(i\mathbf{k}\cdot\mathbf{x}_j + \omega t)\left[z + A - z\right] = A\delta_j^\alpha
\end{aligned} \tag{2.48}$$

where (in the case of a 2-dimensional system) we have $A = A(\mathbf{k}) = -4\sin^2(k_x a/2) - 4\sin^2(k_y a/2)$. Then this $A(\mathbf{k})$, or just A, replaces Δ_d, and Eq. (2.46) can be written as an equation that no longer involves site-dependent quantities

$$\omega\delta p^\alpha = \sum_{\gamma=0}^{M} \mathcal{M}^{\alpha\gamma} \sum_\beta \left\{ T\left(-\frac{\delta_{\gamma\beta}}{p^\gamma} + \frac{\delta_{\gamma 0}}{p^0} + \frac{\delta_{\alpha\beta}}{p^\alpha}\right) + \left(\varepsilon_{\gamma\beta} - \varepsilon_{\alpha\beta}\right)(A+z)\right\} A\delta p^\beta . \tag{2.49}$$

As we did in the main text, let us now set $w^{\alpha 0} = w_0$ and $w^{\alpha\beta} = w_s$, for any $\alpha \neq 0$ and $\beta \neq 0$, where w_0 and w_s are constant attempt rates associated with particle-vacancy and particle-particle exchanges, respectively. We next derive two equations involving ω. The first is obtained by summing up Eq. (2.49) over all species α. This gives

$$\omega\delta\rho = \frac{Aw_0}{2}\left[\delta\rho - \frac{A+z}{T}(1-\rho)\rho_1\delta\rho_1\right] \tag{2.50}$$

where $\delta\rho \equiv \delta\rho_0$ and

$$\rho_n = \sum_\alpha \sigma_\alpha^n p^\alpha \tag{2.51}$$

$$\delta\rho_n = \sum_\alpha \sigma_\alpha^n \delta p^\alpha \tag{2.52}$$

are the moment densities (and their fluctuations), and we have used $\varepsilon_{\alpha\beta} = \sigma_\alpha \sigma_\beta$. For the case with a continuous polydisperse attribute, the summations are integrals. The second equation is obtained by multiplying Eq. (2.49) by σ_α and then summing it over all species. The result is

$$\begin{aligned}\omega\delta\rho_1 = \frac{Aw_0}{2}\left[\rho_1\delta\rho + (1-\rho)\,\delta\rho_1 - \frac{A+z}{T}(1-\rho)\,\rho_2\delta\rho_1\right] \\ + \frac{Aw_s}{2}\left[\rho\delta\rho_1 - \rho_1\delta\rho + \frac{A+z}{T}\left(\rho_1^2 - \rho_2\rho\right)\delta\rho_1\right].\end{aligned} \tag{2.53}$$

By using that $\delta\rho$ and $\delta\rho_1$ should not both be nonzero in the spinodal dynamics and combining the two equations, one can now find $\omega(\mathbf{k})$. One obtains two non-trivial branches $\omega(\mathbf{k})$; we require the largest one, which is Eq. (2.24). There are a further $M-2$ eigenvalues (and eigenvectors) with $\delta\rho = \delta\rho_1 = 0$, leading to $M-2$ trivial branches that all have identical negative eigenvalues. Explicitly, these are given by $\omega = \frac{A}{2}\left[w_0(1-\rho) + w_s\rho\right]$ but as we are looking for the fastest growing modes, they can be ignored.

Chapter 3

Secondary phase separation in colloidal mixtures: Composition heterogeneities

3.1 Introduction

In Section 2.5 we have shown that phase-separating colloidal fluid mixtures can exhibit long-lived 'composition heterogeneities' if they are dense enough. This effect is obviously impossible in one-component fluids because in that case the composition is the same everywhere (all particles are the same) and only the total local density fluctuates. Firstly we have observed that bubbles—or more generally domains—can be formed with strongly 'fractionated' interfaces. This means in the binary case that the gas-liquid interface is much richer in one of the two colloidal components. For arbitrary polydisperse systems, we say that the interface is strongly fractionated if its composition distribution is very different from that of the initially well-mixed fluid ('parent phase') and also from that of the surrounding liquid. Thus, when a bubble shrinks into non-existence by means of the Ostwald ripening mechanism, remnants of its interface continue to be visible for a long time as they struggle—due to crowding—to equilibrate their composition with that of the surrounding liquid. This is not true for the interfaces in monodisperse systems because equilibration in this case can take place much more quickly: the newly-formed domains do not need to enrich in certain species, making the diffusion process easier. We can say

that in the mixture case there is a slow fractionation effect (or one could say slow 'de-fractionation', if we consider a system whose interface is more fractionated than the final equilibrium liquid, in comparison to the original parent composition).

In the present chapter we broadly explore a variety of manifestations of composition heterogeneities in colloidal mixtures. As in Chapter 2, these effects are driven by crowding but here we will consider more complicated liquid-gas phase separation experiments. In fact, we have performed simulations of phase separation with a 'two-step temperature quench' (or just 'double quench'). We specifically consider phase separation after a second, deeper quench following an initial two-phase separation from a first quench. In this scenario, one would expect that secondary domains are transiently formed within phases, before eventually being reabsorbed into the larger domains. We will place particular emphasis on low-temperature or 'deep' second quenches. We have also found interesting effects in the regime where the total local density does not make composition changes too slow, as we will see.

The study of the nonlinear time evolution of phase-separating structures in double quench processes can be viewed as part of the larger endeavour of seeking to understand history dependence in phase separation [84], and accordingly has seen increasing interest in recent years. One of the motivations is the fact that it can lead to strategies for controlling structure formation [85], in particular with regards to tailoring domain formation in polymeric materials [86]. Also, the microstructure of food, paint, biological fluids, etc. not only depends on their constituents but is also an arrested morphology determined by external conditions, such as temperature, that influence the structural evolution [85]. Double quenches have been explored numerically [85–90] and experimentally [91–94], but on the theoretical side only a handful of studies can be applied to colloidal mixtures, none of them looking at effects of the slow composition changes or even at compressible fluids. In Ref. [89] the double quench is modeled via the Cahn–Hilliard equation for incompressible symmetric binary polymer mixtures, using a Flory–Huggins free energy functional. After a first quench into the unstable region, the mixture phase-separates via spinodal decomposition into domains that subsequently coarsen; a second quench is then applied to a point further inside the unstable two-phase region. A new structure factor peak arises

from this second quench and eventually disappears as the system progresses towards a single-domain final equilibrium state.

Here we consider compressible binary colloidal mixtures undergoing secondary temperature quenches into both two- and three-phase regions. We also revisit single quenches but now starting the computational experiment from an already-formed slab domain of well-mixed fluid mixture surrounded by a bath of very dilute vapour. This is similar to one of the geometries considered in a model of binary alloys in Refs. [53, 54], where phase separation starts first at the interface between the vapour and the slab. In our case we will see that within the slab domain other domains (of gas, i.e. bubbles) are formed transiently in a way that can be connected to the double quench experiment. This is because both situations can be viewed as instances of 'domain-within-domain' (or 'secondary') phase separation.

The PLG (Polydisperse Lattice-Gas) mean-field kinetic theory derived in Chapter 2 will be used again in this chapter, for both analytical and numerical approaches. (We will also calculate the equilibrium composition as we did in Chapter 2, i.e. by solving the coexistence conditions.) As we have seen, the theory includes two elementary processes: particle-solvent and particle-particle exchanges. Their relative rate will be used to tune and characterise the effects of slow composition changes in the form of composition heterogeneities. For the sake of simplicity only mixtures of two attractive species plus 'vacancies' (or passive solvent particles) will be considered, but we expect the phenomena observed here to be relatively straightforward to generalise to arbitrary polydisperse systems using the route that we proposed and explored in Section 2.5.2.

The remainder of this chapter is organised as follows. In Section 3.2 we study slow-fractionation effects after secondary quenches into the two-phase region. In Section 3.3 we consider the slab domain as initial state. In Section 3.4 we discuss our simulations for secondary quenches into the three-phase region. Section 3.5 concludes the chapter with a summary, discussion and pointers towards future work.

3.2 Deep secondary quench

Here we consider two-step temperature quenches where the final, second temperature quench takes us further into the unstable region. We will refer to the structures formed after the first quench as primary domains. These will be allowed to coarsen before we perform a secondary quench, which in turn may or may not give rise to the formation of secondary domains within each of the primary phase domains. We will be interested primarily in investigating the secondary phase separation within the primary liquid phase rather than in the gas. This is because the liquid is at higher density and so much more likely to show the effects of slow composition changes. Note that in line with this focus, the secondary quench temperature has to be low enough to make the primary liquid phase unstable. If we let the primary phase separation run for long enough to have nearly equilibrated primary phase compositions, we can say that the liquid will be unstable following the secondary quench if the second quench temperature satisfies

$$T \leq z\left(\rho_2 - \rho_1^2\right) \tag{3.1}$$

where the right-hand side is the annealed spinodal temperature given by Eq. 2.6 and evaluated at the composition of the equilibrium liquid obtained from the primary phase separation. The occurrence or not of an instability in the primary gas phase can be calculated analogously. Moreover, the minimal 'size' of the secondary structures must be smaller than the length scale of the primary domains. We quantify this by the secondary phase separation spinodal length, i.e. $2\pi/k_{\max}$, where $\omega(k_{\max}) = \omega_{\max}$. (See Chapter 2 and Eq. 2.24.)

In order to access clearly distinct behaviours—slow versus fast composition changes—we will compare simulations performed for $w_s = 0$ and $w_s = 1$ at deep secondary quenches but remaining for now within the two-phase region. (Recall here that w_s is the attempt rate for particle-particle swaps.) This makes the primary liquid phase both unstable and dense enough to trigger slow-fractionation effects (for $w_s = 0$). As before, we will start from a parent system with equal amounts of the two species. The normalized polydisperse distribution, therefore, is $(0.5, 0.5)$ and the polydisperse attributes are $\sigma_A = 1 + d$ and

$\sigma_B = 1 - d$, where d is chosen between 0 and 1. The colour scheme in the simulation snapshots throughout the chapter translates essentially as this: dense regions with a high concentration of A's are blue, those with predominantly B's are red and dilute regions dominated by vacancies are white. In this low-T context the final equilibrium liquid has very little fractionation since the gas is extremely dilute and therefore the vast majority of the particles are in the liquid. The caveat of using such low temperatures is that we get a strong slowdown, and consequently computational times increase dramatically; also, we expect to see 'square' interfaces as a consequence of the lattice structure. This happens due to the system's difficulty in overcoming energy barriers that could lead to the formation of more rounded domains. The former of these issues does not pose a significant problem since simulations accessing the final asymptotic coarsening where the secondary domains have disappeared will be beyond our scope. The latter would not be expected to affect the physics qualitatively, though this is something that would be worth checking in future work via e.g. off-lattice simulations.

Fig. 3.1 shows snapshots at times both before and after a secondary quench into the two-phase region of a binary mixture. (For the simulations shown in this chapter we have found it useful to implement an adaptive time-stepping method like the one studied in Ref. [95].) The system's overall density of colloidal particles is 0.75. The first quench, to a temperature $T = T_1 = 0.7$, is shallow and generates a primary liquid that is only slightly fractionated and has a high overall density of 0.92. The second, deep quench down to temperature $T = T_2 = 0.1$ was then performed at $t = t_2 = 40000$, a time at which the primary domains have substantially grown and nearly equilibrated their compositions. After some time we can see in the snapshots that small secondary domains have formed. Our primary and secondary domains of interest are the 'large' and 'small' gas bubbles, respectively, in the surrounding liquid; tiny liquid droplets also form within the primary gas bubbles but these equilibrate quickly by being reabsorbed through the interface as a result of the fast dynamics at the very low density of the gas phase. The initial lengthscale of the secondary structures formed in the primary liquid is consistent with the spinodal lengthscale predicted theoretically; note that because of the large value of t_2 used, the primary bubbles have become sufficiently separated from each other to fit a few such spinodal lengths of

the secondary phase separation in between them. Note that the secondary spinodal dynamics manifests initially as 'waves' propagating from the primary bubbles interfaces, a behaviour that we will discuss further below. (See Section 3.3.) This leads to the formation of the secondary gas bubbles. Once these eventually disappear again by shrinking, their fractionated interfaces remain visible as strongly long-lived patches of composition heterogeneities. This is analogous to what we found in the simulations in Chapter 2 but here we can see these composition heterogeneities during time intervals at least two orders of magnitude longer, as a result of the low temperature.

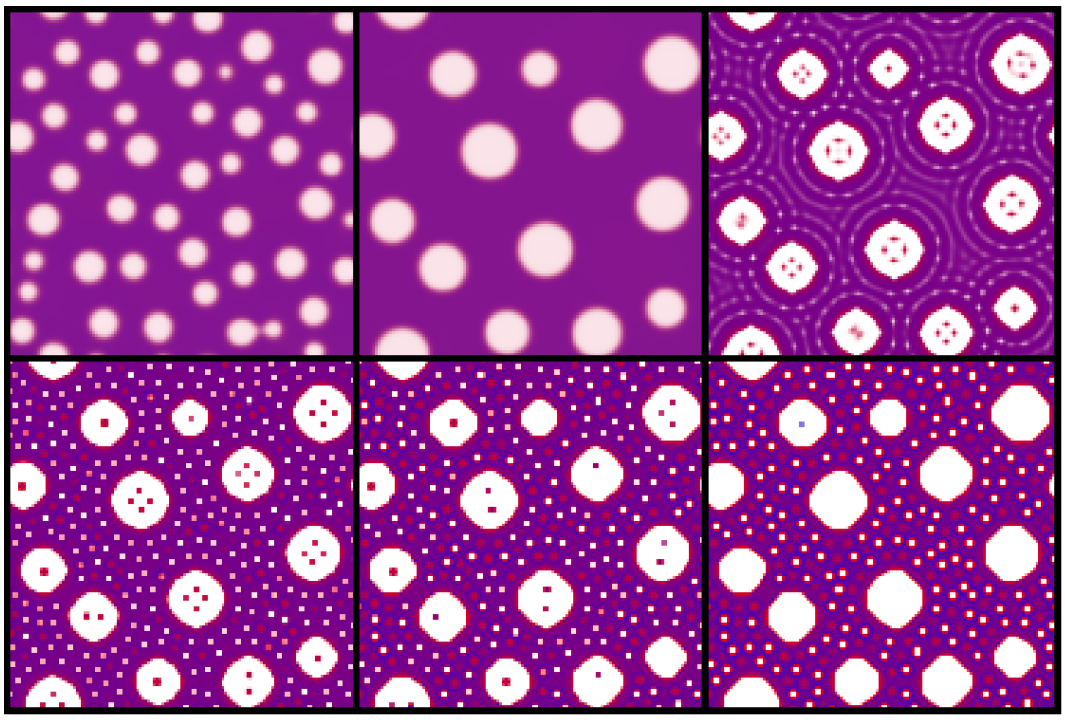

FIGURE 3.1: Time snapshots showing the local compositions throughout the system, as from numerics. For the colour scheme see Fig. 2.7 for details. The lighter portions of the system are gas bubbles, which are surrounded by a B-rich interface separating them from a liquid phase. Parameters: $p^A = p^B = 0.375$, $T_1 = 0.7$, $T_2 = 0.1$, $d = 0.15$, $w_s = 0$, and $L = 128$. From top left to bottom right, the snapshots are taken at $t = 4717$, 40000, 40009, 50705, 234997, and 3.3757×10^6. The secondary quench was performed at $t = t_2 = 40000$. The symmetries are a consequence of the lattice structure and of the low final temperature.

In Fig. 3.2 we can see the time evolution for the average area of primary domains. The areas have been calculated via image analysis[1] and are given in number of lattice sites enclosed by the domain's interface. In order to distinguish between primary and

[1]The image analysis has been performed using *Mathematica*'s function 'ComponentMeasurements' applied to a binary image obtained from our data; to construct the binary image we define that total densities below 0.5 constitute gas bubbles. Therefore the interfaces are mostly considered part of the liquid.

secondary domains we used the fact that the largest secondary domain remained at all times smaller than the smallest primary domain at t_2.[2] According to the Lifshitz-Slyozov (LS) law [96–98] the average linear domain size for coarsening with a conserved order parameter as here should increase as $l(t) \sim t^{1/3}$ in the asymptotic regime. This power law can be identified in the upper data in Fig. 3.2. Since we plot the area rather than linear size the graph shows exponent $2/3$. The asymptotic behaviour is reached during the final stages of the primary phase separation for $t < t_2$. Then the deep quench generates a plateau in the 'coarsening' dynamics, so that effectively it interrupts the coarsening of the primary domains. This interruption extends essentially across all of our simulation time after t_2, which is qualitatively consistent with the depth of the quench causing a drastic slowdown of the dynamics. Within the plateau in the plot that corresponds to the interrupted coarsening there is in fact a very slow growth because the primary bubbles still absorb gas from the tiny secondary bubbles as they disappear, but this is quantitatively a rather weak effect. Indeed the number of primary bubbles remains constant for all $t \geq t_2$ within our simulation time window, showing that primary coarsening is essentially halted during this period.

Fig. 3.3 shows snapshots for the same parameters, except that now we have $w_s = 1$. This effectively 'switches on' direct particle-particle swaps and so facilitates composition changes, leading to different morphological features. The secondary bubbles merge by collapsing one into the other, with the smallest ones collapsing first. (By "collapse" we mean that one bubble disappears by shrinking, with most of its gas being taken up by a neighbouring bubble.) Initially, the number of secondary bubbles increases very quickly from zero (domain formation following the spinodal regime) and then we have a long period of decrease. The rate of decrease slows over a long period (data not shown) as the remaining bubbles are no longer very close to each other and therefore cannot transfer gas so easily. In this process the interface material of the secondary bubbles that disappear becomes partly dispersed into the liquid and partly used to increase the interface lengths of surviving bubbles, rather than becoming trapped as long-lived composition heterogeneities. For the average area of these secondary domains, shown in Fig. 3.4, we initially have a

[2] For the $w_s = 1$ data, in order for this to be true we needed to use a slightly smaller region rather than the entire system.

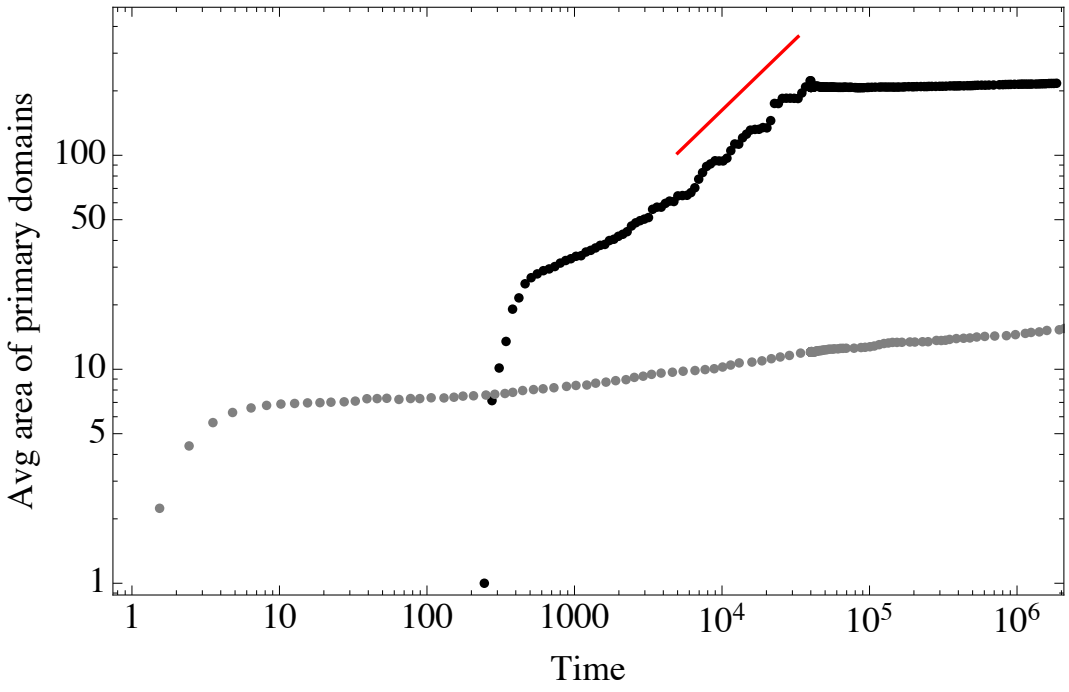

FIGURE 3.2: Log-log plot of the average area (in number of lattice sites) of primary domains, calculated via image analysis, versus time. The red solid line segment is proportional to $t^{2/3}$. The upper data come from the numerics shown in Fig. 3.1, where $T_1 = 0.7$ and $T_2 = 0.1$. They show a kink at the time of the second quench before a plateau of virtually constant area. The lower data are for a situation where there is no secondary temperature quench and we start directly with a quench to $T_1 = T_2 = 0.1$.

strong increase; subsequently, since bubbles become increasingly farther apart, we have that despite the faster dynamics ($w_s = 1$) their average area increases only slowly for a very long period. The slow rate of increase is partly due to the low temperature. In addition, the presence of the large primary bubbles with their low Laplace pressure counteracts the tendency of secondary bubbles to coarsen. Rather than reaching an asymptotic $t^{1/3}$ coarsening regime, the secondary bubbles are then expected to eventually shrink and disappear before coarsening of the primary bubbles resumes.

By comparison, for $w_s = 0$ we have after a similar long transient where the average area of secondary bubbles increases—and their number decreases as some of them shrink—a much longer period of essentially arrested behaviour; this period starts beyond the penultimate snapshot in Fig. 3.1 and lasts until the end of our simulation time window. (Data not shown.) We hypothesize that the slow kinetics of composition changes is again at play here. For example, it is more difficult for the system to increase the length of interfaces of secondary bubbles since interface material from neighbouring shrunk bubbles becomes

trapped as long-lived heterogeneities. This will favour gas liberated by the disappearance of secondary bubbles to go into the primary bubbles, where it can be taken up with a smaller increase in interfacial length.

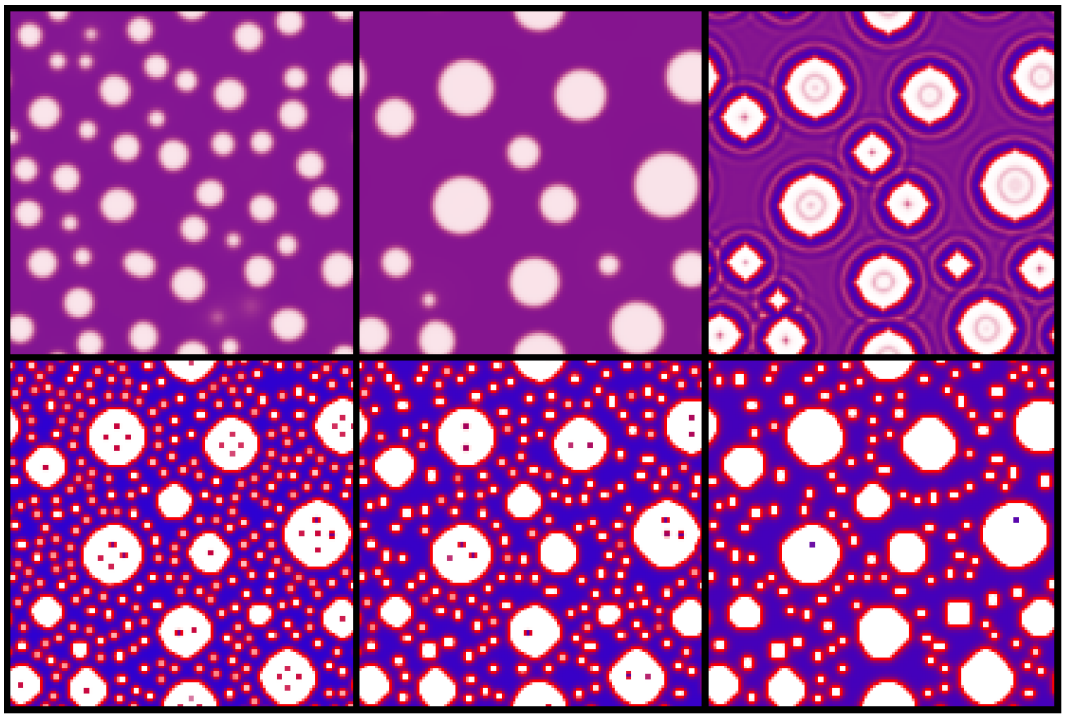

FIGURE 3.3: As Fig. 3.1 but for $w_s = 1$. Parameters: $p^A = p^B = 0.375$, $T_1 = 0.7$, $T_2 = 0.1$, $d = 0.15$, $w_s = 1$, and $L = 128$. From top left to bottom right, the snapshots are taken at $t = 4256$, 40000, 40003, 46220, 179285, and 3.3811×10^6. The secondary quench was performed at $t = t_2 = 40000$. The symmetries are a consequence of the lattice structure and of the low final temperature.

Interestingly, the evolution of the average area of the primary domains for $w_s = 1$ remains qualitatively similar to that for $w_s = 0$ in Fig. 3.2 (data not shown). The implication is that while secondary bubbles do collapse for $w_s = 1$, the amount of gas that such processes transport into primary bubbles – rather than other secondary bubbles – remains small here.

After the coarsening-interruption plateau, we expect for both $w_s = 0$ and $w_s = 1$ that at very late times the system will eventually resume coarsening of the primary bubbles, following a LS-law but with a much reduced prefactor due to the significantly smaller temperature. By this time all secondary bubbles will have disappeared.

To probe this issue further, we show the lower data in Fig. 3.2, which corresponds to a situation where we start directly at the low temperature $T_1 = T_2 = 0.1$, i.e. we perform

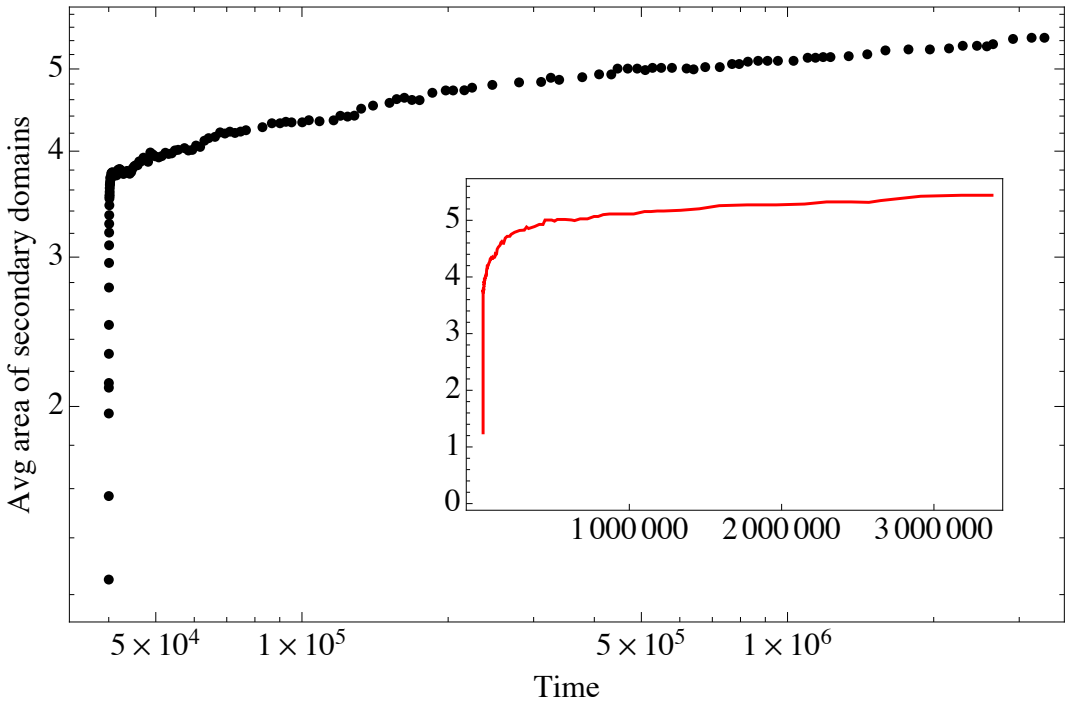

FIGURE 3.4: Log-log plot of the average area (in number of lattice sites) of secondary domains. The data is for the same data used in Fig. 3.3, where $T_1 = 0.7$ and $T_2 = 0.1$. Inset: linear scale, with points joined into a line to guide the eye.

a single quench. By the end of our simulation window this phase separation has not yet reached the LS-law coarsening regime as the bubbles are small and grow very slowly. Now, at sufficiently late times the low-T coarsening dynamics is expected to lose all memory of having started at higher T. Therefore the single-quench data should connect smoothly with the final coarsening curve of the two-step case. But even if the single-quench case reached the LS-law regime soon after the end of our simulation window, its prefactor shows that this would cross the two-step plateau only at a much longer time. This means that by the end of our double quench simulation window we are still far from the late-time edge of the coarsening-interruption plateau. This conclusion is valid for both $w_s = 0$ and $w_s = 1$.

Some other distinctions between the $w_s = 0$ and $w_s = 1$ cases can be seen by examining the snapshots in Figs. 3.1 and 3.3 closely. First, note that primary bubbles that are very close together might not leave enough space for a spinodal length to fit in between them. This effective confinement can prevent the spinodal growth of fluctuations and suppress secondary phase separation in the relevant regions of the system. Although rather difficult

to see in the numerical example for $w_s = 0$ in Fig. 3.1 (slightly easier to see in Fig. 3.5), this is what appears to happen for instance with the closest pair of primary bubbles in the left-hand side of the system: notice how the composition of the environment between those bubbles at $t = 234997$ is more similar to that of the primary liquid, consequently forming a very subtle 'bridge' that wets the two bubbles. This kinetic effect eventually disappears as composition equilibration progresses; in the fast dynamics for the $w_s = 1$ case it simply does not exist.

The liquid phase composition evolves in interestingly different ways indeed, depending on w_s. We point out the different morphologies directly after the second quench. For $w_s = 1$ the spinodal waves quickly lead to the formation of a substantially A-rich liquid phase and do so in a largely homogeneous manner. The enrichment in A-particles compensates for the existence of a large amount of strongly B-rich interfaces. In fact note that the formation of interfaces generally depletes B-particles from the liquid next to the interface. For the case $w_s = 0$ the composition changes involved in this depletion process are too slow to be observable and therefore the spinodal waves lead to a liquid without much fractionation, as we can see from the top-right snapshot (directly after $t = t_2$) in Fig. 3.1.

At later times (for $w_s = 0$) the secondary bubbles grow slightly, at the expense of smaller ones, and of course need vacancy input to do so. (In the Sigehuzi-Tanaka experiment [94] the growth of the secondary domains is also extremely slow.) As vacancies get into the bubbles we temporarily have regions of smaller density surrounding these domains. This allows for composition changes to happen faster than in the bulk liquid. Thus this contributes to the formation of A-rich regions surrounding the growing secondary bubbles while the rest of the system remains relatively poorly fractionated. (See Fig. 3.5. Note that in the regions between secondary bubbles there is depletion of B's from both sides.) We expect this composition-heterogeneous liquid to eventually become homogeneous again—this stage is beyond our simulation window. If it occurs at a point where there is still a large amount of strongly B-rich interfaces then we should expect to see a state similar to the A-rich homogeneous liquid that is formed shortly after the secondary quench in the case $w_s = 1$. Otherwise, the liquid might never become homogeneously A-rich: remember that at equilibrium almost all of the B-rich interface material will have

dispersed (we have only one domain) and the liquid is, again, only slightly fractionated rather than A-rich.

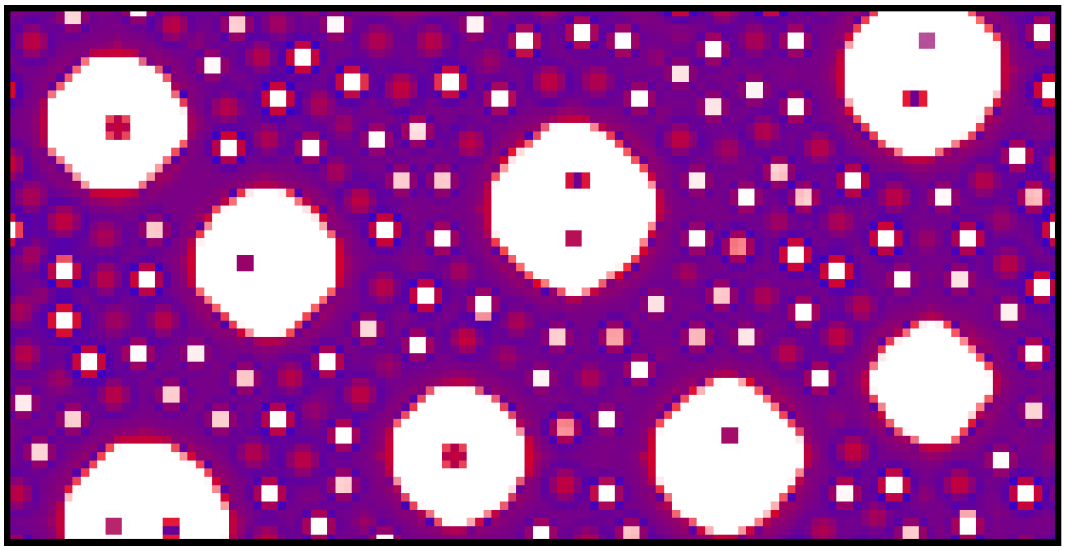

FIGURE 3.5: Lower half of bottom-centre snapshot ($t = 234997$) in Fig. 3.1.

In order to investigate the above and other related phenomena in more detail we will in the next section switch to a simpler set-up.

3.3 Phase separation from slab geometry

Now we consider a liquid domain in the form of a slab surrounded by vapour, and perform a single quench from that state. As anticipated in the introduction, this is similar to one of the geometries considered in a model of binary alloys in Ref. [54], where phase separation starts first at the slab-vapour interface, but the interaction parameters used in Ref. [54] lead to 'A-B' phase separation rather than a fractionated gas-liquid coexistence as in our case. Note that starting from a slab is equivalent to what one would obtain by taking $t_2 \to \infty$ in a double quench situation: only a single domain would be left at the time of the second quench, forming either a slab or a single circular domain in a finite system. (We can also think of the slab domain as the liquid between two big—and therefore locally flat—primary bubble interfaces.) Thus in this section we use the slab domain as our initial state to obtain a geometry that is simpler to analyse. Initially we will imitate the conditions of the simulations in Figs. 3.1 and 3.3 in order to calibrate and perform further analyses. Then

we will proceed to cases with higher final temperature and d where we will see additional effects.

3.3.1 Deep quench 'revisited'

Fig. 3.6 shows a deep quench simulation that replicates the physics seen above for $w_s = 0$. We start from an *equilibrated* slab-geometry liquid domain surrounded by a vapour phase. The initial liquid and vapour compositions as well as the other parameters match those at the time of the second quench in Fig. 3.1. In fact, we have prepared the system by equilibrating it at the first-quench temperature used for Fig. 3.1, and as a result it has quickly generated smooth slab-vapour interfaces. Then we started our phase separation experiment by quenching to $T = 0.1$, i.e. the second-quench temperature in Fig. 3.1. We can clearly see that 'spinodal waves' propagate from the slab-vapour interfaces towards the centre of the liquid. In the terminology used in Ref. [54], this is a consequence of 'surface' modes, and this phenomenon can be viewed as a case of 'surface'-directed spinodal decomposition [86, 99]. The decomposition fronts are spaced according to our calculated spinodal length. As long as the central part of the system has not yet been reached by a front it will remain homogeneous. The newly-formed gas stripes eventually start to break into bubbles as dictated by the bulk modes.

Note that the set of bubbles creates an 'ordered' structure, i.e. the domains are fairly regularly spaced. The behaviour is similar to that obtained for the two-step quench simulations with polymer blends in Ref. [89]. Here, however, this regularity is also long-lived. This can be seen from Fig. 3.7. We show on the left a snapshot of the system at a late time. On the right we show the corresponding average density profile along the cross-interface direction (i.e. normal to the slab-vapour interface); this will be useful for later comparison. Notice how spatially ordered the set of domains (plus long-lived patches) remains: even though the liquid is highly inhomogeneous in composition, the different structures essentially keep their positions for a long time as inherited from the original spinodal decomposition fronts.

The initial behaviour for $w_s = 1$ shown in Fig. 3.8 is structurally similar to that for $w_s = 0$, but with a much more fractionated homogeneous liquid (existing 'behind' the

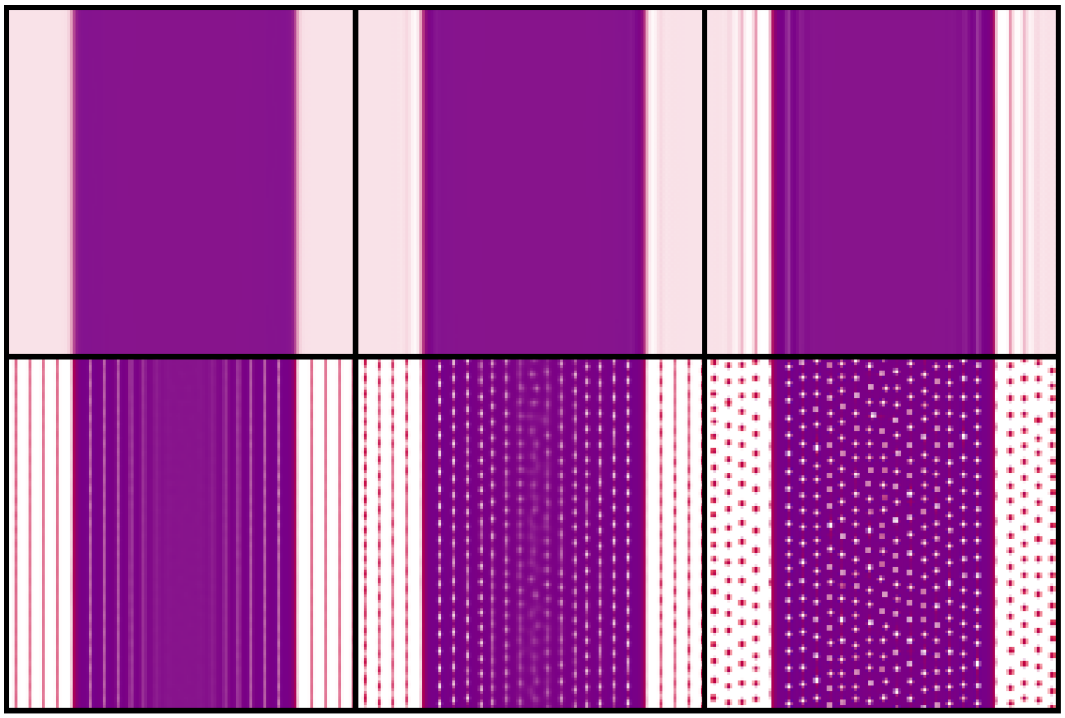

FIGURE 3.6: Time snapshots showing the local compositions throughout the system, as from numerics. For the colour scheme see Fig. 2.7 for details. The lighter portions of the system are gas bubbles. We start from an equilibrated slab-geometry liquid domain surrounded by a vapour phase. The initial liquid and vapour compositions as well as the other parameters match those at the time of the second quench in Fig. 3.1. Parameters: $d = 0.15$, $L = 128$, $w_s = 0$, and $T = 0.1$. (Composition before initial equilibration at $T = 0.7$: $p^A = 0.470$ and $p^B = 0.451$ for the slab liquid domain and $p^A = 0.0247$ and $p^B = 0.0955$ for the vapour. The slab extremes are placed at 18% and 82% of the horizontal simulation box side.) From top left to bottom right, the snapshots are taken at $t = 0$, 2.32, 7.10, 17.61, 22.65, and 60.06, counted from the moment of the quench to the final temperature.

decomposition front) as well as interfaces. However, once the smallest bubbles start to collapse as we have seen in Section 3.2, the regularity is destroyed gradually. This can been seen from the late-time snapshot and its corresponding average density profile in Fig. 3.9.

The spatial regularity in the set of newly-formed domains is a direct consequence of the fact that phase separation is triggered via spinodal decomposition fronts propagating from the slab-vapour interfaces. The 'spinodal waves', in turn, occur because the initial higher-T equilibration of the slab-vapour interfaces has removed all added fluctuations in the bulk phases—similarly to the double-quench simulations of a hydrodynamical model for polymeric blends in Ref. [90]—leaving the slab-vapour interfaces as the sole source of

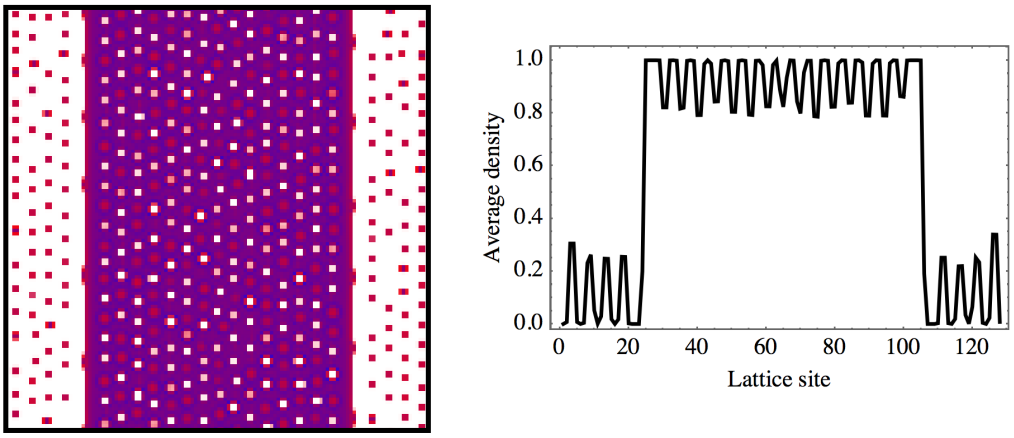

FIGURE 3.7: Left: as Fig. 3.6 but at $t = 86000$. Right: Corresponding average total density profile along cross-interface direction. That is, each horizontal point has associated a total density obtained by averaging over the vertical direction.

fluctuations. That is, even though noise has been added to the slab-geometry configuration, this has been done prior to the initial equilibration, resulting in 'noiseless' equilibrated phases, from which state no spinodal decomposition can occur except if started at the interface. In order to investigate the effects produced by this we have added noise back in at the moment of the final quench, as shown in Fig. 3.10. Notice how the distinct noise strengths result in the spinodal waves being able to travel different distances before bulk spinodal modes reach their nonlinear regime. This is similar to what can be seen in the off-critical 'A-B' vacancy-mediated phase separation simulations of binary alloys in Ref. [54]. (Like in that study we have also performed simulations starting from a 'droplet' geometry, which led to similar results.) It is worth pointing out that, because in their set-up the interaction energies are such that $\varepsilon_{AA} = \varepsilon_{BB}$, these 'spinodal waves' can occur only in their off-critical case, where the overall system becomes richer in one of the particle species; this leads to "$\mu_A \neq \mu_B$" and consequently to a quick formation of interfaces that are richer in one component. In our case this happens 'by default' as $\varepsilon_{AA} \neq \varepsilon_{BB}$.

The bottom-right snapshot in Fig. 3.10 is for a simulation with a *non-equilibrated* initial slab configuration but with noise added as usual. Notice that, even though we do not start with previously formed smooth slab-vapour interfaces, the system (at the point where domains start to form) looks essentially the same as its equilibrated counterpart (bottom-left snapshot). This is because at this noise strength the interface (be it smooth or 'sharp') does

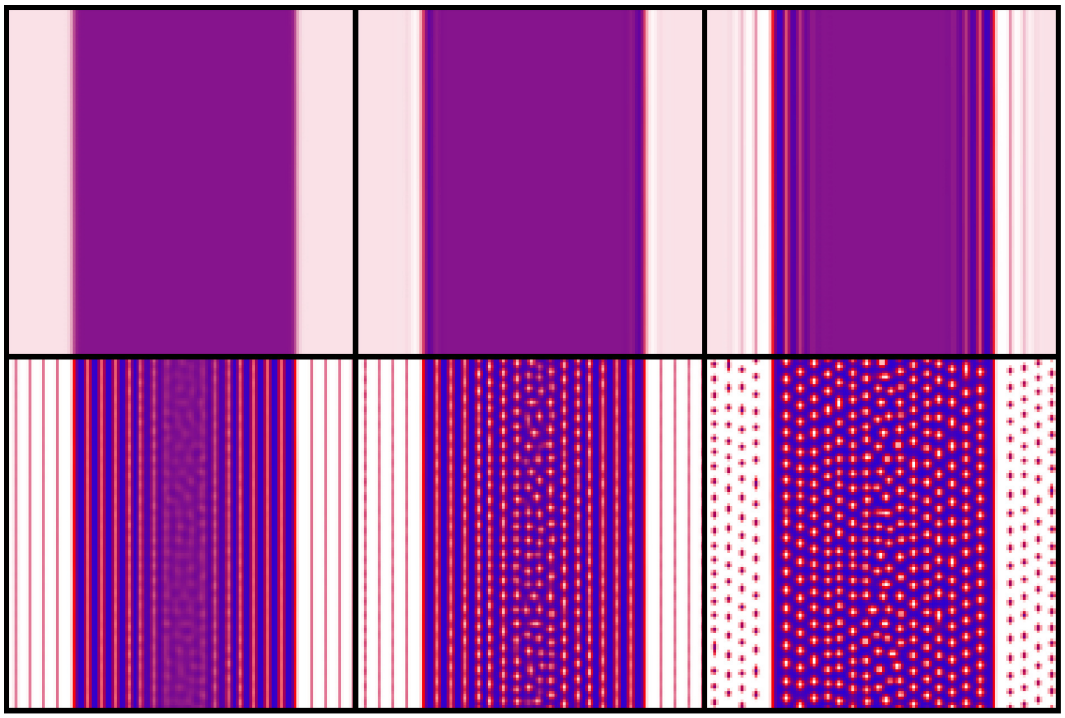

FIGURE 3.8: Analogue of Fig. 3.6 for $w_s = 1$. From top left to bottom right, the snapshots are taken at $t = 0$, 1.89, 6.41, 14.93, 18.49, and 43.67, counted from the moment of the quench to the final temperature.

not play the role of sole fluctuation source, with fluctuations starting to grow 'everywhere' simultaneously, instead. We point out that in Ref. [54] it has been analytically derived that the 'thickness' of surface-directed 'structures' depends logarithmically on the strength of the initial noise; this is consistent with what we see in Fig. 3.10.

The above discussion shows the importance of considering noise in double quench theories, since otherwise the primary phases have no noise and therefore the primary domains would act as the sole sources of fluctuations. The exact noise strength will change with time, depending on temperature and composition, and this will dictate whether the spinodal waves will manifest or not, and consequently what is the structure of the set of secondary domains. As we have seen above, whether this is structure is then long-lived will depend on the presence of slow-fractionation effects.

3.3.2 Higher temperature

We now turn our attention to 'secondary' phase separation at higher temperatures rather than after deep quenches. Here we will choose a second quench temperature high enough

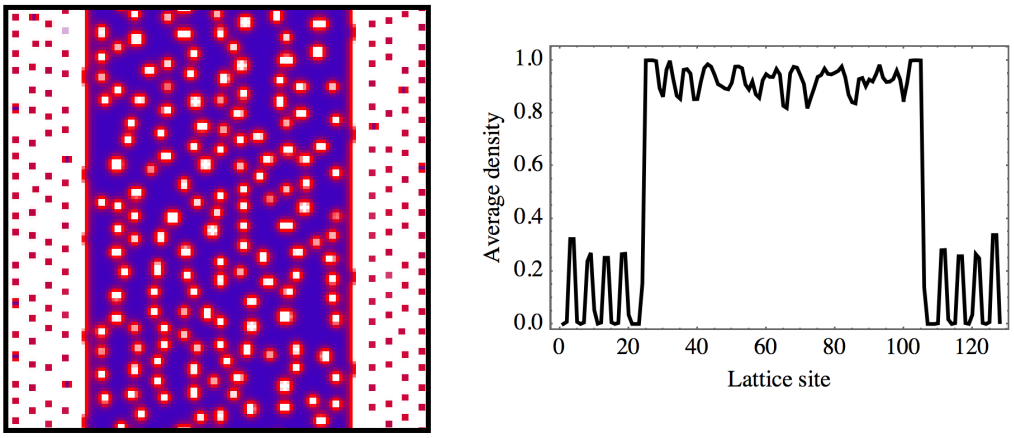

FIGURE 3.9: As Fig. 3.7 but for $w_s = 1$. Taken at $t = 86000$.

for the 'primary' gas phase not to undergo further phase separation while still allowing the dense 'primary' liquid to phase separate. In order to be able to increase the final temperature while keeping the liquid well within the spinodal region we will increase the interaction strength 'polydispersity' parameter d. Because Fig. 3.10 shows that by increasing the initial noise strength at the moment of the final quench one suppresses the 'surface'-directed spinodal waves, we will in this higher temperature context simplify the simulations by ignoring effects from a previously formed smooth interface. This will be done by considering non-equilibrated, 'sharp' slab-vapour interfaces rather than equilibrating them first. The two situations should generally be equivalent if the bulk noise strength is high enough. With these choices we will be able to show the relevant physics in its simplest setting.

Fig. 3.11 shows a simulation for $w_s = 0$ where both the initial phases, the dense liquid and the dilute vapour, contain equal amounts of A's and B's. After the temperature quench is performed, a smooth interface with the outside vapour is formed quickly and after some time spinodal decomposition starts in various places simultaneously. Also, a second layer rich in A's is quickly formed right next to the smooth interface, from inside the slab. Consistent with our discussion in Section 3.2, the formation of this A-rich zone has two contributing causes: (i) generally in our system interfaces have mainly B particles in it, so the formation of the interface will transiently deplete B's from the liquid outside

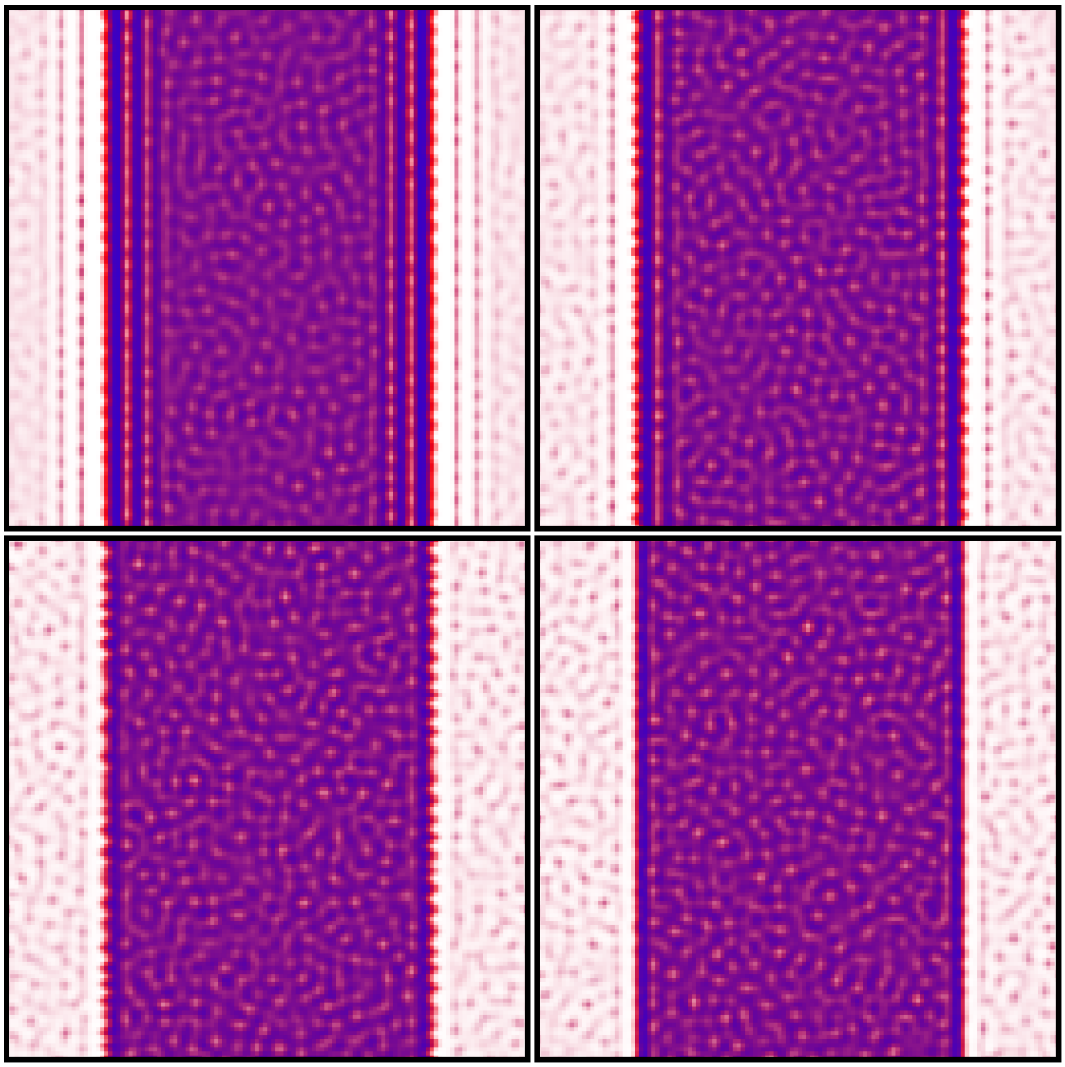

FIGURE 3.10: Parameters as Fig. 3.8 but each early-time snapshot here corresponds to a run with a different strength of the noise added to the initial state, i.e. at the time of the final temperature quench. From top left to bottom right, the zero-mean initial noise has standard deviations 0.01%, 0.1%, 1%, and 1% again, but in the bottom-right snapshot the slab-vapour interface has not been previously equilibrated. All snapshots are taken at the time within the spinodal regime where domains start to form. In the same order, the snapshot times are $t = 7.52$, 5.53, 2.93, and 3.32, counted from the moment of the quench to the final temperature.

the interface; (ii) if the new gas phase is significantly enriched in B's, or conversely depleted in A's compared to the initial phase, then the surplus A particles will diffuse into the liquid phase and create an excess of A's there. Notice that overall there is a density increase in the liquid, making the slab thinner as time passes. Again, we can see B-rich long-lived patches from the interfaces of 'dead' bubbles, but we notice that the A-rich layer is also long-lived. Over time it gradually becomes thicker but also less fractionated (and

so less distinguishable from the bulk liquid); ultimately the layer dissolves and so do the bubbles, with the liquid close to a homogeneous state. We note that for deep quenches as in Section 3.2 the contribution (ii) to the A-rich layer above is not existent as there are essentially no particles remaining in the gas phase (even at equilibrium the gas will be extremely dilute). Also, the diffusive exchange with the surrounding gas has to have time to form an A-rich zone before spinodal fluctuations grow; this situation arises after performing a shallow quench, in which case the spinodal dynamics is generally slower—for both $w_s = 0$ and $w_s = 1$ cases—than it is for a deep quench. (This relation between the spinodal timescales remains even taking into account the different value of d here, as we have checked by calculating the spinodal rates explicitly.)

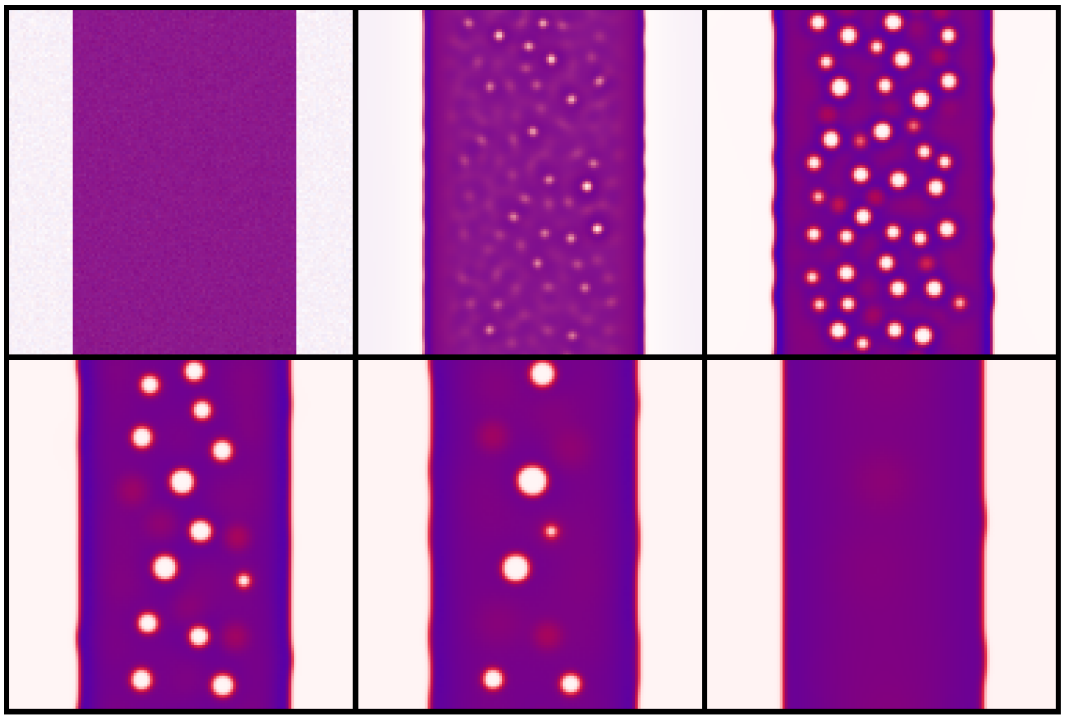

FIGURE 3.11: Time snapshots showing the local compositions throughout the system. We start from a slab-geometry 'liquid' domain surrounded by a vapour. Parameters: $d = 0.25$, $L = 128$, $w_s = 0$, and $T = 0.4$. Composition before quench: $p^A = p^B = 0.45$ for the slab liquid domain and $p^A = p^B = 0.03$ for the vapour. The slab extremes are initially placed at 18% and 82% of the horizontal simulation box side. From top left to bottom right, the snapshots are taken at $t = 0$, 131, 2089, 18445, 41111, and 122065, counted from the moment of the quench to the final temperature.

In the case $w_s = 1$ shown in Fig. 3.12 we can initially see an A-rich layer as well. Its thickness is related to the spinodal length, which leads to domains being able to grow only from a certain distance to the slab-vapour interface. (Notice that fluctuations start to grow

simultaneously everywhere within a region of composition nearly 50–50%.) In this case, however, the liquid quickly becomes homogeneous. Since there is initially a good amount of bubble interfaces—which are rich in $B's$—the bulk liquid ends up being homogeneously slightly enriched in A's for a long period of time (see Fig. 3.12 closely). Eventually the bulk liquid reaches a less fractionated composition and the bubbles are reabsorbed.

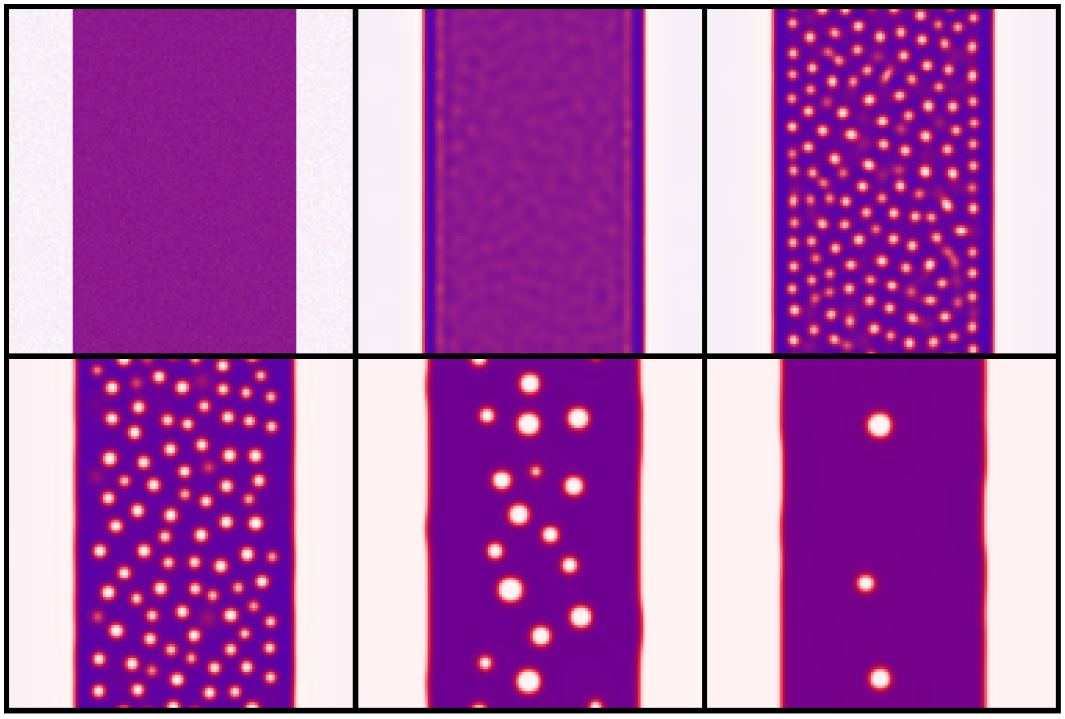

FIGURE 3.12: As Fig. 3.11 but for $w_s = 1$. From top left to bottom right, the snapshots are taken at $t = 0$, 116, 1703, 15791, 36479, and 87289, counted from the moment of the quench to the final temperature.

We notice further an interesting phenomenon that is only possible at high enough temperatures. In the case $w_s = 0$, by looking at the time where the bubbles are still in their initial growth regime (see Fig. 3.13), we can observe the existence of a 'dead zone', i.e. a 'stripe' where no composition fluctuations grow, located next to each A-rich layer. As the spinodal dynamics is slower for $w_s = 0$, we see that by the time domains start to form a wider region of liquid is formed near the interface; it has mostly density close to the equilibrium value and is thus above the density of even the (upper) annealed spinodal. This region is therefore no longer unstable to small composition fluctuations, so these will be damped rather than grow into bubbles. In fact, notice the two 'humps' in the average total density curve near the slab boundaries in the right-hand side of Fig. 3.13; they show that

the region has become sufficiently dense—and if we move towards the centre of the system from these humps we still remain (over some length) at total densities that are very close to the annealed spinodal, therefore making the growth rates very small and leading effectively to a wide 'dead zone'. This can also be seen from the variance of the total density: it is zero in a wide region near the boundary. This is another interesting manifestation of Warren's scenario: the spinodal dynamics is slow because we are mostly outside at least the quenched spinodal (see right-hand side of Fig. 3.13 again, where we show the composition-dependent spinodal densities as cross-interface profiles); therefore in the liquid region near the interface the fast process of density equilibration 'wins' and stabilizes the system before fluctuations can grow. In a one-component system this cannot happen as the timescale of the spinodal dynamics is directly set by the density equilibration. As expected, the effect is destroyed by making $w_s = 1$ on (see Fig. 3.14 for comparison).

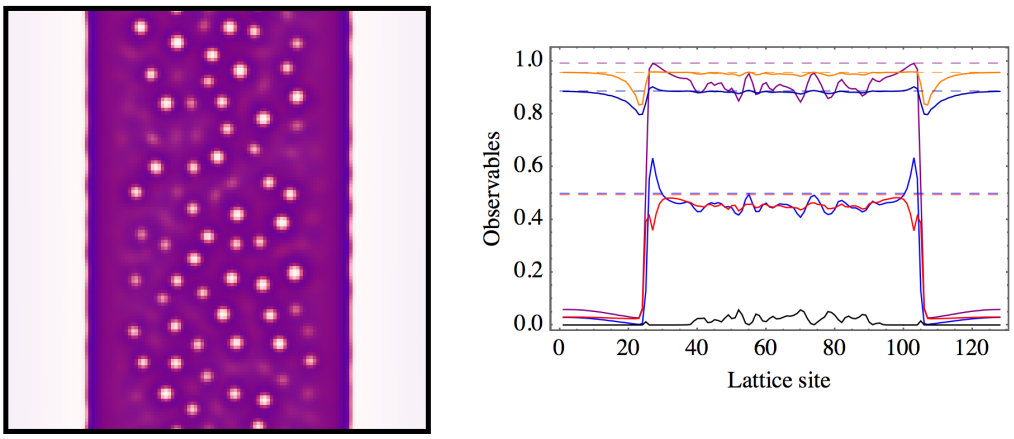

FIGURE 3.13: Left: as Fig. 3.11 but at $t = 172$. Right: Several observables profiles along cross-interface direction (same time). For each observable, we have that each horizontal point has associated the observable value obtained by averaging over the vertical direction. Observables (solid lines)—also listed in Table 3.1—from top to bottom along the y-axis: composition-dependent average annealed spinodal density (orange), composition-dependent average quenched spinodal density (darker blue), average total density (purple), average p^B (red), average p^A (lighter blue), and variance of total density (black). Dashed lines, from top to bottom along the y-axis: liquid equilibrium total density (purple), overall liquid annealed spinodal density (orange), overall liquid quenched spinodal density (darker blue), liquid equilibrium p^A (lighter blue), and liquid equilibrium p^B (red). All spinodal densities are from the high-density branch.

Observables (solid lines)	**Colour**
Composition-dependent average annealed spin. density	Orange
Composition-dependent average quenched spin. density	Darker blue
Average total density	Purple
Average p^B	Red
Average p^A	Lighter blue
Variance of total density	Black

TABLE 3.1: Observables (solid lines) in the right-hand side of Fig. 3.13. From top to bottom along the y-axis.

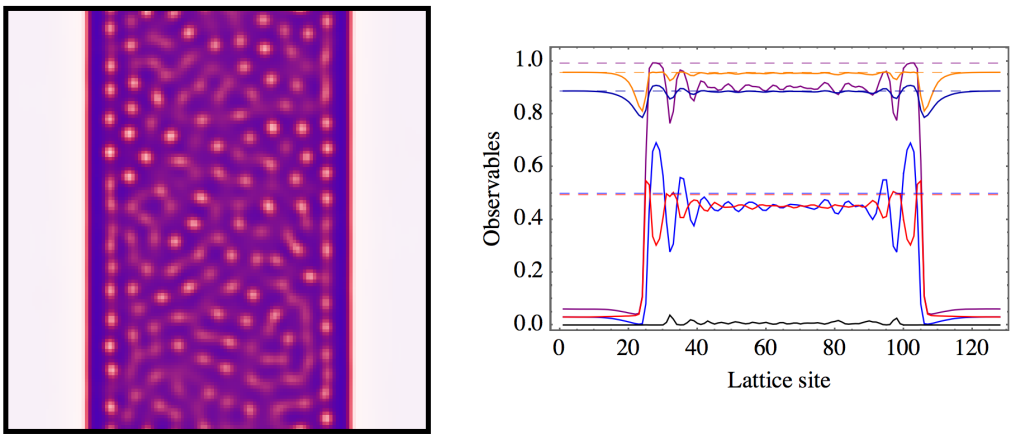

FIGURE 3.14: As Fig. 3.13 but for $w_s = 1$ and at $t = 50$. Observables (solid lines)—also listed in Table 3.1—from top to bottom along the y-axis: composition-dependent average annealed spinodal density (orange), composition-dependent average quenched spinodal density (darker blue), average total density (purple), average p^B (red), average p^A (lighter blue), and variance of total density (black). Dashed lines, from top to bottom along the y-axis: liquid equilibrium total density (purple), overall liquid annealed spinodal density (orange), overall liquid quenched spinodal density (darker blue), liquid equilibrium p^A (lighter blue), and liquid equilibrium p^B (red). All spinodal densities are from the high-density branch.

3.4 Secondary quench into three-phase region

We return finally to the double quench case in bulk geometry. Here we enter the three-phase region by quenching deep enough. While the kinetics of phase separation after quenches into a three-phase coexistence region has been studied previously [65], the range of parameters investigated was relatively limited and to the best of our knowledge the double quench case has not been considered in the literature. Here we consider a higher d than in the discussion for the secondary quench into the two-phase region; therefore we will be able to choose higher final temperatures and still be in the three-phase region.

Fig. 3.15 shows our results for a double quench experiment into the three-phase region. In this case the fast dynamics ($w_s = 1$) induces an interesting wetting phenomenon whereby the primary domains eventually become connected via strongly fractionated interfaces that have been formed from the secondary bubbles. This is different from the wetting 'bridges' described in Section 3.2 in that here these 'filaments' persist (and thicken) due to a thermodynamic driving force: they eventually turn into the third, B-rich phase.

Figs. 3.16 and 3.17 show simulations for the cases $w_s = 0$ and $w_s = 1$, respectively, performed for much larger t_2 and significantly higher T_2, but still low enough for the second quench to land in the three-phase region. They indicate that, until the 'third-phase' filaments start to form and connect primary bubbles, the morphology evolution proceeds generally similar to the two-phase cases in Section 3.2 (see Figs. 3.1 and 3.3). In particular, we expect indeed that for $w_s = 0$ the behaviour for the 'two-phase' and 'three-phase' cases should look generally the same until the liquid phase becomes homogeneous enough to form filaments of the B-rich phase: in the final snapshot in Fig. 3.16 we can already see a clear broadening of the interfaces as the third phase starts to get formed. We can even see that one of the primary bubbles, which has a 'protuberance' in addition to its round shape (from the merger between two rounded domains), begins to form a broader interface, and possibly filaments, quicker than the other bubbles. This could be interesting to explore in future work, by simulating a 'three-phase' final quench starting from a controlled geometry of 'primary' domains. At any rate, in this $w_s = 0$ case the formation of filaments will generally take much longer; therefore it would be interesting to see the final morphology at even longer times in future studies.

3.5 Conclusions

In this chapter we have shown how composition heterogeneities driven by kinetic effects arise in a variety of forms in phase-separating colloidal mixtures. Our results supplement Chapter 2 and constitute additional theoretical evidence that polydisperse phase separation can proceed rather differently from its monodisperse counterpart due to crowding effects on the kinetics of compositions across the system. Here we have looked at the phase separation process following a secondary temperature quench into the two- and

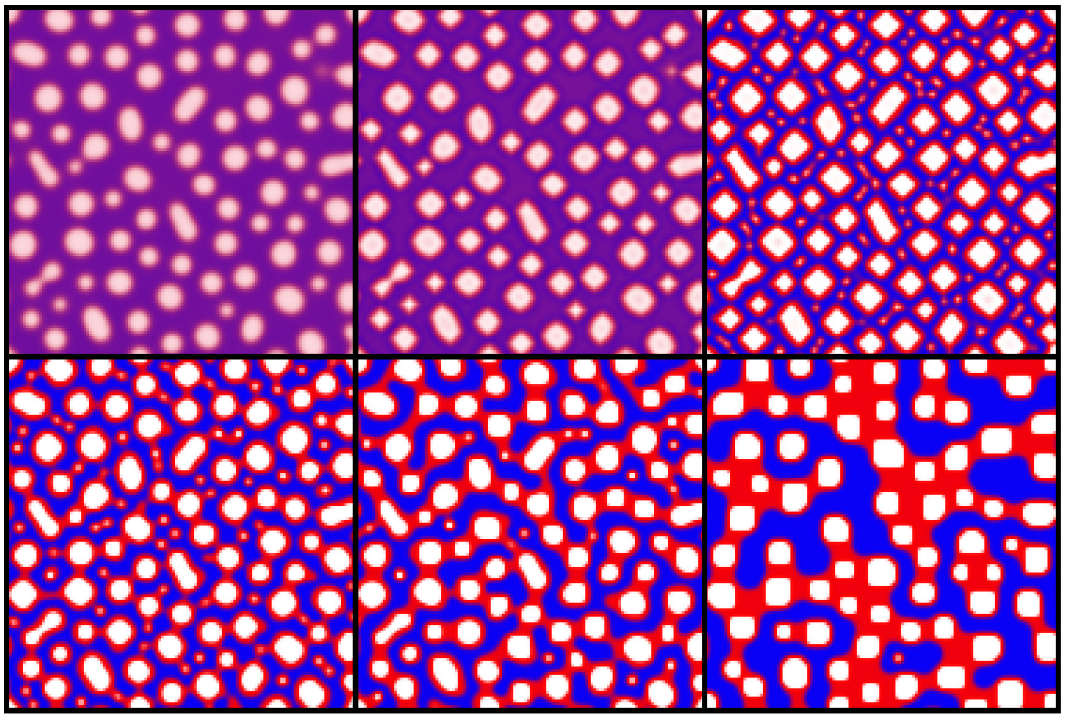

FIGURE 3.15: As Fig. 3.3 but for parameters which place the final system into the three-phase coexistence region. Parameters: $p^A = p^B = 0.375$, $T_1 = 0.7$, $T_2 = 0.15$, $d = 0.25$, $w_s = 1$, and $L = 128$. From top left to bottom right, the snapshots are taken at $t = 1500$, 1501, 1510, 1597, 1914, and 225702. The secondary quench was performed at $t = 1500$. The symmetries are a consequence of the lattice structure and of the low final temperature.

three-phase regions. Secondary domains grow inside the primary phases, but they never actually get to coarsen: they are eventually reabsorbed through the primary domains interface, as in the incompressible polymeric case of Ref. [89].

Here, however, for a deep second quench, the coarsening of the primary domains gets interrupted. The morphology of the liquid formed from the secondary phase separation changes with the kinetics. Also, we investigated the case of a slab surrounded by vapour, which can be interpreted as equivalent to waiting an infinite amount of time before performing the second quench into the two-phase region in a two-step quench experiment. 'Spinodal waves' form as a surface-directed phenomenon, and the decomposition fronts eventually break into secondary bubbles. In the case with slow composition changes, this leads to *long-lived* regularity in the spatial arrangement of the secondary domains. As already pointed out in Ref. [89], this can inspire strategies to develop regular morphologies that may have unusual physical properties. The fact that in our case this regularity is long-lived generates further opportunities to obtain new structures in soft matter systems.

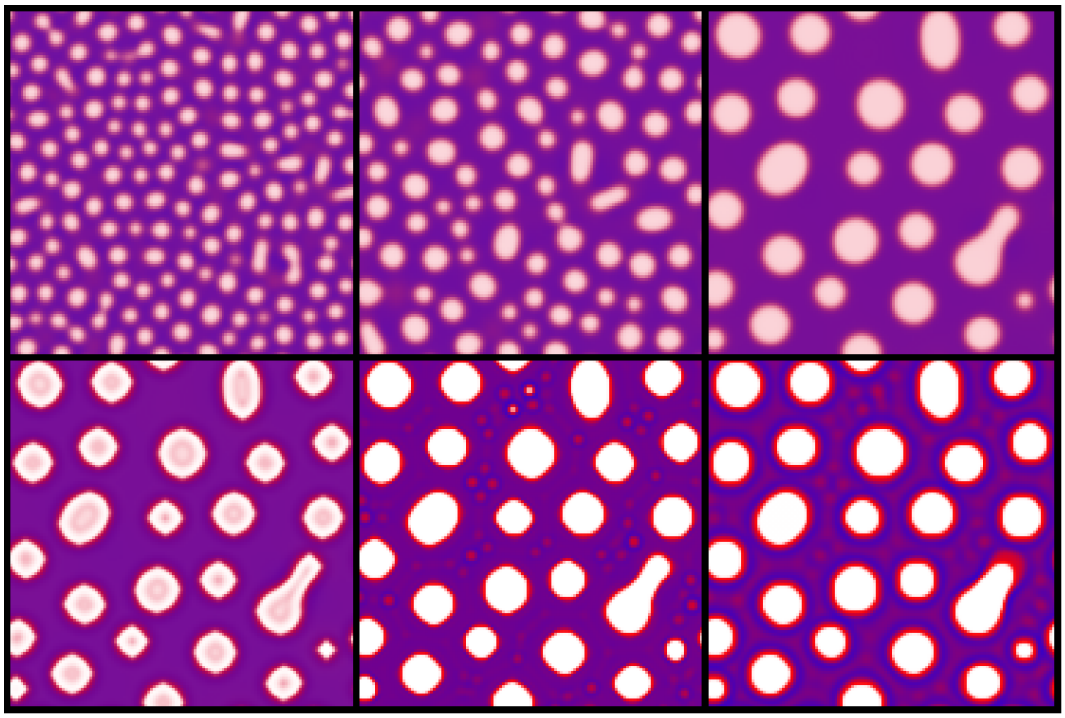

FIGURE 3.16: Parameters: $p^A = p^B = 0.375$, $T_1 = 0.7$, $T_2 = 0.20$, $d = 0.25$, $w_s = 0$, and $L = 128$. From top left to bottom right, the snapshots are taken at $t = 349$, 1992, 20000, 20004, 26177, and 408307. The secondary quench was performed at $t = 20000$. The symmetries are a consequence of the lattice structure and of the low final temperature.

The formation of spinodal waves from the initially equilibrated slab-vapour interfaces is affected by the amount of noise existent at the time of the final quench. At higher temperatures we have seen that a zone rich in the strongest-interacting species can form because the diffusive exchange with the surrounding gas has time to form such a zone before spinodal fluctuations grow. This is a result of the depletion of the more weakly-interacting particles, which flow into the gas. When we have slow composition changes, this layer turns into a significantly more long-lived composition heterogeneity. Also, we showed the existence of a 'dead zone' where spinodal decomposition does not occur. This is a further manifestation of Warren's two-stage scenario. Finally we presented our simulations for the case of a second quench into the three-phase region, where we observed the formation of filaments out of the primary domains; they wet and connect the primary domains and eventually turn into the third phase.

In future work on deep secondary quenches we would like to investigate how the time length of the coarsening-interruption plateau depends on effects of slow composition changes, and how the coarsening is restored as we approach the LS law. For the

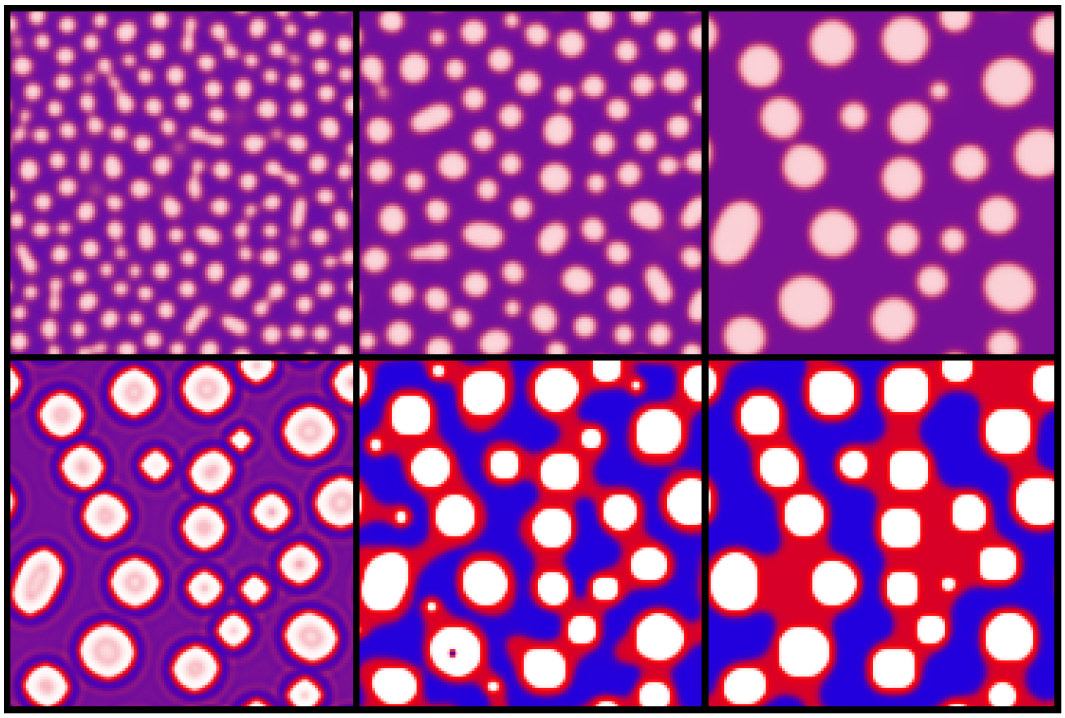

FIGURE 3.17: As Fig. 3.16, but for $w_s = 1$. Parameters: $p^A = p^B = 0.375$, $T_1 = 0.7$, $T_2 = 0.20$, $d = 0.25$, $w_s = 1$, and $L = 128$. From top left to bottom right, the snapshots are taken at $t = 326$, 1816, 20001, 20005, 24515, and 190388. The secondary quench was performed at $t = 20000$. The symmetries are a consequence of the lattice structure and of the low final temperature.

higher-T slab case, one could check how the 'dead zone' is affected by nucleation and growth. In this case even though spinodal decomposition of 'sizes' is not present in that region there could still be a situation where nucleation and growth takes over the phase separation process, effectively destroying the 'dead zone'. The presence of spinodal waves for low noise strength at the time of a secondary quench also adds to the importance of incorporating nucleation and growth effects. In the three-phase double quench case, we would like to see further evolution of the morphology for $w_s = 0$ by running even longer simulations. Also, transporting this three-phase dynamical problem to controlled geometries of the primary interfaces that include e.g. protuberances could constitute an effective method for analysing in a simple way the dynamics of filament formation, at least for $w_s = 1$. More specifically, it would be interesting to look into the dynamical process by which two primary liquid domains become connected. Finally, it will also be interesting to see how some of the effects investigated here manifest themselves in off-lattice models.

Chapter 4

Critical phase behaviour in multi-component fluid mixtures

4.1 Introduction and overview

The present chapter investigates how an arbitrary polydisperse fluid in the liquid-gas coexistence region behaves near its liquid-gas critical point (CP). Our development is valid for any number of particle species regardless of the nature of interparticle interactions, and therefore applies to generic multi-component mixtures. We will mostly use the term 'polydisperse' for such systems and this should then be read as including both genuinely polydisperse systems such as colloids, where the number of species is effectively infinite, and mixtures with a finite number of components.

To build intuition, we recall first the basic fact that liquid-gas phase-separated polydisperse fluids typically exhibit fractionation, where the overall number of particles from any given species is distributed unevenly across coexisting phases (i.e. none of the 'daughter' phases has a composition equal to that of the 'parent' phase). One therefore expects – as we will find – that the critical behaviour of such polydisperse systems is much richer than that of their monodisperse counterparts. For example, consider the case of phase separation starting from a parent phase with a fixed shape of its size distribution. (We will use the term 'size' generically to refer to any polydisperse attribute.) In this scenario a number of different characteristic loci can be defined in the phase diagram. The cloud curve is the one tracing temperature against the overall (parent) density where phase separation first occurs; similarly, the shadow curve records the density of the corresponding incipient

phase [17]. The critical point is located at the intersection of these two curves, rather than at the maximum as in the monodisperse case, where cloud and shadow curves collapse onto a single curve, the standard binodal. If one fixes a parent density one can alternatively study the evolution of the coexisting densities as temperature is lowered, or that of the fractional volumes occupied by the coexisting phases. We will discuss further loci of interest below, in particular ones determined by fixing to arbitrary values the fractions of system volume occupied by the two coexisting phases. This generalises the notion of cloud and shadow curve where these fractions are 1 and 0, respectively.

To motivate the relevance of 'complete scaling' (see below) to our analysis, we give an overview of the development of theories for the so-called 'diameter' of a fluid. This can be defined, for either monodisperse systems or mixtures, as

$$\frac{n_+ + n_-}{2} \tag{4.1}$$

where $n_\pm$ are the total number densities of the two coexisting phases obtained on cooling below the critical point. The temperature dependence of this quantity defines a curve in the phase diagram that has historically played an important role in the context of fluid criticality. In the nineteenth century this dependence was described by the 'law of rectilinear diameter', i.e.

$$\bar{n} \equiv \frac{\check{n}_+ + \check{n}_-}{2} \sim |t| \tag{4.2}$$

This is expressed here in terms of normalised deviations $\check{n} \equiv (n - n_c)/n_c$ and $t \equiv (T - T_c)/T_c$ from the critical density (n_c) and temperature (T_c). In the case of monodisperse fluids, such a linear relation between $\bar{n}$ and t can be obtained theoretically via, for example, the van der Waals equation of state.

However, even for monodisperse fluids, discrepancies between experimental data and the rectilinear law were eventually found in some fluid systems [100–102]. A natural hypothesis is that this is due to critical fluctuations, which are treated only approximately in mean-field approaches like van der Waals. To include these, one can construct a scaling formalism that essentially maps three-dimensional Ising critical behaviour onto its fluid

counterpart [103–107]. The rationale for such a mapping is the notion of universality generated by the diverging lengthscale of fluctuations at the critical point. The mapping expresses Ising thermodynamic variables as functions of fluid thermodynamic variables, allowing one to obtain the equation of state of a fluid in the vicinity of a CP. In particular, using the correspondence between the (monodisperse) lattice-gas fluid model and the Ising model, each independent thermodynamic variable in the Ising model is expressed in terms of a single fluid counterpart [103–105]. This simplest version of a mapping to an Ising scaling theory gives a rectilinear diameter in the sense that a plot of t against $\bar{n}$ is a straight line, though this line is constrained to be vertical ($\bar{n} = 0$) because of the particle-vacancy symmetry of the lattice gas [103, 108]. In order to devise a more flexible mapping framework, Rehr and Mermin introduced 'revised' scaling [106]. Here each independent Ising thermodynamic variable (temperature, magnetic field) is a function of *all independent* fluid thermodynamic variables (temperature, chemical potential): the thermodynamic fields have been 'mixed', producing 'asymmetric' fluid criticality. The leading-order behaviour for the diameter in this case comes out as $\bar{n} \sim |t|^{1-\alpha}$, where α is the universal critical exponent of the specific heat. This prediction agrees with experimental data for some fluid systems but still leaves out a number of other situations [109]. It was only after the beginning of the current century that the formalism known now as 'complete' scaling was introduced [107], whereby in the critical region each Ising scaling variable – temperature, magnetic field and (the singular part of the) thermodynamic potential – is expressed as a combination of *all* relevant thermodynamic variables of the fluid (temperature, chemical potential and pressure). This introduces 'pressure mixing', in the sense that the fluid pressure now appears in the expressions for all Ising thermodynamic variables. For the diameter, the complete scaling approach predicts, in addition to the $1 - \alpha$ term, a new, more singular contribution, namely $\bar{n} \sim |t|^{2\beta}$ where β is the critical exponent for the spontaneous magnetisation. There are experimental data for monodisperse fluid systems which support this prediction [108].

Since then a number of complete scaling studies have been produced, but only a few of them have looked at the behaviour of fluid *mixtures*. This is an important gap for soft matter, where multi-component systems are much more common than one-component

ones [1,3,12]. In Refs. [110] and [111] the case of a binary mixture is considered, but there the fluid pressure is controlled; in Ref. [110] this is done by considering an incompressible fluid mixture setup, whereas in Ref. [111] pressure effects are included only indirectly via their effect on mapping coefficients, in such a way that the pressure is effectively fixed. The scaling behaviour one then predicts is essentially that of a monodisperse system, though with quantitative changes in coefficients that affect e.g. in which direction the diameter curves [111].

Here we develop a complete scaling framework for generic multi-component fluids (not only binary mixtures) where the overall number density of particles is fixed rather than allowed to fluctuate at fixed pressure; the overall composition (fraction of particles belonging to each species) is also fixed. This is the natural setting for colloids and other soft matter fluids, where density is easily fixed by the amount of dilution using a solvent. Controlled pressure, which is common for atomic and molecular fluids, would correspond to the more unusual situation of fixed *osmotic* pressure for colloids. In addition to obtaining new results for the 'diameter', we look at a comprehensive set of other phase-diagram curves. In Refs. [112] and [113], Belyakov *et al.* developed a similar framework for multi-component systems with fixed composition, but they employed their results to create a fitting technique for experimental data near the critical point rather than investigating as we do the scaling exponents of the various characteristic curves in the phase diagram of a mixture. (Note also that in Ref. [112] the effects of complete scaling were not included explicitly, although as we show below this does not change the qualitative scaling form of the cloud curve.)

We will consider in this chapter a generalisation of cloud and shadow curves that reveals interesting structures inside the coexistence region. To motivate this, note first that in the monodisperse case one can define the diameter in at least two distinct, *equivalent* ways. The usual one is to define the diameter as the temperature-dependent midpoint of the phase coexistence region, i.e. $(\check{n}_+ + \check{n}_-)/2$. The coexisting densities can be generated by cooling a system with the critical parent density n_c. Alternatively, one can define the diameter as the parent density that produces, at each temperature, two phases each occupying half the system volume: due to the lever rule, which expresses particle conservation,

this parent density must then be the average of the two coexisting densities.

In the polydisperse case, we will see below that these two definitions are *not* equivalent, due to fractionation effects. We will refer to the first construction as 'midpoint diameter', defined as the average density of coexisting phases obtained by cooling a critical parent system. For the second definition we will use the term 'equal volume diameter'. Experimentally this curve could be obtained by fixing density and decreasing temperature from outside the coexistence region: in this process one crosses the cloud curve, where the split of fractional volumes between the coexisting phases is 100–0%, and then has to cool further until the split becomes 50–50%. Generalising this construction, we will consider below the 'fixed fractional volume' loci in the phase diagram where the parent density is chosen at each temperature such as to produce a *fixed* split of fractional volumes, say 80–20%, between the coexisting phases. We will see that the two different definitions of the diameter and the fixed fractional volume lines, which to our knowledge have not been analysed before, provide useful probes of fluid mixture critical behaviour.

In summary, in this chapter we use a complete scaling theory to relate polydisperse criticality to standard 3D Ising criticality, and thus to predict the scaling of the various lines in the phase diagram. We will investigate which nonlinear field mixing terms need to be retained to account properly for fractionation effects, and will point out observables, distinct from the Yang-Yang anomalies used previously [107], that could be useful to detect potential pressure mixing effects.

The remainder of this article is structured as follows. In section 4.2 we set up the complete scaling theory and derive the key relations between the thermodynamic variables. In section 4.3 we work out the general conditions from which the properties of coexisting phases can be determined. Section 4.4 contains our discussion of constant fractional volume lines. These include the cloud curve and, via the density of the coexisting phases, also the shadow curve. In section 4.5 we pause briefly to discuss in which limit our results reduce to the monodisperse case and how this leads to qualitatively different scaling behaviour. Resuming the discussion of characteristic loci in the phase diagram, the scaling behaviour of the (conventional, fixed parent density) coexistence curves is discussed in section 4.6. Then in Section 4.7 we verify our analytical derivations by numerically solving

the complete scaling equations, for a set of mapping coefficients that reproduces cloud and shadow curve data obtained in Monte Carlo simulations of a polydisperse Lennard-Jones fluid [114]. A summary, conclusions, and discussion of our results can be found in section 4.8. The appendices contain technical details of the calculations required to extract the various scaling laws and to establish the correspondence with the monodisperse limit, as well as information on how we fitted the complete scaling model to simulation data.

4.2 Complete scaling setup

In the critical region the thermodynamic behaviour of Ising-like systems is governed by two independent Ising-like scaling fields: a temperature variable (or thermal field) denoted by $\tilde{t}$ and a field variable (or ordering field) denoted by $\tilde{h}$. These two variables determine the singular part of an appropriate pressure-like variable (i.e. the Ising thermodynamic potential) $\tilde{p}$. We assume these three variables are defined such that they are zero at criticality. Asymptotically close to the critical point, $\tilde{p}$ becomes a generalised homogeneous function of $\tilde{t}$ and $\tilde{h}$ of the form

$$\tilde{p} = Q|\tilde{t}|^{2-\alpha} f^{\pm}\left(\frac{\tilde{h}}{|\tilde{t}|^{2-\alpha-\beta}}\right) \tag{4.3}$$

where Q is a positive amplitude, $f^{\pm}$ are two universal scaling functions that encode the properties of the three-dimensional Ising universality class, with the superscripts $\pm$ indicating $\tilde{t} \gtrless 0$.

In Ref. [107], Kim, Fisher, and Orkoulas (hereafter KFO) introduced the complete scaling approach, in the context of one-component fluids. In this formalism each of the Ising-model variables ($\tilde{p}$, $\tilde{t}$, and $\tilde{h}$) is expressed as a function of *all* thermodynamic fluid variables (pressure, temperature, and chemical potential), and this allows one to use Ising relations to work out the scaling behaviour of the fluid. (Formally this approach stems from a principle of isomorphism [110].) We now extend the approach to the case of a polydisperse fluid, similarly to Ref. [113]. To do so we proceed by writing second-order expansions around the critical point for the Ising scaling variables in terms of the fluid variables (now

pressure, temperature, and *species chemical potentials*) as

$$\tilde{p} = \check{p} - k_0 t - \boldsymbol{l}_0^{\mathrm{T}}\check{\boldsymbol{\mu}} - r_0 t^2 - \check{\boldsymbol{\mu}}^{\mathrm{T}}\boldsymbol{q}_0\check{\boldsymbol{\mu}} - t\boldsymbol{v}_0^{\mathrm{T}}\check{\boldsymbol{\mu}} - m_0\check{p}^2 - n_0\check{p}t - \check{p}\boldsymbol{n}_3^{\mathrm{T}}\check{\boldsymbol{\mu}} \tag{4.4}$$

$$\tilde{t} = t - \boldsymbol{l}_1^{\mathrm{T}}\check{\boldsymbol{\mu}} - j_1\check{p} - r_1 t^2 - \check{\boldsymbol{\mu}}^{\mathrm{T}}\boldsymbol{q}_1\check{\boldsymbol{\mu}} - t\boldsymbol{v}_1^{\mathrm{T}}\check{\boldsymbol{\mu}} - m_1\check{p}^2 - n_1\check{p}t - \check{p}\boldsymbol{n}_4^{\mathrm{T}}\check{\boldsymbol{\mu}} \tag{4.5}$$

$$\tilde{h} = \boldsymbol{l}_2^{\mathrm{T}}\check{\boldsymbol{\mu}} - k_2 t - j_2\check{p} - r_2 t^2 - \check{\boldsymbol{\mu}}^{\mathrm{T}}\boldsymbol{q}_2\check{\boldsymbol{\mu}} - t\boldsymbol{v}_2^{\mathrm{T}}\check{\boldsymbol{\mu}} - m_2\check{p}^2 - n_2\check{p}t - \check{p}\boldsymbol{n}_5^{\mathrm{T}}\check{\boldsymbol{\mu}} \tag{4.6}$$

where the entire set of coefficients $\boldsymbol{l}_i, k_i, j_i, r_i, \boldsymbol{q}_i, \boldsymbol{v}_i, m_i$, etc. appearing in Eqs. (4.4)–(4.6) are dubbed 'mixing coefficients' and

$$t \equiv \frac{T - T_{\mathrm{c}}}{T_{\mathrm{c}}}, \qquad \check{p} \equiv \frac{p - p_{\mathrm{c}}}{n_{\mathrm{c}} k_B T_{\mathrm{c}}} \tag{4.7}$$

Here n_{c} and T_{c}, the critical density and temperature (for a fixed parent composition or 'dilution line' [17]) are used to make all quantities dimensionless; the critical pressure is denoted by p_{c} and k_B is Boltzmann's constant. The vector $\check{\boldsymbol{\mu}}$ has as many components as there are species in the fluid, each of them being denoted by

$$\check{\mu}(\sigma) \equiv \frac{\mu(\sigma) - \mu_{\mathrm{c}}(\sigma)}{k_B T_{\mathrm{c}}} \tag{4.8}$$

where $\mu(\sigma)$ is the chemical potential of a species labelled by an arbitrary polydisperse attribute σ and $\mu_{\mathrm{c}}(\sigma)$ is its critical value. Because $\check{\boldsymbol{\mu}}$ is a vector, the quadratic expansions in Eqs. (4.4)–(4.6) require appropriate 'mixing coefficients' vectors and matrices when $\check{\boldsymbol{\mu}}$ appears (instead of the scalar constants in the other cases); all vectors are taken as column vectors and $\ldots^{\mathrm{T}}$ denotes the transpose of a vector. The vector $\boldsymbol{l}_2$ replaces a unit constant in KFO; leaving this unconstrained means no extra scaling of the argument of $f^{\pm}$ is needed. We use the notation k_2 instead of the k_1 in KFO to ensure that the subscript of each mixing coefficient in Eqs. (4.4)–(4.6) specifies uniquely to which of the Ising scaling variables $\tilde{p}, \tilde{t}$, and $\tilde{h}$ it belongs.

Denoting the arbitrary number of species in the fluid by M, we can check that the above construction gives the right number of equations for a proper equation of state: we have $M+2$ fluid thermodynamic variables ($\check{p}$, t, and $\check{\boldsymbol{\mu}}$), 3 Ising scaling variables ($\tilde{p}$, $\tilde{t}$, and $\tilde{h}$), and $3+1$ equations [Eqs. (4.3)–(4.6)]. Specifying $M+1$ thermodynamic variables (t and

$\check{\boldsymbol{\mu}}$) then determines all other variables and so in particular the pressure $\check{p}$.

At phase coexistence, t, $\check{\boldsymbol{\mu}}$ and $\check{p}$ are the same in both phases. Hence, from the above expansions [Eqs. (4.4)–(4.6)], so are $\tilde{t}$, $\tilde{h}$ and $\tilde{p}$. Thus the relation between these Ising scaling variables along the phase boundary can be worked out from the universal scaling function. Conventionally, one would parametrise this dependence by $\tilde{t}$ (< 0); then $\tilde{h}$, $\tilde{p}$, $\tilde{\rho}$, $\tilde{s}$ are, at least in principle, known functions of $\tilde{t}$, where the generalised number density, $\tilde{\rho}$, and entropy density, $\tilde{s}$, are the Ising scaling densities, defined by the relation $d\tilde{p} = \tilde{\rho}\, d\tilde{h} + \tilde{s} d\tilde{t}$. The results worked out by KFO (omitting prefactors and using the subscripts $\pm$ to label now the two phases) can be written as follows:

$$\tilde{p} \sim |\tilde{t}|^{2-\alpha} + \dots \tag{4.9}$$

$$\tilde{h} \sim |\tilde{t}|^{2-\alpha-\beta+\theta'} + \dots \tag{4.10}$$

$$\tilde{\rho}_{\pm} \sim \pm\left(|\tilde{t}|^{\beta} + |\tilde{t}|^{\beta+\theta} \pm |\tilde{t}|^{\beta+\theta'}\right) \tag{4.11}$$

$$\tilde{s}_{\pm} \sim |\tilde{t}|^{1-\alpha} + |\tilde{t}|^{1-\alpha+\theta} \pm |\tilde{t}|^{1-\alpha+\theta'}. \tag{4.12}$$

For the relevant Ising 3D case, KFO quote $\beta \simeq 0.326$, $\alpha \simeq 0.109$, $\theta \equiv \theta_4 \simeq 0.52$, $\theta' \equiv \theta_5 \simeq 1.32$; the latter two are exponents for the leading (even/odd) corrections to scaling. (KFO point out that in contrast to the symmetric case, $\tilde{h}$ does not vanish identically along the phase boundary.)

We will not keep track of terms of order higher than $|\tilde{t}|^1$. Therefore, we will neglect $\tilde{p}$ and $\tilde{h}$. In the scaling (4.11) for $\tilde{\rho}$, one in principle needs the leading correction to scaling (as $\beta + \theta < 1$), but one can avoid having to take this into account explicitly by parametrising everything in terms of $\tilde{\rho}_+ \equiv \tilde{\rho}$, which we assume to be positive. In particular, one has

$$\tilde{t} = -a\tilde{\rho}^{1/\beta} + \dots \tag{4.13}$$

with an appropriate constant a, and for the entropy density, by eliminating $\tilde{t}$ from the scalings (4.11) and (4.12),

$$\tilde{s} \sim \tilde{\rho}^{(1-\alpha)/\beta} + \tilde{\rho}^{(1-\alpha+\theta)/\beta} \tag{4.14}$$

The first exponent is $1/\tilde{\beta} \simeq 2.73$, the inverse of the 'Fisher-renormalised' order parameter

exponent $\tilde{\beta} = \beta/(1-\alpha)$, while the second one, from the corrections to scaling, is greater than $1/\beta \simeq 3.07$. Since we are only keeping terms to $\tilde{\rho}^{1/\beta}$ [see Eq. (4.13)], we need only to retain the first term in scaling (4.14) (as $1-\alpha+\theta > 1$). Thus one can write

$$\tilde{s} = -b\tilde{\rho}^{1/\tilde{\beta}} + \dots \tag{4.15}$$

where b is some constant.

As a technical aside, since we will frequently need to invert several series expansions with non-integer exponents, it is useful to recall that the inverse series of

$$y = \sum_{i=0}^{\infty} a_i x^{n_i} \tag{4.16}$$

(with increasing exponents $0 < n_0 < n_1 < \dots$) has the form

$$x = \left(\frac{y}{a_0}\right)^{1/n_0} \left(1 + \sum_{i\geq 1} b_i y^{n_i'} + \sum_{i,j\geq 1} b_{ij} y^{n_i'+n_j'} + \dots\right) \tag{4.17}$$

with $n_i' \equiv (n_i - n_0)/n_0$ and this is defined only when y and a_0 have the same sign, a restriction that we will mostly omit in similar results below. Applied to the scaling (4.11) this gives

$$\tilde{t} \sim \tilde{\rho}^{1/\beta}\left(1 + \tilde{\rho}^{\theta/\beta} + \tilde{\rho}^{\theta'/\beta} + \dots\right) \tag{4.18}$$

and hence the expansion (4.14). Note that in Eq. (4.15) the leading-order term $-b\tilde{\rho}^{1/\tilde{\beta}}$ that we are keeping is identical for the two coexisting phases, and hence we have dropped the $\pm$ subscript from $\tilde{s}$. Likewise, $\tilde{\rho}_- = -\tilde{\rho} + \mathcal{O}(\tilde{\rho}^{1+\theta'/\beta}) \approx -\tilde{\rho}$, to the order of our expansion (notice that $\beta + \theta' > 1$). Overall, we see that deviations from the Ising symmetry would only make themselves felt at higher orders.

We will need to know, for a given phase of the system, the density distribution vector $\check{\boldsymbol{\rho}}$. Its components are the normalised species densities $\check{\rho}(\sigma) \equiv \rho(\sigma)/n_c$. This vector of densities can be found by taking the $\check{\boldsymbol{\mu}}$-derivative of the pressure $\check{p}$; the analogous derivative with respect to temperature t is the entropy density $\check{s} = s/n_c$. The Ising scaling analogues of these quantities are $\tilde{s} = \partial\tilde{p}/\partial\tilde{t}$ and $\tilde{\rho} = \partial\tilde{p}/\partial\tilde{h}$, respectively. Since $d\tilde{p} = \tilde{s}\,d\tilde{t} + \tilde{\rho}\,d\tilde{h}$, one

can write, by analogy to the derivation in KFO,

$$d\tilde{p} = \tilde{s}\left(\frac{\partial\tilde{t}}{\partial\check{p}}d\check{p}+\frac{\partial\tilde{t}}{\partial t}dt+\frac{\partial\tilde{t}}{\partial\check{\boldsymbol{\mu}}}d\check{\boldsymbol{\mu}}\right)+\tilde{\rho}\left(\frac{\partial\tilde{h}}{\partial\check{p}}d\check{p}+\frac{\partial\tilde{h}}{\partial t}dt+\frac{\partial\tilde{h}}{\partial\check{\boldsymbol{\mu}}}d\check{\boldsymbol{\mu}}\right) \tag{4.19}$$

$$= \frac{\partial\tilde{p}}{\partial\check{p}}d\check{p}+\frac{\partial\tilde{p}}{\partial t}dt+\frac{\partial\tilde{p}}{\partial\check{\boldsymbol{\mu}}}d\check{\boldsymbol{\mu}}. \tag{4.20}$$

Inserting the Gibbs–Duhem equation $d\check{p} = \check{s}dt + \check{\boldsymbol{\rho}}^{\mathrm{T}}d\check{\boldsymbol{\mu}}$ (and imposing equality of the coefficients of $d\check{\boldsymbol{\mu}}$) gives

$$\check{\boldsymbol{\rho}} = \frac{-\frac{\partial\tilde{p}}{\partial\check{\boldsymbol{\mu}}}+\tilde{s}\frac{\partial\tilde{t}}{\partial\check{\boldsymbol{\mu}}}+\tilde{\rho}\frac{\partial\tilde{h}}{\partial\check{\boldsymbol{\mu}}}}{\frac{\partial\tilde{p}}{\partial\check{p}}-\tilde{s}\frac{\partial\tilde{t}}{\partial\check{p}}-\tilde{\rho}\frac{\partial\tilde{h}}{\partial\check{p}}}. \tag{4.21}$$

This is the mixture analogue of Eq. (5) in Ref. [113]. Inserting the above expansions [Eqs. (4.4)–(4.6)] into Eq. (4.21) and re-expanding (in terms of $\check{p}$, t, $\check{\boldsymbol{\mu}}$, $\tilde{\rho}$, and $\tilde{s}$) leads to

$$\begin{aligned}\check{\boldsymbol{\rho}}_{\pm} = {} & \boldsymbol{l}_0+(2m_0\boldsymbol{l}_0+\boldsymbol{n}_3)\check{p}+(n_0\boldsymbol{l}_0+\boldsymbol{v}_0)t+(\boldsymbol{l}_0\boldsymbol{n}_3^{\mathrm{T}}+2\boldsymbol{q}_0)\check{\boldsymbol{\mu}}+\mathscr{O}_2+\mathscr{O}_3 \\ & \pm\tilde{\rho}(\tilde{\boldsymbol{l}}_2+\mathscr{O}_1+\mathscr{O}_2)+\tilde{\rho}^2(-j_2\tilde{\boldsymbol{l}}_2+\mathscr{O}_1)\pm\tilde{\rho}^3 j_2^2\tilde{\boldsymbol{l}}_2+\tilde{s}(-j_1\boldsymbol{l}_0-\boldsymbol{l}_1)+\ldots\end{aligned} \tag{4.22}$$

where $\tilde{\boldsymbol{l}}_2 \equiv \boldsymbol{l}_2 - j_2\boldsymbol{l}_0$ and we have specialised to the two coexisting phases. In writing down Eq. (4.22) we have anticipated that $\check{p}$, t and $\check{\boldsymbol{\mu}}$ will be no larger than $\sim\tilde{\rho}$ and have thrown away contributions which as a result are smaller than $\tilde{\rho}^{1/\beta}$, e.g. terms $\sim\tilde{\rho}^4$, $\tilde{\rho}\tilde{s}$, $\tilde{s}^2$, and so on. The $\mathscr{O}_{1,2,3}$ symbols represent terms in $(\check{p},t,\check{\boldsymbol{\mu}})$ of the order indicated and will either not be crucial below or cannot be written down explicitly without including third or higher order terms in the mapping expansions Eqs. (4.4)–(4.6).

We notice by inspecting Eq. (4.22) that, if only the linear coefficients (j_i, k_i, and $\boldsymbol{l}_i$) are included, then $\check{\boldsymbol{\rho}}_{\pm}$ is a vectorial combination of $\boldsymbol{l}_0$, $\boldsymbol{l}_1$, and $\boldsymbol{l}_2$. Therefore for $M > 3$ it becomes impossible to realize a generic size distribution in the coexisting phases. Thus we conclude that in order to have fractionation properly accounted for one needs to include nonlinear mixing coefficients.

The critical scaling between the Ising variables has now been written down and we have expressed the density distribution vectors of the polydisperse fluid in terms of its thermodynamic variables and of the Ising scaling densities. It remains to add the particle conservation condition for each species, which we do in Section 4.3. Putting everything together one has a system of equations that can be solved either numerically or analytically

by expansion, allowing one to obtain the critical phase behaviour in terms of the physical fluid variables only.

4.3 Coexistence conditions

One of our goals is to obtain the critical scaling versions of cloud and shadow curves and, more generally, information on coexisting phases. The conditions of equal $\check{p}$, t and $\check{\boldsymbol{\mu}}$ will be satisfied if we are somewhere on the scaling phase boundary, as parametrised by $\tilde{\rho}$. In addition, we need to satisfy particle conservation, i.e. the 'dilution line' constraint. Let us write the parent density distribution as $\check{\boldsymbol{\rho}}^{(0)} = (1+\check{n})\boldsymbol{f}$, where the '(0)' superscript indicates the parent phase, $\boldsymbol{f}$ is the normalised parent density distribution vector and $\check{n} \equiv (n^{(0)} - n_\mathrm{c})/n_\mathrm{c}$ is the (normalised) deviation of the parent density from its critical value. We write the fractional phase volumes as $\frac{1}{2}(1 \pm \Delta)$ so that $\Delta = 0$ represents the situation where both phases occupy equal volumes. Then we need to satisfy

$$(1+\check{n})\boldsymbol{f} = \frac{1}{2}(1+\Delta)\check{\boldsymbol{\rho}}_+ + \frac{1}{2}(1-\Delta)\check{\boldsymbol{\rho}}_- \tag{4.23}$$

where $\check{\boldsymbol{\rho}}_+$ and $\check{\boldsymbol{\rho}}_-$ are given by Eq. (4.21) with $\tilde{\rho}_\pm = \pm\tilde{\rho}$ inserted. For our scaling expansions we use the expanded form (4.22) instead of Eq. (4.21), leading to

$$\begin{aligned}(1+\check{n})\boldsymbol{f} \quad = \quad & \frac{1}{2}(1+\Delta)[\boldsymbol{l}_0 + (2m_0\boldsymbol{l}_0 + \boldsymbol{n}_3)\check{p} + (n_0\boldsymbol{l}_0 + \boldsymbol{v}_0)t + (\boldsymbol{l}_0\boldsymbol{n}_3^\mathrm{T} + 2\boldsymbol{q}_0)\check{\boldsymbol{\mu}} + \mathscr{O}_2 + \mathscr{O}_3 \\ & + \tilde{\rho}(\tilde{\boldsymbol{l}}_2 + \mathscr{O}_1 + \mathscr{O}_2) + \tilde{\rho}^2(-j_2\tilde{\boldsymbol{l}}_2 + \mathscr{O}_1) + \tilde{\rho}^3 j_2^2\tilde{\boldsymbol{l}}_2 + \tilde{s}(-j_1\boldsymbol{l}_0 - \boldsymbol{l}_1)] \\ & + \frac{1}{2}(1-\Delta)[\boldsymbol{l}_0 + (2m_0\boldsymbol{l}_0 + \boldsymbol{n}_3)\check{p} + (n_0\boldsymbol{l}_0 + \boldsymbol{v}_0)t + (\boldsymbol{l}_0\boldsymbol{n}_3^\mathrm{T} + 2\boldsymbol{q}_0)\check{\boldsymbol{\mu}} + \mathscr{O}_2 + \mathscr{O}_3 \\ & - \tilde{\rho}(\tilde{\boldsymbol{l}}_2 + \mathscr{O}_1 + \mathscr{O}_2) + \tilde{\rho}^2(-j_2\tilde{\boldsymbol{l}}_2 + \mathscr{O}_1) - \tilde{\rho}^3 j_2^2\tilde{\boldsymbol{l}}_2 + \tilde{s}(-j_1\boldsymbol{l}_0 - \boldsymbol{l}_1)]. \end{aligned} \tag{4.24}$$

At the critical point, both density distributions must be equal to the parent one (as just above it we have only one phase). By setting all thermodynamic variables to zero in Eq. (4.24), one can see that $\boldsymbol{l}_0 = \boldsymbol{f}$; Eq. (4.24) can in turn be simplified to

$$\begin{aligned}\check{n}\boldsymbol{f} \quad = \quad & (2m_0\boldsymbol{f} + \boldsymbol{n}_3)\check{p} + (n_0\boldsymbol{f} + \boldsymbol{v}_0)t + (\boldsymbol{f}\boldsymbol{n}_3^\mathrm{T} + 2\boldsymbol{q}_0)\check{\boldsymbol{\mu}} + \tilde{\rho}^2(-j_2\tilde{\boldsymbol{l}}_2 + \mathscr{O}_1) + \mathscr{O}_2 + \mathscr{O}_3 \\ & + \tilde{s}(-j_1\boldsymbol{f} - \boldsymbol{l}_1) + \Delta\tilde{\rho}(\tilde{\boldsymbol{l}}_2 + \mathscr{O}_1 + \mathscr{O}_2) + \Delta\tilde{\rho}^3 j_2^2\tilde{\boldsymbol{l}}_2. \end{aligned} \tag{4.25}$$

We can now write down the set of equations that we need to solve, bearing in mind that $\tilde{p}$ and $\tilde{h}$ have been neglected to our order of expansion and noting explicitly the omitted third-order terms in the mapping expansions [Eqs. (4.4)–(4.6)]:

$$0 = \check{p} - k_0 t - \boldsymbol{f}^{\mathrm{T}}\check{\boldsymbol{\mu}} + \mathscr{O}_2 + \mathscr{O}_3 \tag{4.26}$$

$$\tilde{t} = t - \boldsymbol{l}_1^{\mathrm{T}}\check{\boldsymbol{\mu}} - j_1\check{p} + \mathscr{O}_2 + \mathscr{O}_3 \tag{4.27}$$

$$0 = \boldsymbol{l}_2^{\mathrm{T}}\check{\boldsymbol{\mu}} - k_2 t - j_2\check{p} + \mathscr{O}_2 + \mathscr{O}_3 \tag{4.28}$$

and

$$\begin{aligned} - \quad & \Delta\tilde{\rho}\tilde{\boldsymbol{l}}_2 + j_2\tilde{\boldsymbol{l}}_2\tilde{\rho}^2 - \Delta\tilde{\rho}^3\, j_2^2\tilde{\boldsymbol{l}}_2 + \tilde{s}(j_1\boldsymbol{f} + \boldsymbol{l}_1) = -\check{n}\boldsymbol{f} + (2m_0\boldsymbol{f} + \boldsymbol{n}_3)\check{p} \\ + \quad & (n_0\boldsymbol{f} + \boldsymbol{v}_0)t + (\boldsymbol{f}\boldsymbol{n}_3^{\mathrm{T}} + 2\boldsymbol{q}_0)\check{\boldsymbol{\mu}} + \mathscr{O}_2 + \mathscr{O}_3 + \Delta\tilde{\rho}(\mathscr{O}_1 + \mathscr{O}_2) + \tilde{\rho}^2\,\mathscr{O}_1. \end{aligned} \tag{4.29}$$

One sees that in this approach, fixed fractional volume lines appear naturally as they correspond to fixed Δ. These lines can then be traced out by considering a series of increasing $\tilde{\rho}$ (or corresponding $\tilde{t}$) and for each $\tilde{\rho}$ solving the above $M+3$ equations for the $M+3$ unknowns $(\check{n}, \check{p}, t, \check{\boldsymbol{\mu}})$. For the cloud curve one would fix $\Delta = 1$ for the high density branch and $\Delta = -1$ for the low-density branch (where the high density phase is the shadow phase and occupies a vanishing fraction of the system volume). These cases with constant Δ are considered in Section 4.4. For actual coexistence curves (see Section 4.6) one wants to fix the parent density $\check{n}$ instead and infer Δ. This can be done by treating $\Delta\tilde{\rho}$ as a small quantity to expand in, in addition to $\tilde{\rho}$; note that $\Delta\tilde{\rho}$ can be much smaller than $\tilde{\rho}$ but no larger since $|\Delta| \leq 1$. We then have to eliminate $\Delta\tilde{\rho}$ in the end by using the constraint of fixed $\check{n}$.

From the structure of the conditions above one sees that $\check{n}$, $\check{p}$, t and $\check{\boldsymbol{\mu}}$ will be smooth functions of the 'inputs' on the left-hand sides of Eqs. (4.26)–(4.29), i.e. $\Delta\tilde{\rho}$, $\tilde{\rho}^2$, $\tilde{s} = -b\tilde{\rho}^{1/\tilde{\beta}}$, and $\tilde{t} = -a\tilde{\rho}^{1/\beta}$; the input term $\Delta\tilde{\rho}^3$ is already covered here as the product of $\Delta\tilde{\rho}$ and $\tilde{\rho}^2$. The input variables appearing on the right-hand side in Eq. (4.29) have quantitative effects,

but do not produce new terms in the expansion. Thus we can write

$$\check{n} = \nu_1\Delta\tilde{\rho} + (\nu_2 + \nu_2'\Delta^2)\tilde{\rho}^2 + \nu_3\tilde{\rho}^{1/\tilde{\beta}} + (\nu_4\Delta + \nu_4'\Delta^3)\tilde{\rho}^3 + \nu_5\tilde{\rho}^{1/\beta} \tag{4.30}$$

$$\check{p} = \pi_1\Delta\tilde{\rho} + (\pi_2 + \pi_2'\Delta^2)\tilde{\rho}^2 + \pi_3\tilde{\rho}^{1/\tilde{\beta}} + (\pi_4\Delta + \pi_4'\Delta^3)\tilde{\rho}^3 + \pi_5\tilde{\rho}^{1/\beta} \tag{4.31}$$

$$t = \tau_1\Delta\tilde{\rho} + (\tau_2 + \tau_2'\Delta^2)\tilde{\rho}^2 + \tau_3\tilde{\rho}^{1/\tilde{\beta}} + (\tau_4\Delta + \tau_4'\Delta^3)\tilde{\rho}^3 + \tau_5\tilde{\rho}^{1/\beta} \tag{4.32}$$

$$\check{\boldsymbol{\mu}} = \boldsymbol{m}_1\Delta\tilde{\rho} + (\boldsymbol{m}_2 + \boldsymbol{m}_2'\Delta^2)\tilde{\rho}^2 + \boldsymbol{m}_3\tilde{\rho}^{1/\tilde{\beta}} + (\boldsymbol{m}_4\Delta + \boldsymbol{m}_4'\Delta^3)\tilde{\rho}^3 + \boldsymbol{m}_5\tilde{\rho}^{1/\beta} \tag{4.33}$$

where we have introduced appropriate coefficients $\nu_i, \nu_i', \pi_i, \pi_i', \tau_i, \tau_i', \boldsymbol{m}_i$, and $\boldsymbol{m}_i'$, with the latter two types representing vectors of coefficients with M components each. Notice that as throughout, we do not keep track of terms of order higher than $\tilde{\rho}^{1/\beta}$ here.

Pressure mixing coefficients are defined as the coefficients of the terms where the fluid pressure variable $\check{p}$ appears in the expansions for $\tilde{t}$ and $\tilde{h}$, i.e. Eqs. (4.5) and (4.6). (We exclude from this definition the coefficients in the expansion (4.4) for the pressure-like Ising variable $\tilde{p}$.) Without pressure mixing, where the $\tilde{\rho}^2$ and $\Delta\tilde{\rho}^3$ terms on the left-hand side of Eq. (4.29) are absent ($j_2 = 0$ in this case), one has an expansion in $\Delta\tilde{\rho}$, $\tilde{s}$ and $\tilde{t}$ only, so that $\nu_2, \pi_2, \tau_2, \boldsymbol{m}_2$ and $\nu_4, \pi_4, \tau_4, \boldsymbol{m}_4$ all vanish. One can check that the $\tilde{\rho}^2\,\mathscr{O}_1$ term on the right-hand side of Eq. (4.29) does not affect this conclusion.

By inserting Eqs. (4.30)–(4.33) into Eqs. (4.26)–(4.29), and comparing terms order by order, we obtain sets of equations that involve no thermodynamic variables, i.e. they contain only coefficients. These can be solved for the coefficients $\nu_i, \nu_i', \pi_i, \pi_i', \tau_i, \tau_i', \boldsymbol{m}_i$, and $\boldsymbol{m}_i'$, in terms of the 'mixing coefficients'. (See Appendix 4.A.)

4.3.1 Coexisting density distributions

As part of the output of the calculation one wants to look at the coexisting density distributions. Comparing Eq. (4.22) with Eq. (4.25) shows that

$$\check{\boldsymbol{\rho}}_\pm - \boldsymbol{f} = \check{n}\boldsymbol{f} + (\pm 1 - \Delta)[\tilde{\rho}(\tilde{\boldsymbol{l}}_2 + \mathscr{O}_1 + \mathscr{O}_2) + \tilde{\rho}^3 j_2^2 \tilde{\boldsymbol{l}}_2]. \tag{4.34}$$

Once we insert the expansions of $\check{p}, t, \check{\boldsymbol{\mu}}$ [Eqs. (4.31)–(4.33)] into the $\mathscr{O}_1$ and $\mathscr{O}_2$ terms we see that they contribute with terms scaling as $\Delta\tilde{\rho}, \tilde{\rho}^2$ (except if there is no pressure mixing)

and $\Delta^2\tilde{\rho}^2$, so that

$$\check{\boldsymbol{\rho}}_\pm - \boldsymbol{f} = \check{n}\boldsymbol{f} + (\pm 1 - \Delta)[\tilde{\rho}\tilde{\boldsymbol{l}}_2 + \boldsymbol{g}_2\Delta\tilde{\rho}^2 + \boldsymbol{g}_4\tilde{\rho}^3 + \boldsymbol{g}_4'\Delta^2\tilde{\rho}^3] \tag{4.35}$$

with some vectors $\boldsymbol{g}_2$, $\boldsymbol{g}_4$ and $\boldsymbol{g}_4'$; $\boldsymbol{g}_4$ vanishes without pressure mixing. Along with $\tilde{\boldsymbol{l}}_2$, these determine the directions in density distribution space along which fractionation takes place for the given parent composition $\boldsymbol{f}$; to linear and quadratic orders in $\tilde{\rho}$, there is one such direction each, and two to third order.

For the overall coexisting densities themselves one has, by taking the product with $\boldsymbol{e}^{\mathrm{T}}$ where $\boldsymbol{e}$ is a vector with all components equal to 1, the following expression:

$$\begin{aligned}
\check{n}_\pm &= \check{n} + (\pm 1 - \Delta)\left[\tilde{l}_2\tilde{\rho} + g_2\Delta\tilde{\rho}^2 + g_4\tilde{\rho}^3 + g_4'\Delta^2\tilde{\rho}^3\right] && (4.36)\\
&= \tilde{\rho}\left[\pm\tilde{l}_2 + \Delta(\nu_1 - \tilde{l}_2)\right] + \tilde{\rho}^2\left[\nu_2 \pm g_2\Delta + (\nu_2' - g_2)\Delta^2\right] \\
&\quad + \nu_3\tilde{\rho}^{1/\tilde{\beta}} + \tilde{\rho}^3\left[\pm g_4 + (\nu_4 - g_4)\Delta \pm g_4'\Delta^2 + (\nu_4' - g_4')\Delta^3\right] + \nu_5\tilde{\rho}^{1/\beta}. && (4.37)
\end{aligned}$$

Here we have abbreviated the element sums (not norms!) of the various vectors as $\tilde{l}_2 \equiv \boldsymbol{e}^{\mathrm{T}}\tilde{\boldsymbol{l}}_2$, $g_2 \equiv \boldsymbol{e}^{\mathrm{T}}\boldsymbol{g}_2$ etc. In the second step we have inserted Eq. (4.30). Note that one expects $\tilde{l}_2 > 0$ in order to ensure $\check{n}_+ > \check{n}_-$; also, for $\Delta = 1$ the (liquid cloud) parent density should increase with $\tilde{\rho}$, so that ν_1 should likewise come out positive.

4.4 Constant fractional volume lines

We can now look at the various curves in the phase diagram that are obtained for fixed Δ. With Δ fixed, there is only $\tilde{\rho}$ to eliminate as the curve parameter since $\Delta\tilde{\rho}$ is no longer treated as an additional small quantity to expand in. The elimination process involves inverting expansions like Eq. (4.30), which leads to

$$\begin{aligned}
\tilde{\rho} &= \frac{\check{n}}{\nu_1\Delta} - \frac{\nu_2 + \nu_2'\Delta^2}{\nu_1\Delta}\left(\frac{\check{n}}{\nu_1\Delta}\right)^2 - \frac{\nu_3}{\nu_1\Delta}\left(\frac{\check{n}}{\nu_1\Delta}\right)^{1/\tilde{\beta}} \\
&\quad + \left[2\left(\frac{\nu_2 + \nu_2'\Delta^2}{\nu_1\Delta}\right)^2 - \frac{\nu_4 + \nu_4'\Delta^2}{\nu_1\Delta}\right]\left(\frac{\check{n}}{\nu_1\Delta}\right)^3 - \frac{\nu_5}{\nu_1\Delta}\left(\frac{\check{n}}{\nu_1\Delta}\right)^{1/\beta}. && (4.38)
\end{aligned}$$

As pointed out after Eq. (4.16), our convention here and below is that expansions involving non-integer powers without modulus signs should be interpreted as applicable only when the quantity being raised is positive. Eq. (4.38) holds for $\Delta \neq 0$, while for $\Delta = 0$ one has similarly

$$\tilde{\rho} = \left(\frac{\check{n}}{\nu_2}\right)^{1/2} - \frac{\nu_3}{2\nu_2}\left(\frac{\check{n}}{\nu_2}\right)^{(1/\tilde{\beta}-1)/2} - \frac{\nu_5}{2\nu_2}\left(\frac{\check{n}}{\nu_2}\right)^{(1/\beta-1)/2}. \tag{4.39}$$

In both cases the expansions are given to the order that can be determined reliably from the original expansions up to $\tilde{\rho}^{1/\beta}$.

Inserting Eq. (4.38) into Eq. (4.32) yields for the temperature as a function of the parent density (when $\Delta \neq 0$):

$$\begin{aligned} t \;=\; & \frac{\tau_1}{\nu_1}\check{n} - \tilde{\tau}_2'\left(\frac{\check{n}}{\nu_1}\right)^2 - \tilde{\tau}_3\left(\frac{\check{n}}{\nu_1\Delta}\right)^{1/\tilde{\beta}} \\ & - \left[\tilde{\tau}_4\Delta + \tilde{\tau}_4'\Delta^3 - 2\left(\frac{\nu_2+\nu_2'\Delta^2}{\nu_1\Delta}\right)\tilde{\tau}_2'\Delta^2\right]\left(\frac{\check{n}}{\nu_1\Delta}\right)^3 - \tilde{\tau}_5\left(\frac{\check{n}}{\nu_1\Delta}\right)^{1/\beta} \end{aligned} \tag{4.40}$$

where

$$\tilde{\tau}_i \equiv \nu_i\frac{\tau_1}{\nu_1} - \tau_i, \qquad \tilde{\tau}_i' \equiv \nu_i'\frac{\tau_1}{\nu_1} - \tau_i' \tag{4.41}$$

Note that with this definition one has $\tilde{\tau}_2 = 0$, a fact we have already used above. (This result comes from a general proportionality between first and second order expansion coefficients, $\nu_2 = -j_2\nu_1$, $\tau_2 = -j_2\tau_1$, etc., which we derive in Appendix 4.A.) The coefficient structure makes sense: in the hypothetical degenerate case where the $\tilde{\rho}$-expansion coefficients for t [Eq. (4.32)] and $\check{n}$ [Eq. (4.30)] were all proportional to each other, then t and $\check{n}$ themselves would be proportional and therefore all terms must vanish (as is ensured by the definition of the $\tilde{\tau}_i$) except for $t = (\tau_1/\nu_1)\check{n}$.

As indicated, the linear term in Eq. (4.40) is *independent* of Δ; the only Δ-dependence arises via the higher order terms, and for the singular contributions it is a simple scaling. One sees that the expansion remains the same under the change $\Delta \to -\Delta$, so that such pairs of curves connect smoothly through the critical point. (As pointed out above, each curve for a given Δ is confined to one side of the critical point, such that $\check{n}/\nu_1$ and hence $\check{n}$ has the same sign as Δ, reflecting the constraint $\tilde{\rho} > 0$.) Note that without pressure mixing

also the quadratic and third order terms in Eq. (4.40) are Δ-independent because $\tilde{\tau}_4$ and ν_2 also vanish in this case, in addition to $\tilde{\tau}_2$.

The cloud curve is obtained for $\Delta = \pm 1$ as

$$\begin{aligned} t &= \frac{\tau_1}{\nu_1}\check{n} - \tilde{\tau}_2'\left(\frac{\check{n}}{\nu_1}\right)^2 - \tilde{\tau}_3\left|\frac{\check{n}}{\nu_1}\right|^{1/\tilde{\beta}} \\ &\quad - \left[\tilde{\tau}_4 + \tilde{\tau}_4' - 2\left(\frac{\nu_2+\nu_2'}{\nu_1}\right)\tilde{\tau}_2'\right]\left(\frac{\check{n}}{\nu_1}\right)^3 - \tilde{\tau}_5\left|\frac{\check{n}}{\nu_1}\right|^{1/\beta}. \end{aligned} \tag{4.42}$$

and this result now applies for $\check{n}$ of arbitrary sign, i.e. for parent densities either side of n_c. One can check that the structure of the above expansion of the cloud curve is independent of pressure mixing: even if all pressure mixing mapping coefficients are set to zero, then generically none of the prefactors in Eq.(4.42) will vanish. This is consistent with the result of Ref. [112], where the authors developed a framework for multi-component fluids with fixed overall composition but without pressure mixing, obtaining essentially the same cloud curve structure as in Eq. (4.42), except for the third order term. This may have been omitted by accident in Ref. [112] or dropped out because an intermediate expansion was truncated too early.

We note that in the case of mean-field ($\alpha = 0$, $\beta = \tilde{\beta} = 1/2$) rather than Ising criticality the second, third, and fifth terms in Eq. (4.42) degenerate into a term proportional to $\check{n}^2$, and consequently the cloud curve becomes fully smooth around the critical point, as expected. Otherwise, the term with the Fisher-renormalised exponent, $|\check{n}|^{1/\tilde{\beta}}$, is the first singular contribution. The latter may be challenging to detect in practice as it will be masked by the smooth variation given by the linear and the quadratic terms. One might then need to look at derivatives along the cloud curve, e.g. $d^3t/d\check{n}^3$ to see the singularity clearly as a divergence, or at least $d^2t/d\check{n}^2$ to observe a cusp singularity.

In the special case of $\Delta = 0$, one obtains the following generic form for the 50–50 fractional volume line ($\check{n}$ must now have the same sign as ν_2):

$$t = \frac{\tau_2}{\nu_2}\check{n} - \left(\nu_3\frac{\tau_2}{\nu_2} - \tau_3\right)\left(\frac{\check{n}}{\nu_2}\right)^{1/(2\tilde{\beta})} - \left(\nu_5\frac{\tau_2}{\nu_2} - \tau_5\right)\left(\frac{\check{n}}{\nu_2}\right)^{1/(2\beta)} \tag{4.43}$$

The slope τ_2/ν_2 of the linear piece in Eq. (4.43) is equal to the slope τ_1/ν_1 of the linear piece in the cloud [Eq. (4.42)] because $\nu_2 = -j_2\nu_1$ and $\tau_2 = -j_2\tau_1$ as mentioned above. Note

that one cannot interpolate smoothly to $\Delta = 0$ once $\tilde{\rho}$ has been eliminated: the $\Delta \to 0$ limit of Eq. (4.40) diverges. (It is important to note here that while all physical quantities vary smoothly with Δ *away* from the CP, this does not have to be the case in expansions around the CP.) The reason is that the expansion in Eq. (4.40) is, effectively, in terms of $\check{n}/(\nu_1\Delta)$ and so is valid in a range of width proportional to Δ that vanishes for $\Delta \to 0$. Note the rather unexpected singularity exponent above: the singularity for $\Delta = 0$ is *stronger* than on the constant fractional volume lines $\Delta \neq 0$, including the cloud curve.

The $\Delta = 0$ constant fractional volume line is special also in that its shape depends sensitively on the presence or absence of pressure mixing. In the latter case one has $\check{n} = \nu_3\tilde{\rho}^{1/\tilde{\beta}} + \nu_5\tilde{\rho}^{1/\beta}$, which yields $\tilde{\rho}^{1/\tilde{\beta}} \sim \check{n}(1 + \check{n}^{\tilde{\beta}/\beta-1} + \ldots)$ and hence (for $\check{n}/\nu_3 > 0$)

$$t = \frac{\tau_3}{\nu_3}\check{n} - \left(\nu_5\frac{\tau_3}{\nu_3} - \tau_5\right)\left(\frac{\check{n}}{\nu_3}\right)^{1/(1-\alpha)} \tag{4.44}$$

In this form where $\tilde{\rho}$ has been eliminated the fact that pressure mixing changes the leading singularity exponent from $1/(1-\alpha)$ to $(1-\alpha)/(2\beta)$ may seem a little unexpected; however, it is quite natural when looked at in terms of the vanishing of a number of contributions in the $\tilde{\rho}$-expansions [Eqs. (4.30) and (4.32)]. Note that the slope of the linear term in Eq. (4.44) is generically *different* from the slope of the cloud curve at the critical point: without pressure mixing the 50–50 fractional volume line departs from the critical point in a different direction, while in the presence of pressure mixing it starts off tangentially to the cloud curve.

To highlight the differences discussed above we now consider $\delta t_0 \equiv t_{\text{cloud}} - t_{\Delta=0} > 0$, which is the temperature difference between the cloud curve and the $\Delta = 0$ line at fixed parent density $\check{n}$. With pressure mixing this is the difference between Eq. (4.42) and Eq. (4.43), which gives

$$\delta t_0 = \left(\nu_3\frac{\tau_2}{\nu_2} - \tau_3\right)\left(\frac{\check{n}}{\nu_2}\right)^{1/(2\tilde{\beta})} + \left(\nu_5\frac{\tau_2}{\nu_2} - \tau_5\right)\left(\frac{\check{n}}{\nu_2}\right)^{1/(2\beta)} + \ldots \tag{4.45}$$

whereas in the case without pressure mixing it is the difference between Eq. (4.42) (with modified prefactors due to pressure mixing being absent) and Eq. (4.44), i.e.

$$\delta t_0 = \left(\frac{\tau_1}{\nu_1} - \frac{\tau_3}{\nu_3}\right)\check{n} + \left(\nu_5\frac{\tau_3}{\nu_3} - \tau_5\right)\left(\frac{\check{n}}{\nu_3}\right)^{1/(1-\alpha)} \tag{4.46}$$

With pressure mixing [Eq. (4.45)] there is *no linear contribution*, reflecting the fact that the 50–50 fractional volume line starts off tangential to the cloud curve, with the slopes of the linear pieces in Eqs. (4.42) and (4.43) cancelling. Without pressure mixing this is no longer the case, leading to the linear piece in Eq. (4.46). This suggests that measurements of δt_0 as a function of $\check{n}$ could be useful probes of pressure mixing effects, in particular because the leading terms have exponents of $1/(2\tilde{\beta}) \simeq 1.37$ and 1 respectively that are easy to distinguish. This is explored further in our numerical analysis in Section 4.7.

Looking next at the behaviour of the coexisting densities, these are easy to determine since Eq. (4.37) has, for constant Δ, the same structure as the expansion of the parent density, Eq. (4.30). Therefore one can read off directly the expression for t vs. $\check{n}_\pm$, but as this is rather long we defer it to Appendix 4.B. One useful special case is t vs. $\check{n}_\pm$ for $\Delta = \mp 1$, which gives the shadow curve. As can be seen in Appendix 4.B, it has the same structure as the cloud curve [Eq. (4.42)], but with different coefficients (obtained via $\nu_1 \to \nu_1 - 2\tilde{l}_2$, $\nu_2 \to \nu_2 - g_2$, $\nu_2' \to \nu_2' - g_2$, $\nu_4 \to \nu_4 - g_4$, $\nu_4' \to \nu_4' - g_4'$).

For the other interesting special case of $\Delta = 0$ one obtains the '50–50 coexistence curves', i.e. the temperature dependence of the coexisting densities obtained from parents on the 50–50 fractional volume line:

$$t = \tau_2\left(\frac{\check{n}_\pm}{\tilde{l}_2}\right)^2 + \tau_3\left|\frac{\check{n}_\pm}{\tilde{l}_2}\right|^{1/\tilde{\beta}} + 2\frac{\nu_2\tau_2}{\tilde{l}_2}\left(\frac{\check{n}_\pm}{\tilde{l}_2}\right)^3 + \tau_5\left|\frac{\check{n}_\pm}{\tilde{l}_2}\right|^{1/\beta}. \tag{4.47}$$

The two curves $t(\check{n}_+)$ and $t(\check{n}_-)$ are symmetric in the first two leading terms, but then the asymmetry appears. Without pressure mixing one has $\tau_2 = 0$ and so the leading quadratic as well as the cubic terms are both absent.

It is useful to convert the above results into expressions of densities versus temperature to connect with our discussion of the diameter in the introduction. The $\Delta = 0$ line is the

equal volume diameter and, by inverting (4.43) and (4.44), respectively, is given by

$$\check{n} = \frac{\nu_2}{\tau_2} t + \left(\nu_3 - \tau_3 \frac{\nu_2}{\tau_2}\right) \left(\frac{t}{\tau_2}\right)^{1/(2\tilde{\beta})} + \left(\nu_5 - \tau_5 \frac{\nu_2}{\tau_2}\right) \left(\frac{t}{\tau_2}\right)^{1/(2\beta)} . \tag{4.48}$$

with pressure mixing and by

$$\check{n} = \frac{\nu_3}{\tau_3} t - \left(\tau_5 \frac{\nu_3}{\tau_3} - \nu_5\right) \left(\frac{t}{\tau_3}\right)^{1/(1-\alpha)} \tag{4.49}$$

without. Note that in both cases the leading term is linear, in contrast to the situation in the monodisperse case discussed in the introduction, and it is only the exponent of the first subleading term that signals the presence or absence of pressure mixing.

Generally, if we consider Δ being varied from 1 to -1, the curve $t(\check{n})$ will be deformed from the high-density to the low-density part of the cloud curve (see Fig. 4.1); similarly $t(\check{n}_+)$ interpolates between the high-density parts of the cloud curve and of the shadow curve, while $t(\check{n}_-)$ interpolates between the low-density parts of the shadow curve and of the cloud curve.

4.5 The monodisperse case

We have seen above that the complete scaling predictions for the equal volume diameter are different from those reviewed in the introduction for monodisperse systems, whether with or without pressure mixing. Ostensibly, however, our analysis is valid for an arbitrary number of mixture components M. What, then, is different about the monodisperse case ($M = 1$)?

One answer is that when there is only a single chemical potential, the conditions in Eqs. (4.26)–(4.28) are sufficient to determine $\tilde{p}$, t, μ and these must therefore be smooth functions of $\tilde{t} = -a\tilde{\rho}^{1/\beta}$. (A similar comment can be found in Ref. [113].) In our $\tilde{\rho}$-expansions, Eqs. (4.31)–(4.33), this means that the only nonzero coefficients are π_5, τ_5, and $\boldsymbol{m}_5$, the latter being a scalar for $M = 1$. (One can easily check this from the explicit conditions for the coefficients; e.g. the first order conditions in Eqs. (4.64)–(4.67) have the obvious solution $\pi_1 = \tau_1 = m_1 = 0$, $\nu_1 = \tilde{l}_2$ in the monodisperse case.) Since $\tilde{\rho} \sim |\tilde{t}|^\beta \sim |t|^\beta$,

the coexisting densities then have the standard expansion $\check{n}_\pm \sim \pm\tilde{\rho} + \tilde{\rho}^2 + \tilde{\rho}^{1/\tilde{\beta}} + \tilde{\rho}^{1/\beta} \sim \pm|t|^\beta + |t|^{2\beta} + |t|^{1-\alpha} + |t|$ and the first term cancels from the diameter.

In the polydisperse case the solution above does not work since e.g. in the first order conditions in Eqs. (4.64)–(4.67) the vectors $\boldsymbol{f}$ and $\tilde{\boldsymbol{l}}_2$ will generically not be parallel. Alternatively, one can go back to the dilution line constraint in Eq. (4.25): there are singular (in $\tilde{t}$) terms on the right-hand side, proportional to $\tilde{\rho}$, $\tilde{\rho}^2$ and $\tilde{s}$. If $\check{\boldsymbol{\mu}}$ and t depended smoothly on $\tilde{t}$, these singular terms would always dominate and so push the system off the required dilution line. To avoid this, $\check{\boldsymbol{\mu}}$ and t themselves need to contain terms proportional to $\tilde{\rho}$, $\tilde{\rho}^2$ and $\tilde{s}$. In the monodisperse case there is no dilution line constraint and so no such requirement.

One might argue that the above discussion cannot be taken literally for most colloidal systems, because of the difficulty of producing the truly identical particles that a description in terms of a single species ($M = 1$) in principle requires. A more realistic endeavour would be to make the distribution of particle sizes (say) narrower and narrower by improving experimental protocols. In the limit, one would then still expect to retrieve monodisperse phase behaviour, but this would result from an M-species system where the differences between species have become very small. How is this second route to the monodisperse limit achieved in our approach?

Taking the true monodisperse limit where one has M species of particles that are physically identical, one can think of the different species as being identified by different colours but with this colour having no effect on the physical behaviour. We show in Appendix 4.C that in this description of a physically monodisperse – but 'colour polydisperse' – system, the vectors $\boldsymbol{f}$ and $\tilde{\boldsymbol{l}}_2$ will always be parallel. As discussed above, there is then no need for the additional scaling terms that are required in a physically polydisperse system, and standard monodisperse scaling behaviour follows. (We note as an aside that similar conceptual issues, related to the physical relevance of polydispersity in the limit when particle species become very similar, arise in determining the configurational entropy of glasses, see e.g. Ref. [115].)

The derivation in Appendix 4.C is effectively a method by which one can map *the mixing coefficients* of a monodisperse fluid onto a new set of mixing coefficients for a colour

polydisperse fluid with nominally $M > 1$ components, in such a way that both systems are physically equivalent with regards to their critical behaviour. The method is in fact more general, allowing one to map the mixing coefficients of a fluid with M' components onto a physically identical fluid with nominally $M > M'$ components.

4.6 Coexistence curves

Next we look at conventional coexistence curves, which are obtained from a parent of fixed density $\check{n}$ by varying temperature. With $\check{n}$ fixed, Δ then has to vary appropriately to maintain particle conservation.

We start by separating $\Delta\tilde{\rho}$-terms and $\tilde{\rho}$-terms in Eq. (4.30) for $\check{n}$:

$$\check{n} - \nu_2\tilde{\rho}^2 - \nu_3\tilde{\rho}^{1/\tilde{\beta}} - \nu_5\tilde{\rho}^{1/\beta} = \nu_1\Delta\tilde{\rho} + \nu_2'(\Delta\tilde{\rho})^2 + \nu_4(\Delta\tilde{\rho})\tilde{\rho}^2 + \nu_4'(\Delta\tilde{\rho})^3 \tag{4.50}$$

This can be solved perturbatively for $\Delta\tilde{\rho}$:

$$\begin{aligned}\Delta\tilde{\rho} \;=\; & \frac{\check{n}}{\nu_1} - \frac{\nu_2}{\nu_1}\tilde{\rho}^2 - \frac{\nu_2'}{\nu_1}\left(\frac{\check{n}}{\nu_1}\right)^2 - \frac{\nu_3}{\nu_1}\tilde{\rho}^{1/\tilde{\beta}} - \left(\frac{\nu_4}{\nu_1} - 2\frac{\nu_2}{\nu_1}\frac{\nu_2'}{\nu_1}\right)\tilde{\rho}^2\frac{\check{n}}{\nu_1} \\ & - \left[\frac{\nu_4'}{\nu_1} - 2\left(\frac{\nu_2'}{\nu_1}\right)^2\right]\left(\frac{\check{n}}{\nu_1}\right)^3 - \frac{\nu_5}{\nu_1}\tilde{\rho}^{1/\beta}\end{aligned} \tag{4.51}$$

We have used that since $\check{n} = \nu_1\Delta\tilde{\rho}$ to leading order, $\check{n}$ is never larger than $\sim\tilde{\rho}$, so that we are sure to have all relevant terms if we treat $\check{n}$ as proportional to $\tilde{\rho}$ and then expand. Now one inserts (4.51) into the expansion for t in Eq. (4.32):

$$t = \frac{\tau_1}{\nu_1}\check{n} - \tilde{\tau}_2'\left(\frac{\check{n}}{\nu_1}\right)^2 - \tilde{\tau}_3\tilde{\rho}^{1/\tilde{\beta}} - \left(\tilde{\tau}_4 - 2\frac{\nu_2}{\nu_1}\tilde{\tau}_2'\right)\frac{\check{n}}{\nu_1}\tilde{\rho}^2 - \tilde{\tau}_4'\left(\frac{\check{n}}{\nu_1}\right)^3 - \tilde{\tau}_5\tilde{\rho}^{1/\beta} \tag{4.52}$$

The leading linear and quadratic terms can be cancelled by switching from t to the temperature difference from the cloud point temperature, $\delta t \equiv t_{\text{cloud}} - t$. Here t_{cloud} is given by Eq. (4.42) and is fixed by the given parent density $\check{n}$. In terms of δt, Eq. (4.52) takes the

simpler form

$$\begin{aligned}\delta t &= \tilde{\tau}_3\left[\tilde{\rho}^{1/\tilde{\beta}} - \left|\frac{\check{n}}{\nu_1}\right|^{1/\tilde{\beta}}\right] + \left(\tilde{\tau}_4 - 2\frac{\nu_2}{\nu_1}\tilde{\tau}_2'\right)\frac{\check{n}}{\nu_1}\left[\tilde{\rho}^2 - \left(\frac{\check{n}}{\nu_1}\right)^2\right] \\ &\quad + \tilde{\tau}_5\left[\tilde{\rho}^{1/\beta} - \left|\frac{\check{n}}{\nu_1}\right|^{1/\beta}\right]. \end{aligned} \tag{4.53}$$

(Note that δt is positive by definition and so needs to increase with $\tilde{\rho}$; thus $\tilde{\tau}_3$ should be positive.)

Our goal is to find the coexisting densities $\check{n}_\pm$. For these one uses Eq. (4.36) with Eq. (4.51) inserted, to obtain $\check{n}_\pm$ as a function of $\tilde{\rho}$ for fixed $\check{n}$. Now $\tilde{\rho}$ needs to be eliminated between the resulting expression [see (4.84) in Appendix 4.B] and Eq. (4.53). As $\tilde{\rho}$ only appears at second and higher order in Eq. (4.53), it suffices to find it from (4.84) to linear order in terms of $\check{n}_\pm$, resulting in the simple expression

$$\tilde{\rho} = \pm\left(\frac{\check{n}_\pm}{\tilde{l}_2} + c\check{n}\right) \tag{4.54}$$

where $c \equiv 1/\nu_1 - 1/\tilde{l}_2$. Inserting into Eq. (4.53) produces finally

$$\begin{aligned}\delta t &= \tilde{\tau}_3\left(\left|\frac{\check{n}_\pm}{\tilde{l}_2} + c\check{n}\right|^{1/\tilde{\beta}} - \left|\frac{\check{n}}{\nu_1}\right|^{1/\tilde{\beta}}\right) + \left(\tilde{\tau}_4 - 2\frac{\nu_2}{\nu_1}\tilde{\tau}_2'\right)\frac{\check{n}}{\nu_1}\left[\left(\frac{\check{n}_\pm}{\tilde{l}_2} + c\check{n}\right)^2 - \left(\frac{\check{n}}{\nu_1}\right)^2\right] \\ &\quad + \tilde{\tau}_5\left(\left|\frac{\check{n}_\pm}{\tilde{l}_2} + c\check{n}\right|^{1/\beta} - \left|\frac{\check{n}}{\nu_1}\right|^{1/\beta}\right). \end{aligned} \tag{4.55}$$

One sees that at the onset of phase coexistence ($\delta t = 0$), $\check{n}_\pm/\tilde{l}_2 + c\check{n}$ must equal $\check{n}/\nu_1$ or $-\check{n}/\nu_1$ to leading order. This gives $\check{n}_+ = \check{n}$ and $\check{n}_- = \check{n}(1 - 2\tilde{l}_2/\nu_1)$ or vice versa; the latter prefactor is consistent with the ratio of the slopes of cloud and shadow curves at the critical point, which can be read off from Eqs. (4.42) and (4.82).

The above expressions simplify considerably for the case $\check{n} = 0$. Eq. (4.55) then gives the critical coexistence curve as

$$|t| = \delta t = \tilde{\tau}_3\left|\frac{\check{n}_\pm}{\tilde{l}_2}\right|^{1/\tilde{\beta}} + \tilde{\tau}_5\left|\frac{\check{n}_\pm}{\tilde{l}_2}\right|^{1/\beta} \tag{4.56}$$

The leading term shows the expected Fisher-renormalised order parameter exponent $\tilde{\beta}$.

More interestingly, the structure of this conventional coexistence curve has no obvious signatures of pressure mixing, a situation rather different from the 50–50 ($\Delta = 0$) coexistence curve in Eq. (4.47).

We next consider the temperature variation of the fractional volumes of the coexisting phases, more specifically their difference Δ. In Eqs. (4.51) and (4.53) we already have $\Delta\tilde{\rho}$ and δt, both as functions of $\tilde{\rho}$ (for fixed $\check{n}$). Solving the second of these equations for $\tilde{\rho}$ gives to leading order

$$\tilde{\rho}^{1/\tilde{\beta}} = \frac{\delta t}{\tilde{\tau}_3} + \left|\frac{\check{n}}{\nu_1}\right|^{1/\tilde{\beta}} \tag{4.57}$$

If we then keep only the leading terms in $\Delta\tilde{\rho}$ and $\tilde{\rho}$ and write the ratio between them we find

$$\Delta = \frac{\check{n} - \nu_2(\delta t/\tilde{\tau}_3)^{2\tilde{\beta}}}{\nu_1\left[\delta t/\tilde{\tau}_3 + |\check{n}/\nu_1|^{1/\tilde{\beta}}\right]^{\tilde{\beta}}} \tag{4.58}$$

For off-critical parents ($\check{n} \neq 0$) this starts off at ± 1 as it should at the cloud point and then decreases (in modulus), scaling for $\check{n}^{1/\tilde{\beta}} \ll \delta t \ll \check{n}^{1/(2\tilde{\beta})}$ as $\check{n}(\delta t)^{-\tilde{\beta}}$. The behaviour changes when $\delta t \sim \check{n}^{1/(2\tilde{\beta})}$ and crosses over to $\Delta \approx -(\nu_2/\nu_1)(\delta t/\tilde{\tau}_3)^{\tilde{\beta}}$ for $\delta t \gg \check{n}^{1/(2\tilde{\beta})}$. Only the latter regime is present for the critical coexistence curve ($\check{n} = 0$). For $\check{n} \neq 0$, the crossover between the different regimes implies that on one side of the critical point Δ will always depend non-monotonically on δt. (To find which side will have that behaviour we have to look at the sign of $-(\nu_2/\nu_1)$: if this is positive, Δ is increasing for large δt and so the non-monotonicity occurs on the high-density side of the critical point, where Δ initially *decreases* from 1.)

Without pressure mixing, where ν_2 vanishes, the corresponding expression is

$$\Delta = \frac{\check{n} - \nu_3(\delta t/\tilde{\tau}_3)}{\nu_1\left[\delta t/\tilde{\tau}_3 + |\check{n}/\nu_1|^{1/\tilde{\beta}}\right]^{\tilde{\beta}}} \tag{4.59}$$

which scales as $\check{n}(\delta t)^{-\tilde{\beta}}$ for $\check{n}^{1/\tilde{\beta}} \ll \delta t \ll \check{n}$, changing when $\delta t \sim |\check{n}|^{1/\tilde{\beta}}$ and crossing over to $(\delta t)^{1-\beta}$ for $\delta t \gg \check{n}$; similar comments about non-monotonicity apply as above, but now one has to look at the sign of $-(\nu_3/\nu_1)$.

Finally we ask about the behaviour of the midpoint diameter of the coexistence curves,

as well as about its analogue at off-critical parent densities. For any fixed $\check{n}$, we define $\bar{n} \equiv \frac{1}{2}(\check{n}_+ + \check{n}_-)$ as in the introduction. The steps sketched in Appendix 4.B lead to

$$\bar{n} = \frac{\nu_2 \tilde{l}_2}{\nu_1} \left(\frac{\delta t}{\tilde{\tau}_3}\right)^{2\tilde{\beta}} - 2\tilde{\beta} \frac{\nu_2 \tilde{l}_2}{\nu_1} \frac{\tilde{\tau}_5}{\tilde{\tau}_3} \left(\frac{\delta t}{\tilde{\tau}_3}\right)^{2\tilde{\beta}+\alpha/(1-\alpha)} \tag{4.60}$$

In the case without pressure mixing, we have

$$\bar{n} = \frac{\tilde{l}_2 \nu_3}{\tilde{\tau}_3 \nu_1} \delta t + \frac{\tilde{l}_2}{\nu_1} \left(\nu_5 - \nu_3 \frac{\tilde{\tau}_5}{\tilde{\tau}_3}\right) \left(\frac{\delta t}{\tilde{\tau}_3}\right)^{1/(1-\alpha)} \tag{4.61}$$

Compared to the results quoted in the introduction, one sees that the leading exponents are Fisher-renormalised because of the presence of polydispersity, giving $2\beta/(1-\alpha) = 2\tilde{\beta}$ with pressure mixing and $(1-\alpha)/(1-\alpha) = 1$ without.

A comparison with the equal volume diameter results is also instructive: Eq. (4.49) shows that without pressure mixing both diameters have the same scaling behaviour but with different prefactors. With pressure mixing, only the midpoint diameter has a leading singular term, while the equal volume diameter starts off linearly as shown by Eq. (4.44). It is worth emphasizing also that the midpoint diameter, which is obtained by cooling a parent with the critical density, always relates to temperatures below the critical point, $t < 0$. The equal volume diameter has no such restriction – it only has to lie within the coexistence region, i.e. below the cloud curve – as we will see in the numerical illustrations in Sec. 4.7.

Above we have written the midpoint diameter density as a function of temperature, to ease comparison with treatments elsewhere in the literature. For consistency with the way we have expressed our results for other phase diagram loci we give the corresponding inverted relations here, which read

$$\delta t = \tilde{\tau}_3 \left(\frac{\nu_1 \bar{n}}{\nu_2 \tilde{l}_2}\right)^{1/(2\tilde{\beta})} + \tilde{\tau}_5 \left(\frac{\nu_1 \bar{n}}{\nu_2 \tilde{l}_2}\right)^{1/(2\beta)} \tag{4.62}$$

with pressure mixing and

$$\delta t = \tilde{\tau}_3 \left(\frac{\nu_1 \bar{n}}{\nu_3 \tilde{l}_2}\right) + \left(\tilde{\tau}_5 - \tilde{\tau}_3 \frac{\nu_5}{\nu_3}\right) \left(\frac{\nu_1 \bar{n}}{\nu_3 \tilde{l}_2}\right)^{1/(1-\alpha)} \tag{4.63}$$

in the case without. As written, the results in Eqs. (4.60), (4.61), (4.62), and (4.63) are valid only for $\check{n} = 0$, but their off-critical versions can be obtained simply via the replacement $\bar{n} \to \bar{n} - \check{n}\left(1 - \frac{\tilde{l}_2}{v_1}\right)$.

4.7 Numerics

In this section we compare the scaling expansions derived above to direct numerical evaluation of the complete scaling theory. For a given set of numerical values for the mixing coefficients one needs to solve the mapping equations (4.4)–(4.6) and the dilution line (or particle conservation) constraint (4.23). The relation between the Ising variables is given by the scaling relation (4.3) together with the coexistence-region condition $\tilde{h} = 0$. In solving this full system we will not make any further approximations; in particular we will retain $\tilde{p}$ rather than neglecting it as subleading, and we will use the general expressions for $\check{\boldsymbol{\rho}}$ from Eq. (4.21) without further expansion. (By setting $\tilde{h} = 0$ we are neglecting the asymmetry terms from Eq. (4.10); these are subleading even compared to the effect of allowing $\tilde{p}$ to be nonzero.) For the required explicit form of the scaling relation (4.3) we have used the 'parametric linear model' of Ref. [116].

While in the analytical development of the previous sections it was convenient to use $\tilde{\boldsymbol{\rho}}$ to parameterise the various curves in the phase diagram, for the numerics we prefer $\tilde{t}$ as this enters directly in the scaling form (4.3). One ends up with a system of $M+3$ equations (mapping equations plus dilution line constraint) and $M+4$ variables, the extra variable in addition to the $M+3$ variables $\check{n}, \check{p}, t$, and $\tilde{\boldsymbol{\mu}}$ being precisely $\tilde{t}$. For each value of this variable we solve the full system of equations to generate a point in the space of the physical fluid variables. With this approach we can check both the exponents *and prefactors* of the analytical expansions obtained above. In particular we will discuss the effects of pressure mixing. We will see that these generally become weaker as one moves away from the critical point, leading to crossovers to behaviour characteristic of a system without pressure mixing.

We started by finding fitted values for the mixing coefficients by comparison with cloud and shadow data obtained in Ref. [114] from computer simulations of a Lennard-Jones (LJ) fluid with 'amplitude' polydispersity. The results as well as the details of the fitting

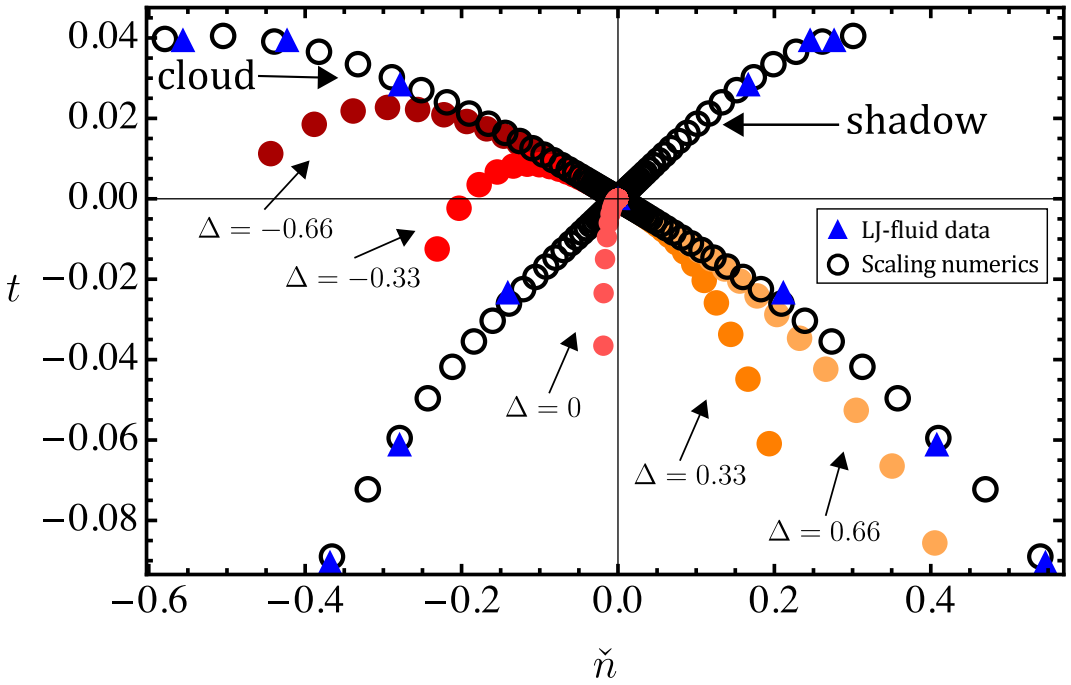

FIGURE 4.1: Cloud and shadow data from polydisperse Lennard-Jones (LJ) fluid simulations in Ref. [114] (triangles) and from our numerical solution (empty circles). From warmer to cooler colours, we also show data for five constant fractional volume lines, for values of Δ as shown. (In the convention used in later figures, the strength of pressure mixing here is $f_{\rm pm} = 1$.)

method are described in Appendix 4.D. With these fitted mixing coefficients the numerical solution led to the cloud and shadow data in Fig. 4.1; notice the good agreement with the LJ fluid data. We omitted in the fit and in the comparison in Fig. 4.1 those data points from Ref. [114] that were too far from the CP to allow a meaningful comparison with a scaling theory for the critical behaviour. From warmer to cooler colours, we also show data for the numerically calculated constant fractional volume lines (t vs. $\check{n}$) for $\Delta = -0.66$, -0.33, 0, 0.33 and 0.66, respectively. Notice that the $\Delta = 0$ curve, which is the equal volume diameter, initially moves left and up from the CP, towards higher temperatures and lower densities. It shares this behaviour with the constant fractional volume lines for negative Δ as discussed in detail below.

For further numerical evaluation it is useful to be able to vary the strength of pressure mixing. We do this by scaling the values of the pressure mixing coefficients according to $j_1 \to f_{\rm pm}\, j_1$ and $j_2 \to f_{\rm pm}\, j_2$, where the factor $f_{\rm pm}$ is then a 'pressure mixing fraction'. (With this definition, $f_{\rm pm} = 1$ in Fig. 4.1.) Changing $f_{\rm pm}$ in the range 0 to 4 we obtain data that are physically reasonable and only slightly off the LJ data from Ref. [114]. But

predictions change close to the critical point, as we will explore shortly.

We have selected a number of key features of the scaling formulae obtained above for which we will present supporting numerical data. Firstly, Figs. 4.2 and 4.3 illustrates how the behaviour of the constant fractional volume lines (t vs. $\check{n}$ for fixed $\Delta = 0, \pm 0.1$) depends on pressure mixing. For strong pressure mixing (Fig. 4.2) we can clearly see that, although the curve for $\Delta = 0$ separates from the one with $\Delta = -0.1$ as it moves away from the CP (main graph), the two curves become tangential to each other at the CP, i.e. they have the same slope there (inset). This agrees with the prediction for the prefactors of the leading linear terms in Eqs. (4.40) and (4.43). The curve with $\Delta = 0.1$ has the same initial slope but departs from the CP in the opposite direction, towards lower temperatures and larger parent densities. Two additional lines in Fig. 4.2 show numerical results for small $|\Delta|$. These clarify that, as noted before, all properties are smooth in Δ *away* from the CP, but cross over to the discontinuous change at $\Delta = 0$ in the direction of departure from the CP itself.

Fig. 4.3 contrasts these observations with the case without pressure mixing, obtained by setting $f_{\text{pm}} = 0$. The curves for $\Delta = \pm 0.1$ again show the same slope at the CP and depart in opposite directions. However, the $\Delta = 0$ line now has a different slope at the CP and separates linearly from the other lines, consistent with the different prefactors of the linear terms in Eqs. (4.43) and (4.44) and the discussion in Sec. 4.4 above. Two further small $|\Delta|$ lines again illustrate how these discontinuous changes at the CP connect to the smooth Δ-dependences away from the CP.

Figs. 4.4, 4.5 and 4.6 illustrate the nonlinear terms in the equal volume diameter ($\Delta = 0$ constant fractional volume curve), by showing this diameter on log scales with the leading linear $\check{n}$-dependence predicted from Eq. (4.43) taken off. For high values of f_{pm} we therefore see a leading nonlinear term with exponent $1/(2\tilde{\beta})$, in Fig. 4.4. Note that for $f_{\text{pm}} = 1$ the sub-sub-leading term in Eq. (4.43), with exponent $1/(2\beta)$, would kick in at a value of $|\check{n}|$ well inside the range shown. In order to see the first sub-leading term with exponent $1/(2\tilde{\beta})$ clearly we therefore used $f_{\text{pm}} = 0.05$. A small residue of this competition remains, causing the slight upward shift of the numerical data compared to the theory at low $|\check{n}|$.

As we decrease f_{pm} (Fig. 4.5), a crossover to the result without pressure mixing, Eq. (4.44),

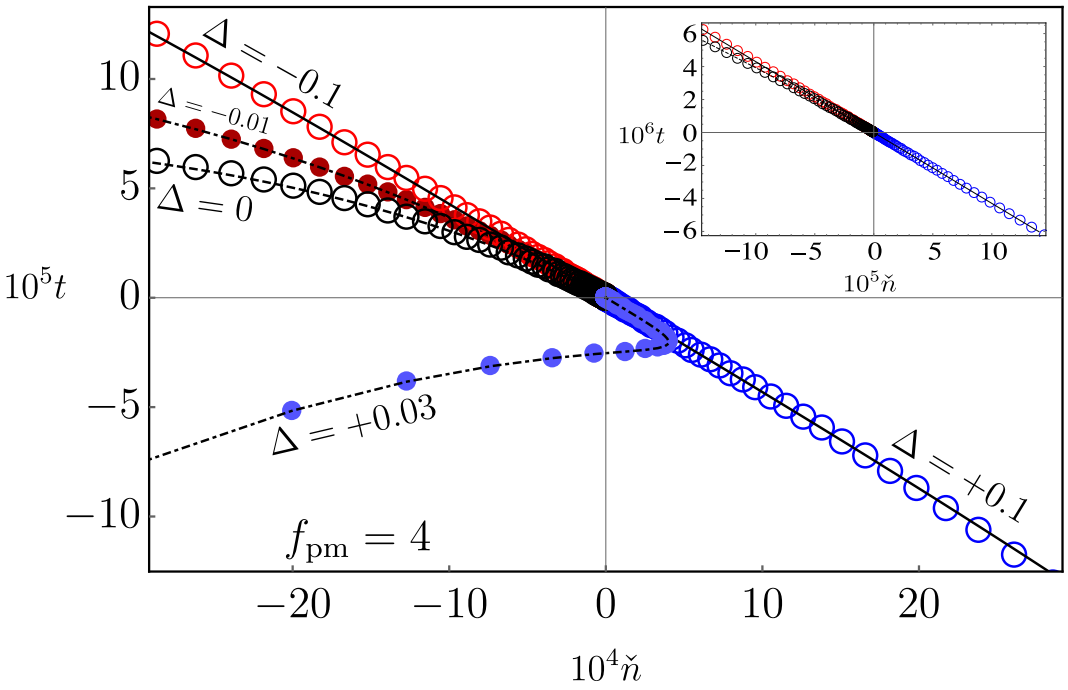

FIGURE 4.2: Constant fractional volume lines. Linear scale plot of numerical data (circles) and theoretical predictions (lines) for the lines defined by $\Delta = 0$ and $\Delta = \pm 0.1$. Strong pressure mixing, $f_{\rm pm} = 4$. Inset: zoom on the region close to the CP. Additional numerical data (small filled symbols and dash-dotted lines) are shown for two small $|\Delta|$, with Δ-values chosen in order to illustrate the smooth Δ-dependence of the curve away from the CP.

becomes visible inside our $|\check{n}|$-range. However, this occurs where the dominant term in Eq. (4.44) is already the one with exponent $1/(1-\alpha)$. At $f_{\rm pm} = 0$, finally, pressure mixing effects disappear and we observe only the term with exponent $1/(1-\alpha)$ (see Fig. 4.6). As in Fig. 4.5, there is in principle a linear contribution that arises because we are subtracting the linear prediction *with* pressure mixing, which has a different prefactor and so cannot cancel the linear term *without* pressure mixing. This should dominate at small $|\check{n}|$ but is quantitatively too small to be visible. We emphasize that in all cases the numerical data agree with the theoretical predictions agree not just in exponent (slope) but also in prefactor.

As discussed above in Section 4.4, Eq. (4.45) shows that in the 'with pressure mixing' regime the temperature difference $\delta t_0 = t_{\rm cloud} - t_{\Delta=0}$ between the cloud curve and the equal volume diameter should have no linear term in $\check{n}$; the leading contribution is singular, with exponent $1/(2\tilde{\beta})$ from Eq. (4.45). This is exactly what can be observed in Fig. 4.7. Subsequently, we would expect to see the term with exponent $1/(2\beta)$ as one moves away

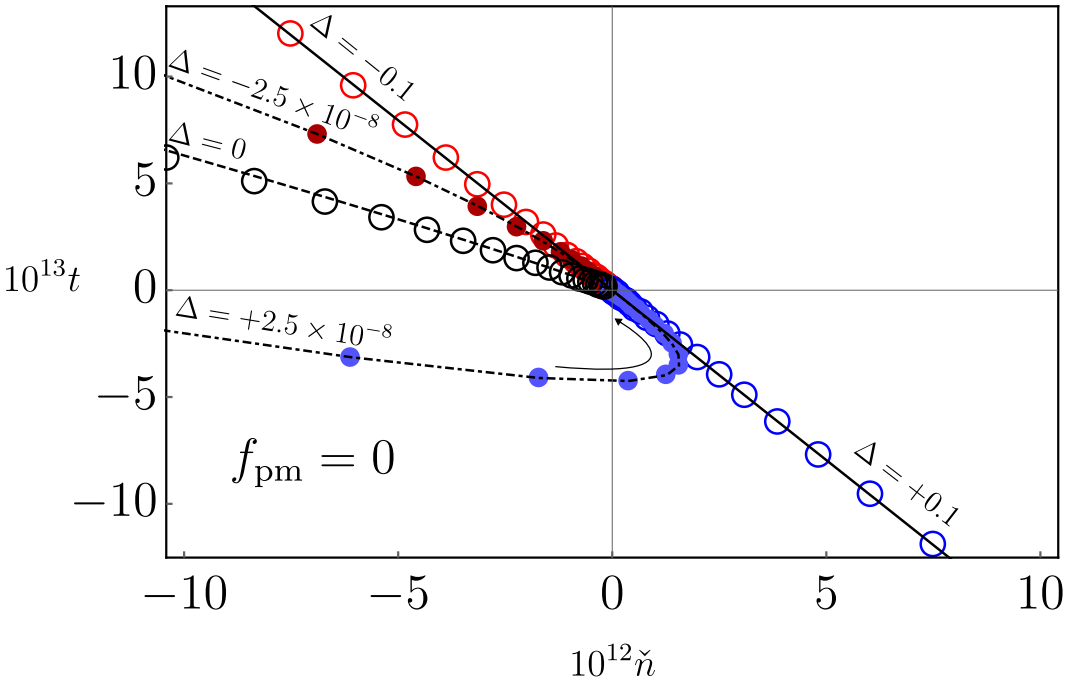

FIGURE 4.3: (Similar to Fig. 4.2.) No pressure mixing, $f_{\rm pm} = 0$; notice the distinct slope of the equal volume diameter ($\Delta = 0$ line). Again, additional numerical data (small filled symbols and dash-dotted lines) are shown for two small $|\Delta|$, with Δ-values chosen in order to illustrate the smooth Δ-dependence of the curve away from the CP.

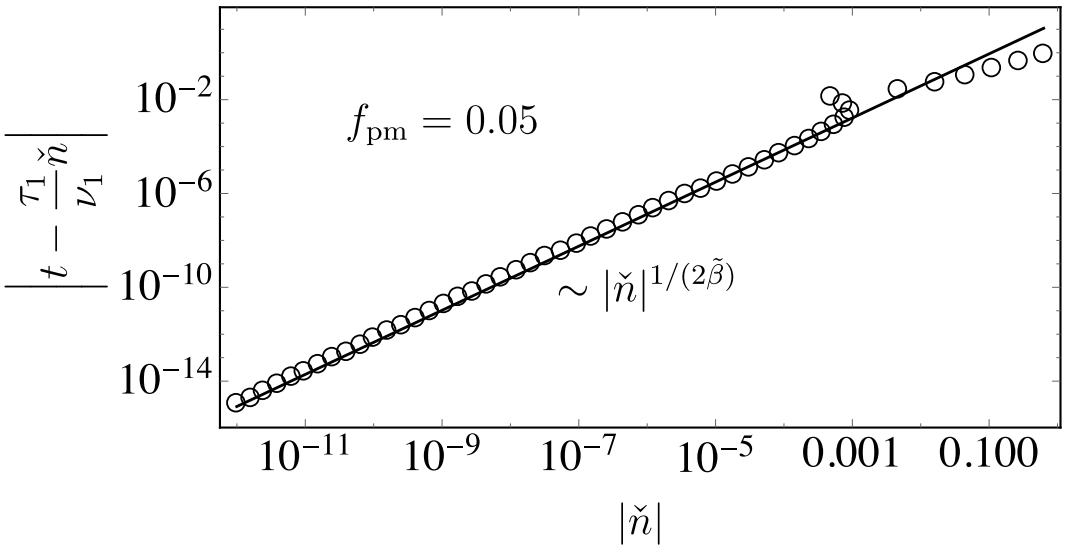

FIGURE 4.4: Equal volume diameter ($\Delta = 0$). Log-log plots of numerical data for $|t - \frac{\tau_1}{\nu_1}\check{n}|$ vs. $|\check{n}|$, i.e. with predicted leading term removed (empty circles). It shows a change of sign in $\check{n}$ at higher $|\check{n}|$. Lines are theoretical predictions. Moderate pressure mixing, $f_{\rm pm} = 0.05$, shows the leading power law term with exponent $1/(2\tilde{\beta}) \simeq 1.37$.

from CP. However, *before* this happens, a crossover to the 'without pressure mixing' regime occurs, where there is a leading linear piece from Eq. (4.46). This is however largely masked by the next term with exponent $1/(1-\alpha)$. If pressure mixing is switched off completely

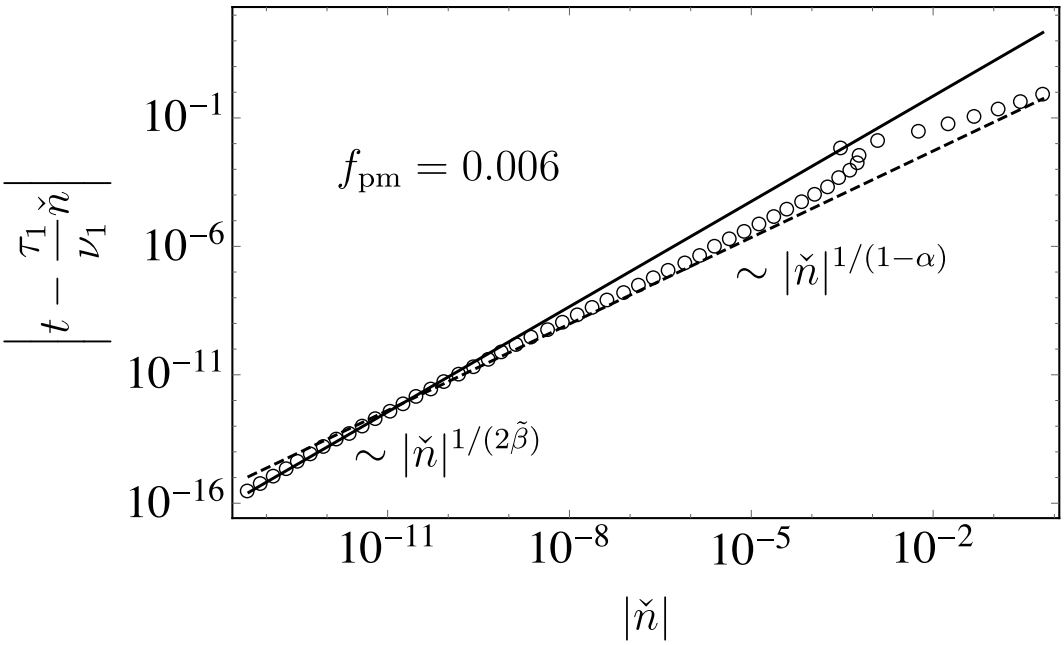

FIGURE 4.5: (Similar to Fig. 4.4.) Weak pressure mixing, $f_{\rm pm} = 0.006$, produces a crossover between power laws with pressure mixing (solid line) and without (dashed line, exponent $1/(1-\alpha) \simeq 1.12$).

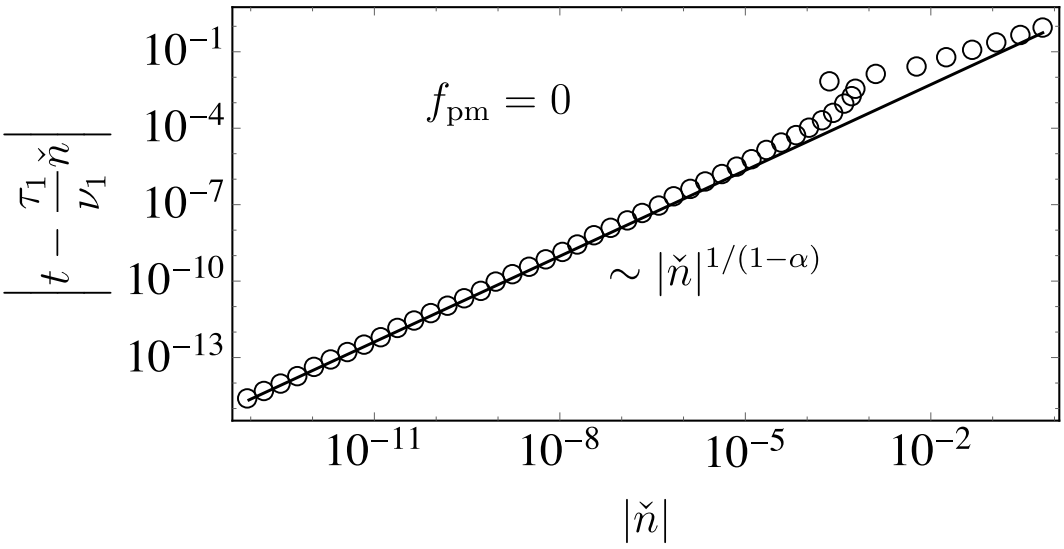

FIGURE 4.6: (Similar to Fig. 4.4.) No pressure mixing, $f_{\rm pm} = 0$.

($f_{\rm pm} = 0$), the linear contribution is clearly visible (see inset of Fig. 4.7) as well as the crossover to $|\check{n}|^{1/(1-\alpha)}$.

For our last set of numerical results for constant fractional volume we look in Figs. 4.8 and 4.9 at the $\Delta = 0$ coexistence curves of t vs. $\check{n}_{\pm}$, in order to verify Eq. (4.47). Even with weak pressure mixing ($f_{\rm pm} = 0.025$) the leading quadratic term can easily be discerned, as can a contribution that survives even without pressure mixing, with exponent $1/\beta$. The

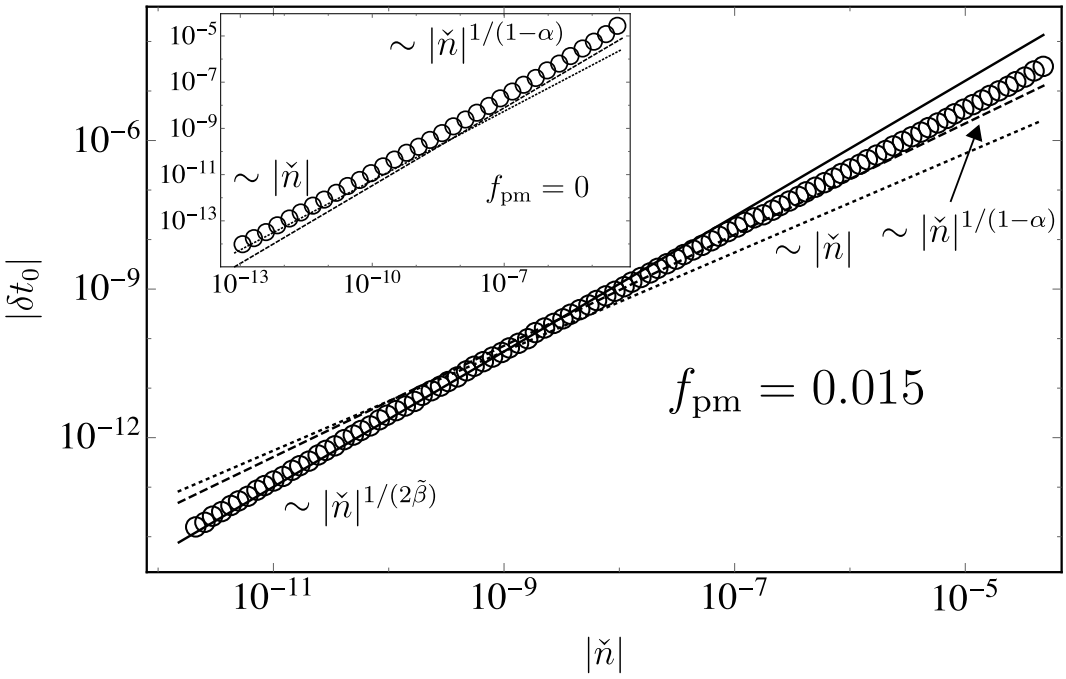

FIGURE 4.7: Temperature difference between cloud curve and equal volume diameter. Log-log plots of numerical data for $|\delta t_0|$ vs. $|\check{n}|$ at $f_{\rm pm} = 0.015$ (empty circles). Solid line: contribution with exponent $1/(2\tilde{\beta}) \simeq 1.37$ from the theoretical prediction. A crossover to the regime without pressure mixing is seen, where terms with exponents 1 (dotted) and $1/(1-\alpha) \simeq 1.12$ (dashed) compete, kick in around the same value of $|\check{n}|$. Inset: Without pressure mixing, $f_{\rm pm} = 0$, the term with exponent $1/(2\tilde{\beta})$ is absent.

terms with intermediate exponents 3 and $1/\tilde{\beta}$ cannot be seen as they are quantitatively too small. This is also why we do not plot the $\check{n}_-$ branch, which would differ from $\check{n}_+$ only by the small third order term. The inset shows the case $f_{\rm pm} = 0$: now only the terms with exponents $1/\tilde{\beta}$ and $1/\beta$ can be observed. This is as expected from Eq. (4.47) since without pressure mixing the terms with exponents 2 and 3 drop out. Fig. 4.9 is similar to Fig. 4.8, but now for larger $f_{\rm pm} = 2$. The quadratic term that signals pressure mixing is clearly visible starting from $\check{n} \simeq 10\%$ and extending for several decades towards the CP, suggesting that it could be amenable to relatively straightforward experimental verification.

Now we move on to the numerical results for fixed parent density $\check{n}$. At $\check{n} = 0$ we first consider (see Fig. 4.10) the dependence of the fractional volume parameter Δ on the temperature difference to the CP, $\delta t = -t$. Data for $f_{\rm pm} = 1$ and $f_{\rm pm} = 0$ clearly show the exponents and prefactors for the cases with and without pressure mixing as predicted by Eqs. (4.58) and (4.59), respectively. Note that close to the CP the difference $|\Delta|$ between the fractional volumes of the two coexisting phases is orders of magnitude larger with

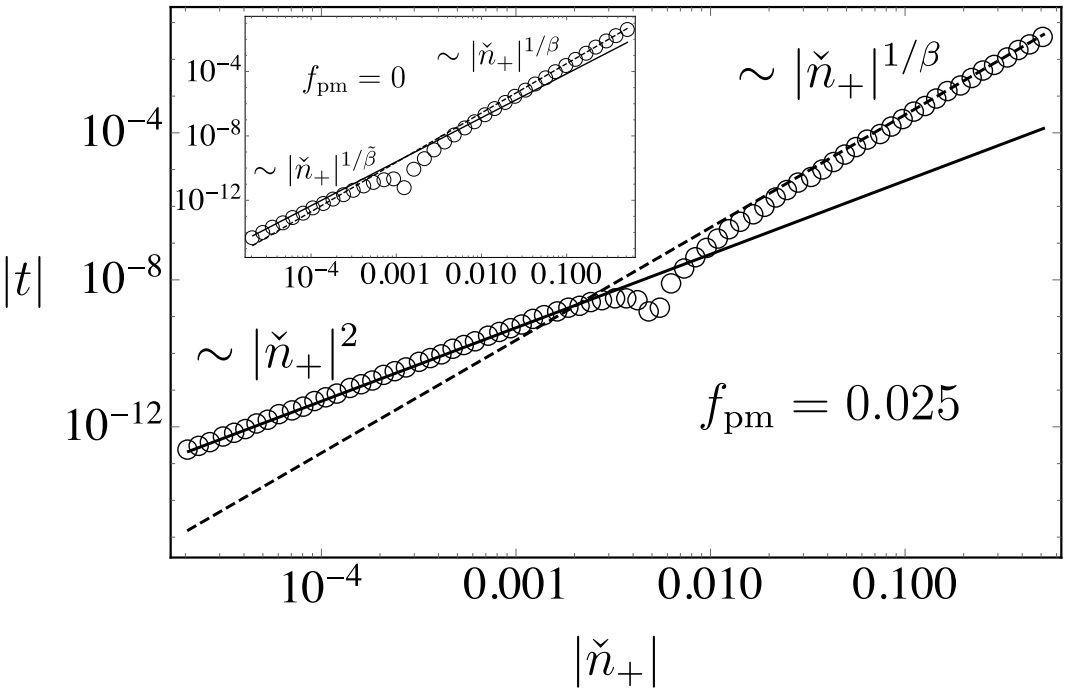

FIGURE 4.8: Equal fractional volume coexistence curve. Log-log plot of numerical data for $|t|$ vs. $|\check{n}_+|$ for $\Delta = 0$ at $f_{\rm pm} = 0.025$ (empty circles), showing a change of sign in t. Solid and dashed lines: theoretical predictions for the terms with exponent 2 and $1/\beta \simeq 3.07$, respectively. Inset: No pressure mixing, $f_{\rm pm} = 0$. As predicted, only contributions with exponents $1/\tilde{\beta} \simeq 2.73$ (solid) and $1/\beta$ (dashed) can be observed.

pressure mixing than without, suggesting a potential route for experimental detection of pressure mixing effects that would not require precise exponent measurements.

Keeping our focus on the critical parent ($\check{n} = 0$) we finally look at the midpoint diameter $\bar{n}$ vs. δt (Fig. 4.11), for which we have the theoretical prediction Eqs. (4.60) and (4.61) in the cases with and without pressure mixing. The leading order terms are seen clearly close to the CP. Notice in particular how without pressure mixing, the singular $\sim \delta t^{1-\alpha}$ dependence from the monodisperse case conspires with mixture effects to reproduce a rectilinear midpoint diameter, $|\check{n}| \sim \delta t$.

4.8 Conclusions and discussion

We have used complete scaling theory to relate standard 3D Ising criticality to polydisperse criticality, and thus to predict the scaling of a number of important properties of the phase diagram of polydisperse fluids. These predictions, which we summarise in Table 4.1, were also confirmed in comparisons with numerical evaluations of the full theory. We

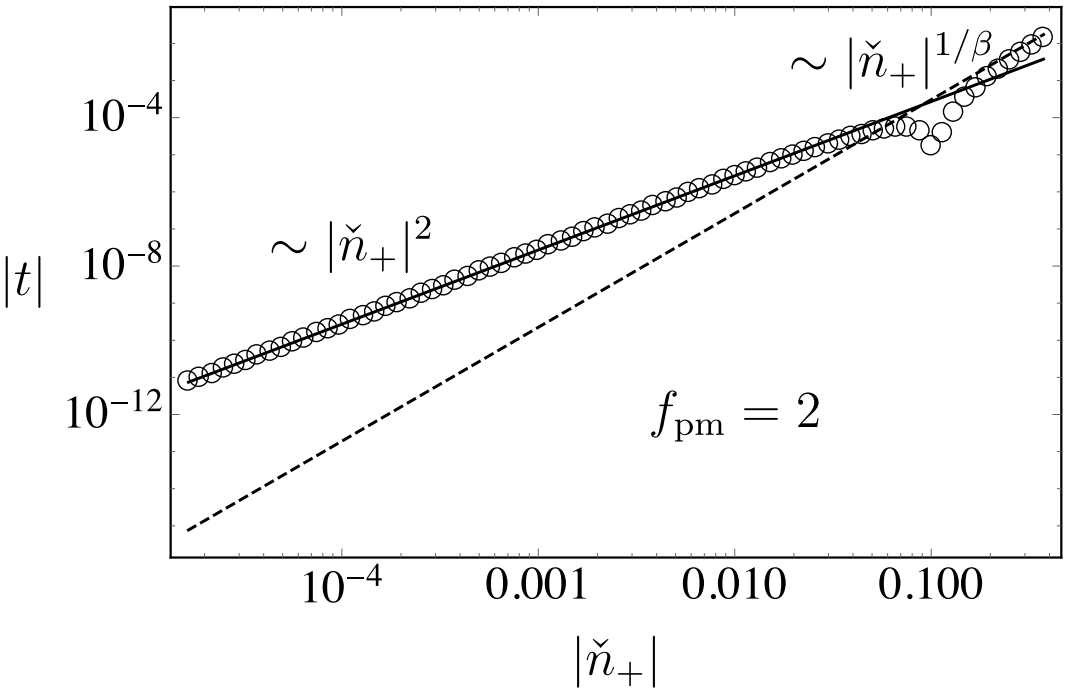

FIGURE 4.9: Similar to Fig. 4.8 but now with stronger pressure mixing, $f_{\rm pm} = 2$. The characteristic quadratic term is now visible as far as $\check{n} \simeq 10\%$ from the CP.

have emphasised the potential effects of pressure mixing in the scaling fields, and have highlighted a number of new observables that could be used to detect such effects.

A number of the potentially useful observables involve the equal volume diameter, which determines for any fixed overall (parent) density $\check{n}$ at what temperature a phase split with $\Delta = 0$, i.e. with equal fractional volumes occupied by the coexisting phases, is produced. From Table 4.1 we see that this diameter itself has a leading linear variation independently of pressure mixing. The distance δt_0 to the cloud curve, which is the extra temperature decrease that is required to get from the onset of phase separation to a 50–50 phase split, shows a clearer signature, with the leading density dependence being linear without pressure mixing but singular with exponent $1/2\tilde{\beta} \simeq 1.37$ when pressure mixing is present. The 50–50 coexistence curve, which records the coexisting densities for parents on the equal volume diameter, is likewise a potentially useful probe: its leading quadratic term disappears without pressure mixing.

For measurements at fixed critical parent density, the difference Δ of the fractional phase volumes also shows clear signatures of pressure mixing, with a smaller exponent ($\tilde{\beta}$ rather than $1 - \tilde{\beta}$) leading to significantly larger Δ near the critical point (CP) when

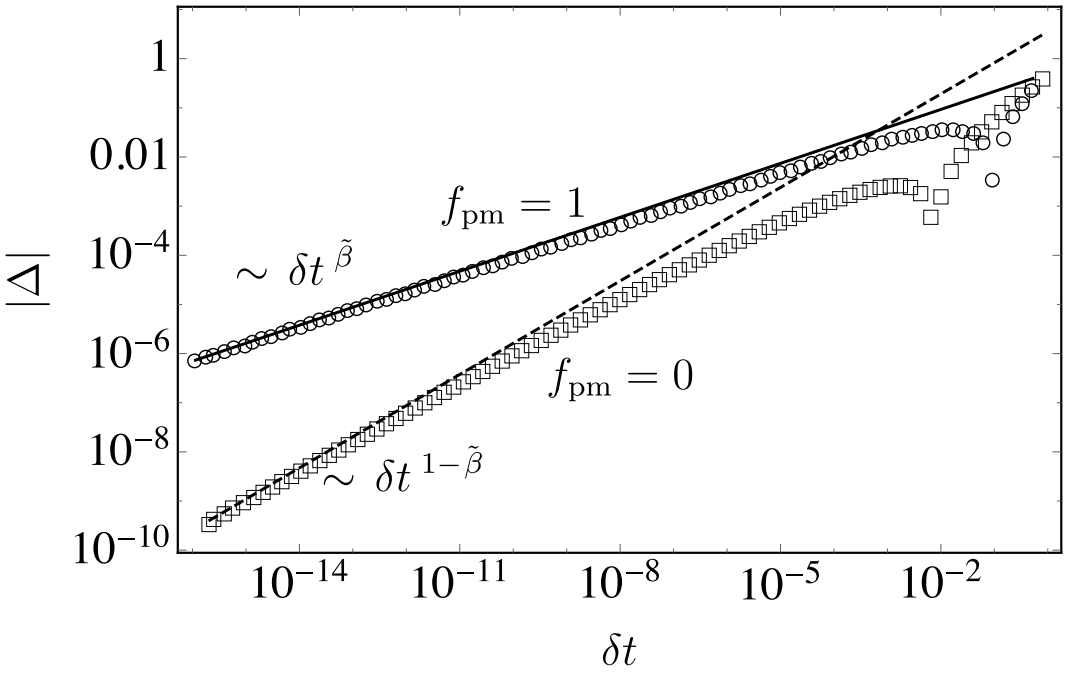

FIGURE 4.10: Difference in fractional volumes of coexisting phases produced from critical parent ($\check{n} = 0$). Log-log plots of numerical data for $|\Delta|$ vs. $|\delta t|$; Δ changes sign at larger δt. Data with pressure mixing ($f_{\rm pm} = 1$, empty circles) and without ($f_{\rm pm} = 0$, empty squares) agree well with the theoretically predicted power laws with exponents $\tilde{\beta} \simeq 0.37$ and $1 - \tilde{\beta} \simeq 0.63$, respectively.

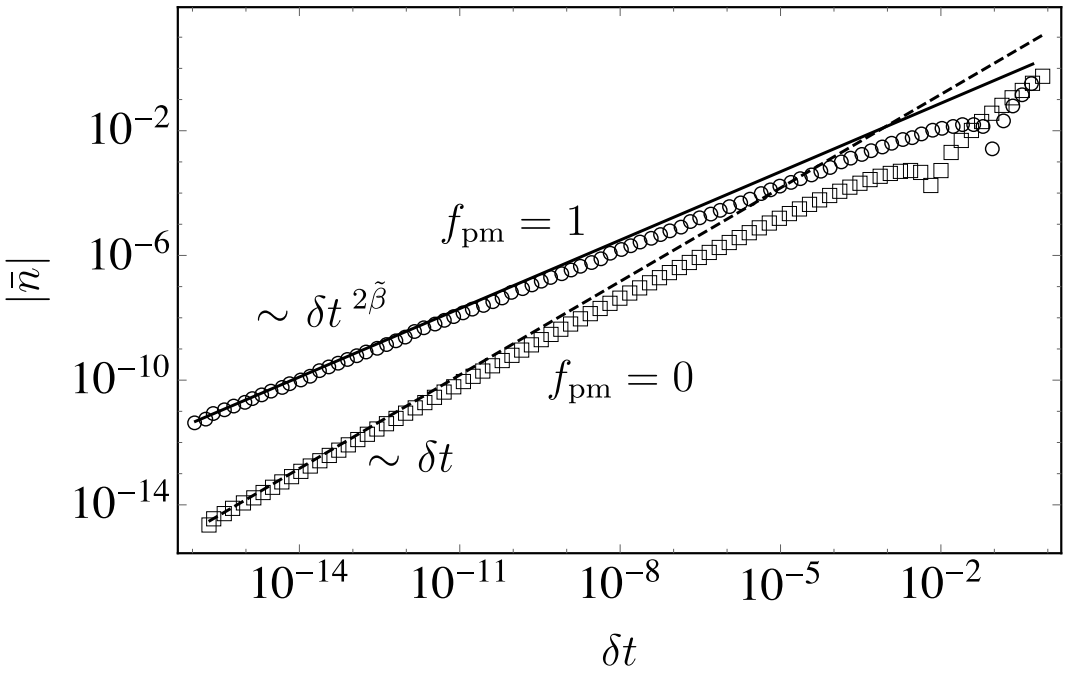

FIGURE 4.11: Midpoint diameter. Log-log plots of numerical data for $|\bar{n}|$ vs. $|\delta t|$ for fixed $\check{n} = 0$. For $f_{\rm pm} = 1$ (pressure mixing, empty circles), the solid line shows our prediction for the power law, with exponent $2\tilde{\beta} \simeq 0.73$. For $f_{\rm pm} = 0$ (no pressure mixing, empty squares), the predicted exponent is 1. The numerical data agree well with the predictions close to the CP.

TABLE 4.1: Summary of analytical results (without prefactors). Abbreviations: 'var.' = 'variable', 'diam.' = 'diameter', 'Frac.' = 'Fractional', 'vol.' = 'volume', and 'temp' = 'temperature'. Remember that $\delta t_0 \equiv t_{\text{cloud}} - t_{\Delta=0}$.

Curve	Fixed var.	With pressure mixing	Without pressure mixing	Figs.
Cloud and others	$\Delta \neq 0$	$t \sim \check{n} + \check{n}^2 + \lvert\check{n}\rvert^{1/\tilde{\beta}} + \check{n}^3 + \lvert\check{n}\rvert^{1/\beta}$	$t \sim \check{n} + \check{n}^2 + \lvert\check{n}\rvert^{1/\tilde{\beta}} + \check{n}^3 + \lvert\check{n}\rvert^{1/\beta}$	4.1, 4.2 & 4.3
Equal volume diam.	$\Delta = 0$	$t \sim \check{n} + \check{n}^{1/(2\tilde{\beta})} + \check{n}^{1/(2\beta)}$	$t \sim \check{n} + \check{n}^{1/(1-\alpha)}$	4.2, 4.3, 4.4, 4.5 & 4.6
$t_{\text{cloud}} - t_{\Delta=0}$ vs. $\check{n}$	$\Delta = \pm 1$ $\Delta = 0$	$\delta t_0 \sim \check{n}^{1/(2\tilde{\beta})} + \check{n}^{1/(2\beta)}$	$\delta t_0 \sim \check{n} \ + \ \check{n}^{1/(1-\alpha)}$	4.7
Shadow and others	$\Delta \neq 0$	$t \sim \check{n}_\pm + \check{n}_\pm^2 + \lvert\check{n}_\pm\rvert^{1/\tilde{\beta}} + \check{n}_\pm^3 + \lvert\check{n}_\pm\rvert^{1/\beta}$	$t \sim \check{n}_\pm + \check{n}_\pm^2 + \lvert\check{n}_\pm\rvert^{1/\tilde{\beta}} + \check{n}_\pm^3 + \lvert\check{n}_\pm\rvert^{1/\beta}$	4.1
50–50 coexistence	$\Delta = 0$	$t \sim \check{n}_\pm^2 + \lvert\check{n}_\pm\rvert^{1/\tilde{\beta}} + \check{n}_\pm^3 + \lvert\check{n}_\pm\rvert^{1/\beta}$	$t \sim \lvert\check{n}_\pm\rvert^{1/\tilde{\beta}} + \lvert\check{n}_\pm\rvert^{1/\beta}$	4.8 & 4.9
Coexistence curve	$\check{n} = 0$	$\delta t \sim \lvert\check{n}_\pm\rvert^{1/\tilde{\beta}} + \lvert\check{n}_\pm\rvert^{1/\beta}$	$\delta t \sim \lvert\check{n}_\pm\rvert^{1/\tilde{\beta}} + \lvert\check{n}_\pm\rvert^{1/\beta}$	N/A
Frac. vol. vs. temp.	$\check{n} = 0$	$\Delta \sim \delta t^{\tilde{\beta}}$	$\Delta \sim \delta t^{1-\tilde{\beta}}$	4.10
Midpoint diam.	$\check{n} = 0$	$\delta t \sim \bar{n}^{1/(2\tilde{\beta})} + \bar{n}^{1/(2\beta)}$ $\bar{n} \sim \delta t^{2\tilde{\beta}} + \delta t^{2\tilde{\beta}+\alpha/(1-\alpha)}$	$\delta t \sim \bar{n} + \bar{n}^{1/(1-\alpha)}$ $\bar{n} \sim \delta t + \delta t^{1/(1-\alpha)}$	4.11

pressure mixing is present. Finally, the midpoint diameter, defined as the average of the coexisting densities produced by a critical parent, is also sensitive to pressure mixing as found previously in the literature in analogous studies of monodisperse systems: the midpoint density $\bar{n}$ varies linearly with temperature without pressure mixing but singularly with exponent $2\tilde{\beta}$ when pressure mixing is present.

The above predictions are all amenable to experimental verification and as tools to detect pressure mixing effects. How easy this is will of course depend on the specific fluid system and in particular on the accuracy that can be achieved for measurements close to the CP. While we have found that some crossovers require quite a few orders of magnitude to see clearly, other properties like those connected to the equal fractional volume coexistence curve (Section 4.4) should be more easily accessible.

We note that in Ref. [111], where a complete scaling theory for weakly compressible

binary liquids was developed, the authors used literature data [117] to show that the effective leading-order exponent of the midpoint diameter is 0.75, whereas the predicted leading and subleading exponents were respectively $2\beta \simeq 0.65$ and $1-\alpha \simeq 0.89$. A possible explanation is that the data falls within a crossover range. Alternatively there could be impurities in the experimental set-up that would act as a hidden field in the calculations, resulting in the Fisher-renormalisation [118] of the leading exponent that we also find. This would change the exponent from 2β to $2\tilde{\beta} = 2\beta/(1-\alpha) \simeq 0.73$ (see Ref. [110]), close to the experimental result. Note that our results do not directly apply to the fixed pressure situation considered in Ref. [111] since we have kept overall density fixed instead. (Fisher renormalisation of exponents at fixed composition and density was already found and discussed in Ref. [119] for the simpler revised scaling approach, in the context of binary mixtures.)

It is interesting to observe that if we were dealing with mean-field criticality, where $\alpha = 0$ and $\beta = \tilde{\beta} = 1/2$, all terms that we have derived in the expansion of both the midpoint and equal volume diameters would simply degenerate to linear contributions, though – as one might expect on general grounds due to fractionation – the prefactors would differ between the two diameter definitions.

In future work we plan to look at additional properties of polydisperse colloidal fluids using the same setup presented here, i.e. a framework for polydisperse fluids with complete scaling, in the experimentally relevant case of controlled overall particle density. Such properties could include Tolman's length [120], dielectric constant [121], refractive index [122], thermal and transport properties [119,123,124], and more generally other properties that can be obtained from the dependence of the pressure on the other variables [125]. It will be interesting to see what new physical insights can be gained from the inclusion of polydispersity and potential pressure mixing effects. We also plan to study more closely the crossover between monodisperse and polydisperse critical behaviour that one expects to see in weakly polydisperse systems, building on perturbative approaches to polydisperse critical behaviour [44].

Appendices

4.A Expansion coefficients from mixing coefficients

As explained in the main text, by inserting Eqs. (4.30)–(4.33) into Eqs. (4.26)–(4.29), and comparing terms order by order, we obtain sets of equations that involve no thermodynamic variables, i.e. they contain only coefficients. These can be solved to extract the expansion coefficients $\nu_i, \nu_i', \pi_i, \pi_i', \tau_i, \tau_i', \boldsymbol{m}_i$ and $\boldsymbol{m}_i'$ in terms of the mixing coefficients. The conditions for the $\mathscr{O}(\Delta\tilde{\rho})$ coefficients are

$$
\begin{aligned}
0 &= \pi_1 - k_0\tau_1 - \boldsymbol{f}^{\mathrm{T}}\boldsymbol{m}_1 && (4.64)\\
0 &= -j_1\pi_1 + \tau_1 - \boldsymbol{l}_1^{\mathrm{T}}\boldsymbol{m}_1 && (4.65)\\
0 &= -j_2\pi_1 - k_2\tau_1 + \boldsymbol{l}_2^{\mathrm{T}}\boldsymbol{m}_1 && (4.66)\\
-\tilde{\boldsymbol{l}}_2 &= -\boldsymbol{f}\nu_1 + (2m_0\boldsymbol{f} + \boldsymbol{n}_3)\pi_1 + (n_0\boldsymbol{f} + \boldsymbol{v}_0)\tau_1 + (\boldsymbol{f}\boldsymbol{n}_3^{\mathrm{T}} + 2\boldsymbol{q}_0)\boldsymbol{m}_1 && (4.67)
\end{aligned}
$$

while for $\mathscr{O}(\tilde{\rho}^2)$ one gets

$$
\begin{aligned}
0 &= \pi_2 - k_0\tau_2 - \boldsymbol{f}^{\mathrm{T}}\boldsymbol{m}_2 && (4.68)\\
0 &= -j_1\pi_2 + \tau_2 - \boldsymbol{l}_1^{\mathrm{T}}\boldsymbol{m}_2 && (4.69)\\
0 &= -j_2\pi_2 - k_2\tau_2 + \boldsymbol{l}_2^{\mathrm{T}}\boldsymbol{m}_2 && (4.70)\\
j_2\tilde{\boldsymbol{l}}_2 &= -\boldsymbol{f}\nu_2 + (2m_0\boldsymbol{f} + \boldsymbol{n}_3)\pi_2 + (n_0\boldsymbol{f} + \boldsymbol{v}_0)\tau_2 + (\boldsymbol{f}\boldsymbol{n}_3^{\mathrm{T}} + 2\boldsymbol{q}_0)\boldsymbol{m}_2 && (4.71)
\end{aligned}
$$

The analogous relations for the coefficients of the $\mathscr{O}(\tilde{\rho}^{1/\tilde{\beta}})$ terms read

$$\begin{aligned} 0 &= \pi_3 - k_0\tau_3 - \boldsymbol{f}^{\mathrm{T}}\boldsymbol{m}_3 && (4.72)\\ 0 &= -j_1\pi_3 + \tau_3 - \boldsymbol{l}_1^{\mathrm{T}}\boldsymbol{m}_3 && (4.73)\\ 0 &= -j_2\pi_3 - k_2\tau_3 + \boldsymbol{l}_2^{\mathrm{T}}\boldsymbol{m}_3 && (4.74)\\ -b(j_1\boldsymbol{f}+\boldsymbol{l}_1) &= -\boldsymbol{f}\nu_3 + (2m_0\boldsymbol{f}+\boldsymbol{n}_3)\pi_3 + (n_0\boldsymbol{f}+\boldsymbol{v}_0)\tau_3 \\ &\quad + (\boldsymbol{f}\boldsymbol{n}_3^{\mathrm{T}} + 2\boldsymbol{q}_0)\boldsymbol{m}_3 && (4.75) \end{aligned}$$

and finally for $\mathscr{O}(\tilde{\rho}^{1/\beta})$:

$$\begin{aligned} 0 &= \pi_5 - k_0\tau_5 - \boldsymbol{f}^{\mathrm{T}}\boldsymbol{m}_5 && (4.76)\\ -a &= -j_1\pi_5 + \tau_5 - \boldsymbol{l}_1^{\mathrm{T}}\boldsymbol{m}_5 && (4.77)\\ 0 &= -j_2\pi_5 - k_2\tau_5 + \boldsymbol{l}_2^{\mathrm{T}}\boldsymbol{m}_5 && (4.78)\\ 0 &= -\boldsymbol{f}\nu_5 + (2m_0\boldsymbol{f}+\boldsymbol{n}_3)\pi_5 + (n_0\boldsymbol{f}+\boldsymbol{v}_0)\tau_5 + (\boldsymbol{f}\boldsymbol{n}_3^{\mathrm{T}} + 2\boldsymbol{q}_0)\boldsymbol{m}_5. && (4.79) \end{aligned}$$

These conditions all take the same form because they relate to terms that are *linear* in the 'input variables' of the expansion described in the main text, i.e. $\Delta\tilde{\rho}$, $\tilde{\rho}^2$, $b\tilde{\rho}^{1/\tilde{\beta}}$ and $\tilde{\rho}^{1/\beta}$. The $(\Delta\tilde{\rho})^2$ and third order terms in the expansions (4.30)–(4.33) are quadratic or third order in these input variables; the equations for their coefficients would therefore involve higher order mixing coefficients that we have not written down in Eqs. (4.4)–(4.6), so we do not state them here.

The conditions above are in principle straightforward to solve, requiring only the inversion of the $(M+3)\times(M+3)$ coefficient matrix on the right hand side. One expects that all coefficients must generically be nonzero, although the monodisperse case is exceptional (see Section 4.5). Note that one can always proceed by first obtaining $\boldsymbol{m}_i$ ($i = 1,3,5$) from the last equation of each set to reduce the problem to three linear equations for the remaining expansion coefficients. This first step involves the inversion of the matrix $\boldsymbol{f}\boldsymbol{n}_3^{\mathrm{T}} + 2\boldsymbol{q}_0$. Except for $M = 1$ this requires a nonzero (and in general full-rank, invertible) $\boldsymbol{q}_0$, supporting our conclusion in the main text that nonlinear mixing effects as specified by $\boldsymbol{q}_0$ need to be accounted for to obtain a meaningful description of critical mixture behaviour.

We note finally that the inhomogeneities on the left hand sides of (4.64)—(4.67) and (4.68)—(4.71) are directly proportional to each other. Accordingly the expansion coefficients for $O(\Delta\tilde{\rho})$ and $O(\tilde{\rho}^2)$ terms that these equations determine are likewise proportional:

$$\nu_2 = -j_2\nu_1, \quad \tau_2 = -j_2\tau_1, \quad \pi_2 = -j_2\pi_1, \quad \boldsymbol{m}_2 = -j_2\boldsymbol{m}_1. \tag{4.80}$$

From these results one deduces, in particular, that $\tilde{\tau}_2 = 0$ as explained in Section 4.4 in the main text.

4.B Coexisting densities

In the following we present a number of additional analytical results (and intermediate steps) for the coexisting densities $\check{n}_\pm$ in both fixed-Δ and fixed-$\check{n}$ contexts. We start by writing down the result for t vs. $\check{n}_\pm$ for fixed Δ (see Section 4.4):

$$\begin{aligned}
t \;=\; & \frac{\tau_1\Delta}{\pm\tilde{l}_2+\Delta(\nu_1-\tilde{l}_2)}\check{n}_\pm \\
& - \left[\frac{[\nu_2 \pm g_2\Delta + (\nu_2'-g_2)\Delta^2]\tau_1\Delta}{\pm\tilde{l}_2+\Delta(\nu_1-\tilde{l}_2)} - \tau_2 + \tau_2'\Delta^2\right]\left(\frac{\check{n}_\pm}{\pm\tilde{l}_2+\Delta(\nu_1-\tilde{l}_2)}\right)^2 \\
& - \left(\frac{\nu_3\tau_1\Delta}{\pm\tilde{l}_2+\Delta(\nu_1-\tilde{l}_2)} - \tau_3\right)\left(\frac{\check{n}_\pm}{\pm\tilde{l}_2+\Delta(\nu_1-\tilde{l}_2)}\right)^{1/\tilde{\beta}} \\
& - \left\{\frac{[\pm g_4 + (\nu_4-g_4)\Delta \pm g_4'\Delta^2 + (\nu_4'-g_4')\Delta^3]\tau_1\Delta}{\pm\tilde{l}_2+\Delta(\nu_1-\tilde{l}_2)} - (\tau_4\Delta+\tau_4'\Delta^3)\right. \\
& - 2\left(\frac{\nu_2 \pm g_2\Delta + (\nu_2'-g_2)\Delta^2}{\pm\tilde{l}_2+\Delta(\nu_1-\tilde{l}_2)}\right)\left[\frac{[\nu_2 \pm g_2\Delta + (\nu_2'-g_2)\Delta^2]\tau_1\Delta}{\pm\tilde{l}_2+\Delta(\nu_1-\tilde{l}_2)}\right. \\
& \left.\left. - (\tau_2+\tau_2'\Delta^2)\right]\right\}\left(\frac{\check{n}_\pm}{\pm\tilde{l}_2+\Delta(\nu_1-\tilde{l}_2)}\right)^3 \\
& - \left(\frac{\nu_5\tau_1\Delta}{\pm\tilde{l}_2+\Delta(\nu_1-\tilde{l}_2)} - \tau_5\right)\left(\frac{\check{n}_\pm}{\pm\tilde{l}_2+\Delta(\nu_1-\tilde{l}_2)}\right)^{1/\beta}.
\end{aligned} \tag{4.81}$$

As pointed out in the main text, the shadow curve is obtained by taking $\check{n}_\pm$ for $\Delta = \mp 1$, giving

$$\begin{aligned} t &= \frac{\tau_1}{\nu_1 - 2\tilde{l}_2}\check{n}_\pm - \left[\frac{(\nu_2+\nu_2'-2g_2)\tau_1}{\nu_1-2\tilde{l}_2} - (\tau_2+\tau_2')\right]\left(\frac{\check{n}_\pm}{\nu_1-2\tilde{l}_2}\right)^2 \\ &\quad - \left(\frac{\nu_3\tau_1}{\nu_1-2\tilde{l}_2} - \tau_3\right)\left|\frac{\check{n}_\pm}{\nu_1-2\tilde{l}_2}\right|^{1/\tilde{\beta}} - \left\{\frac{[\nu_4+\nu_4'-2(g_4+g_4')]\tau_1}{\nu_1-2\tilde{l}_2} - (\tau_4+\tau_4')\right. \\ &\quad \left. - 2\left(\frac{\nu_2+\nu_2'-2g_2}{\nu_1-2\tilde{l}_2}\right)\left[\frac{(\nu_2+\nu_2'-2g_2)\tau_1}{\nu_1-2\tilde{l}_2} - (\tau_2+\tau_2')\right]\right\}\left(\frac{\check{n}_\pm}{\nu_1-2\tilde{l}_2}\right)^3 \\ &\quad - \left(\frac{\nu_5\tau_1}{\nu_1-2\tilde{l}_2} - \tau_5\right)\left|\frac{\check{n}_\pm}{\nu_1-2\tilde{l}_2}\right|^{1/\beta}. \end{aligned} \tag{4.82}$$

To obtain the coexisting densities at fixed $\check{n}$ (Section 4.6) rather than fixed Δ as above, one starts from the general expansion (4.36) and then uses Eq. (4.51) to eliminate $\Delta\tilde{\rho}$, to obtain an expansion in terms of $\tilde{\rho}$ only:

$$\begin{aligned} \check{n}_\pm &= \check{n} \pm \tilde{l}_2\tilde{\rho} - \tilde{l}_2\Delta\tilde{\rho} \pm g_2\tilde{\rho}(\Delta\tilde{\rho}) - g_2(\Delta\tilde{\rho}^2) \pm g_4\tilde{\rho}^3 - g_4\tilde{\rho}^2(\Delta\tilde{\rho}) \\ &\quad \pm g_4'\tilde{\rho}(\Delta\tilde{\rho})^2 - g_4'(\Delta\tilde{\rho})^3 \qquad (4.83) \\ &= \left(1-\frac{\tilde{l}_2}{\nu_1}\right)\check{n} \pm \tilde{l}_2\tilde{\rho} + \frac{\nu_2\tilde{l}_2}{\nu_1}\tilde{\rho}^2 \pm g_2\tilde{\rho}\frac{\check{n}}{\nu_1} + \left(\frac{\nu_2'\tilde{l}_2}{\nu_1} - g_2\right)\left(\frac{\check{n}}{\nu_1}\right)^2 + \frac{\nu_3\tilde{l}_2}{\nu_1}\tilde{\rho}^{1/\tilde{\beta}} \\ &\quad \pm \left(g_4 - \frac{\nu_2 g_2}{\nu_1}\right)\tilde{\rho}^3 + \left[-g_4 + \frac{\nu_4\tilde{l}_2}{\nu_1} + 2\frac{\nu_2}{\nu_1}\left(g_2 - \frac{\nu_2'\tilde{l}_2}{\nu_1}\right)\right]\tilde{\rho}^2\frac{\check{n}}{\nu_1} \\ &\quad \pm \left(g_4' - \frac{\nu_2' g_2}{\nu_1}\right)\tilde{\rho}\left(\frac{\check{n}}{\nu_1}\right)^2 + \left[-g_4' + \frac{\nu_4'\tilde{l}_2}{\nu_1} + 2\frac{\nu_2'}{\nu_1}\left(g_2 - \frac{\nu_2'\tilde{l}_2}{\nu_1}\right)\right]\left(\frac{\check{n}}{\nu_1}\right)^3 \\ &\quad + \frac{\nu_5\tilde{l}_2}{\nu_1}\tilde{\rho}^{1/\beta}. \qquad (4.84) \end{aligned}$$

As explained in the main text, one can then determine $\tilde{\rho}$ from this expression to eliminate it from a similar expansion for the temperature, Eq. (4.53), in order to determine the temperature dependence of the coexisting densities $\check{n}_\pm$ at fixed $\check{n}$ that is stated in Eq. (4.55). For the diameter, defined as $\bar{n} \equiv \frac{1}{2}(\check{n}_+ + \check{n}_-)$, one can proceed similarly. Starting again from

Eq. (4.36) and using (4.50)

$$\bar{n} = \check{n} - \Delta[\tilde{l}_2\tilde{\rho} + g_2\Delta\tilde{\rho}^2 + g_4\tilde{\rho}^3 + g_4'\Delta^2\tilde{\rho}^3] \tag{4.85}$$

$$= (\nu_1 - \tilde{l}_2)\Delta\tilde{\rho} + (\nu_2 - g_2\Delta + \nu_2'\Delta^2)\tilde{\rho}^2 + \nu_3\tilde{\rho}^{1/\tilde{\beta}} + (g_4 + \nu_4\Delta + g_4'\Delta^2 + \nu_4'\Delta^3)\tilde{\rho}^3 + \nu_5\tilde{\rho}^{1/\beta}. \tag{4.86}$$

Once Δ has been eliminated to fix $\check{n}$, again using Eq. (4.51), this becomes

$$\begin{aligned}\bar{n} = {} & \left(1 - \frac{\tilde{l}_2}{\nu_1}\right)\check{n} + \left(\frac{\nu_2'\tilde{l}_2}{\nu_1} - g_2\right)\left(\frac{\check{n}}{\nu_1}\right)^2 + \frac{\nu_2\tilde{l}_2}{\nu_1}\tilde{\rho}^2 \\ & + \frac{\nu_3\tilde{l}_2}{\nu_1}\tilde{\rho}^{1/\tilde{\beta}} + \frac{\check{n}}{\nu_1}\tilde{\rho}^2\left[\frac{2j_2\tilde{l}_2\nu_2'}{\nu_1} + \frac{\tilde{l}_2\nu_4}{\nu_1} - 2j_2g_2 - g_4\right] \\ & + \left(\frac{\check{n}}{\nu_1}\right)^3\left[\frac{2g_2\nu_2'}{\nu_1} - \frac{2\tilde{l}_2\nu_2'^2}{\nu_1^2} + \frac{\tilde{l}_2\nu_4'}{\nu_1} - g_4'\right] + \frac{\nu_5\tilde{l}_2}{\nu_1}\tilde{\rho}^{1/\beta}\end{aligned} \tag{4.87}$$

Again one has to eliminate $\tilde{\rho}$. For the diameter it is convenient to have an expression for $\bar{n}$ in terms of δt rather than vice versa, so here one solves Eq. (4.53) for $\tilde{\rho}$. Focussing on the simplest case $\check{n} = 0$, this yields

$$\tilde{\rho} = \left(\frac{\delta t}{\tilde{\tau}_3}\right)^{\tilde{\beta}} - \tilde{\beta}\frac{\tilde{\tau}_5}{\tilde{\tau}_3}\left(\frac{\delta t}{\tilde{\tau}_3}\right)^{\tilde{\beta}+\alpha/(1-\alpha)}. \tag{4.88}$$

and after insertion into Eq. (4.87) one finds (4.60). When pressure mixing is absent, one can check by going back to Eq. (4.51) that, again for $\check{n} = 0$, all terms with integer powers vanish in Eq. (4.87):

$$\bar{n} = \frac{\tilde{l}_2}{\nu_1}\left(\nu_3\tilde{\rho}^{1/\tilde{\beta}} + \nu_5\tilde{\rho}^{1/\beta}\right). \tag{4.89}$$

Eliminating $\tilde{\rho}$ again using Eq. (4.88) then leads to Eq. (4.61) in the main text.

4.C Equivalence between mixtures with different numbers of species

In this appendix we explain how the critical phase behaviour of a fluid mixture with a certain number of species can be described equivalently in terms of a mixture with an

'inflated' number of species. As explained in the main text, this is useful in order to understand how the monodisperse limit can be approached starting from a polydisperse system.

Consider a mixture with M' species and mixing coefficients $j'_1, j'_2, k'_0, k'_2, \boldsymbol{l}'_0, \boldsymbol{l}'_1, \boldsymbol{l}'_2, \boldsymbol{q}'_0$, etc. We want to map it onto a system with $M > M'$ and mixing coefficients $j_1, j_2, k_0, k_2, \boldsymbol{l}_0$, $\boldsymbol{l}_1, \boldsymbol{l}_2, \boldsymbol{q}_0$, etc. such that both systems are physically equivalent with respect to their phase behaviour near the critical point. We nominally create new species by 'painting' particles, allowing them to be distinguished by an additional colour label without changing any of their physical properties. Each original species is thus divided into one or more coloured subspecies, in such a way that

$$\rho'_i = \sum_{j \in i} \rho_j \tag{4.90}$$

where ρ'_i is the density of a particle species i in the original labelling and the ρ_j are similarly the densities of the subspecies arising from i by colouring, as indicated symbolically in the sum by the notation $j \in i$. In terms of the new, M-species description, the free energy density of the system is (setting $k_B = 1$ here)

$$f = T \sum_{j=1}^{M} \rho_j (\ln \rho_j - 1) + f_{\text{ex}}(\{\rho'_i\}) \tag{4.91}$$

where f_{ex} is the excess free energy density and can be expressed as a function of the original composition $\{\rho'_i\}$ since colouring the particles by definition does not affect their physical interactions.

The chemical potentials of the coloured particles are obtained from f by differentiation as

$$\mu_j = \frac{\partial f}{\partial \rho_j} = T \ln \rho_j + \frac{\partial f_{\text{ex}}(\{\rho'_i\})}{\partial \rho_j} \tag{4.92}$$

Now because of Eq. (4.90), changing ρ_j changes only the density ρ'_i of the original species that subspecies j belongs to, by the same amount. It follows that

$$\mu_j - T \ln \rho_j = \frac{\partial f_{\text{ex}}}{\partial \rho'_i} \qquad \text{for all } j \in i \tag{4.93}$$

The intuitive content of this relation is that the excess chemical potential, which encodes the physical properties of each particle type, is the same for subspecies j as for the original

species i that was coloured to obtain j.

Now consider a small change $d\mu_j$ in all subspecies chemical potentials. Eq. (4.93) then implies

$$d\mu_j = T\frac{d\rho_j}{\rho_j} + \sum_k \frac{\partial^2 f_{ex}}{\partial\rho'_i \partial\rho'_k}\, d\rho'_k \tag{4.94}$$

Multiplying by ρ_j and summing over $j \in i$ gives, using on the r.h.s. again (4.90),

$$\sum_{j\in i} \rho_j\, d\mu_j = T\, d\rho'_i + \sum_k \rho'_i \frac{\partial^2 f_{ex}}{\partial\rho'_i \partial\rho'_k}\, d\rho'_k \tag{4.95}$$

This can be read as a vector equation for the density changes $d\rho'_i$ of the original species as a function of the weighted chemical potential changes associated with each original species, $\sum_{j\in i} \rho_j\, d\mu_j$, on the l.h.s. In particular, if these weighted changes are all zero, then also the original species densities remain unchanged, $d\rho'_i \equiv 0$. As we are keeping temperature T fixed, also pressure must then remain unchanged. In summary, any chemical potential change that obeys

$$\sum_{j\in i} \rho_j\, d\mu_j = 0 \tag{4.96}$$

for all i will not change the physical state of the system in any way. (What it will modify is the physically irrelevant distribution of coloured subspecies within each physical particle species.) In the mapping equations (4.4)–(4.6), such a chemical potential change must then leave the Ising scaling variables on the l.h.s. unchanged, as well as the temperature t and pressure $\check{p}$ on the r.h.s.

The above invariance with respect to most changes of the chemical potentials for the labelled particle species puts significant constraints on the mixing coefficients for the M-species system in Eqs. (4.4)–(4.6) as we now show. Consider first the simplest case $M' = 1$. In vector form, the chemical potential changes we are considering obey $\check{\boldsymbol{\rho}}^{\mathrm{T}} d\check{\boldsymbol{\mu}} = 0$; we can use the shifted and scaled chemical potentials $\check{\boldsymbol{\mu}}$ here because their changes are proportional to those of the conventional chemical potentials. For any such $d\check{\boldsymbol{\mu}}$ the Ising scaling pressure must not change, hence $d\tilde{p} = (\partial\tilde{p}/\partial\check{\boldsymbol{\mu}})^{\mathrm{T}} d\check{\boldsymbol{\mu}} = 0$. This implies that the vectors $\check{\boldsymbol{\rho}}$ and $\partial\tilde{p}/\partial\check{\boldsymbol{\mu}}$ are proportional as otherwise one could find a $d\check{\boldsymbol{\mu}}$ that is orthogonal to $\check{\boldsymbol{\rho}}$ but not to $\partial\tilde{p}/\partial\check{\boldsymbol{\mu}}$. Applying the same logic to the other two scaling variables shows

that

$$\check{\boldsymbol{\rho}} \propto \frac{\partial \tilde{p}}{\partial \check{\boldsymbol{\mu}}} \propto \frac{\partial \tilde{t}}{\partial \check{\boldsymbol{\mu}}} \propto \frac{\partial \tilde{h}}{\partial \check{\boldsymbol{\mu}}} \tag{4.97}$$

In other words, at any state point the gradients of the three mapping equations w.r.t. the chemical potentials must be proportional to each other. Writing out the gradient for e.g. $\tilde{p}$ from Eq. (4.4) one has

$$\frac{\partial \tilde{p}}{\partial \check{\boldsymbol{\mu}}} = -\boldsymbol{l}_0 - 2\boldsymbol{q}_0\check{\boldsymbol{\mu}} - t\boldsymbol{v}_0 - \check{p}\boldsymbol{n}_3 \tag{4.98}$$

At the critical point this reduces to $-\boldsymbol{l}_0$, and comparing with the analogous gradients for $\tilde{t}$ and $\tilde{h}$ shows that

$$\boldsymbol{l}_0 \propto \boldsymbol{l}_1 \propto \boldsymbol{l}_2 \tag{4.99}$$

As $\boldsymbol{l}_0 = \boldsymbol{f}$, also $\boldsymbol{l}_1$ and $\boldsymbol{l}_2$ must then be proportional to $\boldsymbol{f}$, and it remains to fix their normalisation. This can be done by comparing Eq. (4.21) for the densities $\check{\boldsymbol{\rho}}$ in the coloured (M-species) system with the analogous expression for the density in the original $M' = 1$ system. Using the constraint that the labelled densities must add up to the original density, Eq. (4.90), then shows that we must have $\boldsymbol{e}^{\mathrm{T}}\boldsymbol{l}_1 = l_1'$ and $\boldsymbol{e}^{\mathrm{T}}\boldsymbol{l}_2 = l_2'$. Since $\boldsymbol{e}^{\mathrm{T}}\boldsymbol{f} = 1$ by construction, the explicit mapping from $M' = 1$ to an equivalent M-species system for these mixing coefficients is

$$\boldsymbol{l}_1 = \boldsymbol{f}l_1', \qquad \boldsymbol{l}_2 = \boldsymbol{f}l_2' \tag{4.100}$$

By comparing gradients like (4.98) at nonzero t or $\check{p}$ one shows easily that also $\boldsymbol{v}_0 = \boldsymbol{f}v_0'$, $\boldsymbol{n}_3 = \boldsymbol{f}n_3'$ with analogous results for all other vector mixing coefficients. For the matrix $\boldsymbol{q}_0$ one notes that $\boldsymbol{q}_0\check{\boldsymbol{\mu}}$ must also be proportional to $\boldsymbol{f}$, otherwise one could change the direction of the gradient (4.98) by moving around state space and do so in a different way for the different scaling variables, thus destroying the proportionality (4.97). By symmetry

of $\boldsymbol{q}_0$ and the same normalisation argument as above one then finds

$$\boldsymbol{q}_0 = \boldsymbol{f} q_0' \boldsymbol{f}^{\mathrm{T}} \tag{4.101}$$

in terms of the mixing coefficient q_0' of the original $M' = 1$ system. Analogous results apply for the other matrix mixing coefficients.

The generalisation of the above reasoning to $M' > 1$ is not difficult. If we define for each i the vector $\check{\boldsymbol{\rho}}_i$ as the one collecting the densities of the corresponding labelled subspecies $j \in i$, with all other entries set to zero, then the chemical potential changes that leave the physical state of the system invariant obey $\check{\boldsymbol{\rho}}_i^{\mathrm{T}} d\check{\boldsymbol{\mu}} = 0$ for all i. The three scaling variable gradients $[(\partial\tilde{p}/\partial\check{\boldsymbol{\mu}})$, etc.] must then be linear combinations of the vectors $\check{\boldsymbol{\rho}}_i$ at each state point. At the critical point these vectors are proportional to the vectors $\boldsymbol{f}_i$, defined such that $\boldsymbol{f}_i$ collects the nonzero entries of $\boldsymbol{f}$ that correspond to original species i. One thus has, taking $\boldsymbol{l}_1$ as an example

$$\boldsymbol{l}_1 = \sum_i L_i \boldsymbol{f}_i \tag{4.102}$$

The coefficients L_i can be worked out from the density sum constraints (4.90) again, giving

$$\boldsymbol{l}_1 = \sum_i \boldsymbol{f}_i (\boldsymbol{l}_1')_i / f_i' \tag{4.103}$$

where the parent distribution in the original system, $f_i' = \boldsymbol{e}^{\mathrm{T}} \boldsymbol{f}_i = \sum_{j \in i} f_j$, naturally emerges as normaliser. If we define a rectangular $M \times M'$ 'inflation' matrix by

$$S_{ji} = f_j / f_i' \qquad \text{for } j \in i \tag{4.104}$$

and $S_{ji} = 0$ otherwise, then the relation (4.102) can be written in the simple matrix form

$$\boldsymbol{l}_1 = \boldsymbol{S} \boldsymbol{l}_1' \tag{4.105}$$

This then applies to all vector mixing coefficients. Matrix mixing coefficients are inflated from M' to M similarly by

$$\boldsymbol{q}_0 = \boldsymbol{S}\,\boldsymbol{q}_0'\,\boldsymbol{S}^{\mathrm{T}} \tag{4.106}$$

etc. This transformation would then generalise to tensorial mixing coefficients in the obvious way, which would arise if one chose to include third or higher order terms in the mapping equations (4.4)–(4.6). In essence the transformation ensures that the M chemical potentials $\check{\boldsymbol{\mu}}$ in the larger system enter all physical properties only through the M' weighted combinations $\boldsymbol{S}^{\mathrm{T}}\check{\boldsymbol{\mu}}$, consistent with the invariance condition (4.96).

Beyond conceptual use in understanding the monodisperse limit, the above method could also be deployed in fitting mixing coefficients to numerical data for the critical behaviour of polydisperse systems. In principle a description with M as large as possible is preferred as it would capture the most detail; on the other hand, the computational costs will increase with the number of fitting parameters and hence with M (see Section 4.D). One could therefore envisage initially fitting parameters for some small M' and then using the method above to map these to an equivalent representation with larger M. This should then constitute a suitable initial point for further parameter optimisation in the larger description. The process could be repeated in an iterative manner, building up increasingly refined data-driven descriptions of the critical behaviour of a polydisperse system.

4.D Fitted mixing coefficients

In order to find fitted mixing coefficients, we first created a forward routine that, for any given set of mixing coefficients, solves the full system of equations (mapping equations and dilution line constraint) numerically to produce predictions for the cloud and shadow curves. The root mean squared error between these predictions and those Lennard-Jones data points from Ref. [114] that were not too far from the CP was then used as the objective function, to be minimised across all possible assignments of mixing coefficients. Only $\boldsymbol{l}_0$ is taken as fixed because as shown in the main text it has to equal to the normalised parent distribution $\boldsymbol{f}$.

Even for the smallest mixture description, $M = 2$, this still leaves 38 linear and quadratic mixing coefficients to be found; for general M this number is $\left(26 + 19M + 3M^2\right)/2$, bearing in mind that each mixing vector contributes M parameters and each (symmetric) mixing matrix $M(M+1)/2$. Minimisation of the root mean square objective over such a large parameter space proved difficult, in particular due to the presence of a large number of local minima. We therefore chose to simplify the set of mixing coefficients by keeping all first order coefficients plus $\boldsymbol{q}_0$, and setting the remaining coefficients of quadratic terms to zero. The choice of $\boldsymbol{q}_0$ was driven by the fact that, as explained in Appendix 4.A, the presence of this term is essential in order to have a consistent theory that can properly describe fractionation. [Initially we observed that $\boldsymbol{q}_0$ is the only matrix that turns up when expressing the slope in Eq. (4.42) in terms of the original, mixing coefficients. This fact led us to predict that $\boldsymbol{q}_0$ would be important in the polydisperse critical phase behaviour. In fact if one includes only first-order mixing coefficients then fractionation may be wrongly taken into account. We know that this occurs for sure when $M > 3$, as discussed in Section 4.2.] Of course we expect that in reality the other quadratic mixing coefficients will not be exactly zero but, as shown in Fig. 4.1, setting them to zero as we did is reasonable given that it still allows us to fit the simulation data well. For the same reason we fixed the amplitude parameter in the scaling relation (4.3) to $Q = 1$.

Given the considerations above we limited ourselves to fitting mixing coefficients for a mixture description with the smallest non-trivial value, $M = 2$. One then has to make an appropriate assignment of the effective parent distribution $\boldsymbol{f}$ for this chosen M. The actual distribution of the polydisperse attributed used in Ref. [114] was roughly bell-shaped, more specifically a Schulz distribution with a standard deviation of 14% of the mean, limited to the range $0.5 < \sigma < 1.4$ and then renormalised appropriately. To find $\boldsymbol{f}$ we formed M bins evenly spaced across the σ-range and then integrated the probability within each bin. For $M = 2$ this led to

$$\boldsymbol{f}^{\mathrm{T}} = \begin{bmatrix} 0.378 & 0.622 \end{bmatrix} \tag{4.107}$$

[In the above it became clear that, because of the similarly drawn composition, even the $M = 2$ numerics can be a good match to the Lennard-Jones data, even though in Ref. 114

they considered 120 bins. (One can think of our distribution as a quantitative analogue for $M = 2$ of the distribution used in Ref. 114.)] The best mixing coefficients corresponding to this choice of $\boldsymbol{f}$ were found using a combination of global optimisation using simulated annealing and local optimisation near candidate local minima. This produced the following nonzero coefficients:

$$\boldsymbol{l}_1^{\mathrm{T}} = \begin{bmatrix} -0.836 & -0.987 \end{bmatrix} \tag{4.108}$$

$$\boldsymbol{l}_2^{\mathrm{T}} = \begin{bmatrix} 1.10 & 1.05 \end{bmatrix} \tag{4.109}$$

$$\boldsymbol{q}_0 = \begin{bmatrix} 0.980 & 0.147 \\ 0.147 & 0.600 \end{bmatrix} \tag{4.110}$$

$$j_1 = 0.231, j_2 = 0.217 \tag{4.111}$$

$$k_0 = -0.599, k_2 = -0.996 \tag{4.112}$$

As explained above, all other mixing coefficients were set to zero. (Note that the numerical procedure used to obtain the fitted mixing coefficients could in principle pick up the unphysical sign for the mixing coefficients in the expansion for $\tilde{h}$. This would lead e.g. to $\nu_1 < 0$ despite our comment in Subsection 4.3.1 saying it should be positive. However, because all the numerical data generated here is in the coexistence region or on its boundary, i.e. $\tilde{h} = 0$, one could flip the sign of all the coefficients in the expansion of $\tilde{h}$, i.e. $\boldsymbol{l}_2$, j_2, and k_2, without changing any of the numerical data.)

We also considered an alternative route towards fitting mixing coefficients, where cloud and shadow curve data are first fitted to the form we find in our analytical expansions [Eqs. (4.42) and (4.82)], using arbitrary prefactors. Given our theoretical predictions that express these prefactors in terms of the mixing coefficients one could then, in a second

step, find a set of coefficients that reproduces the fitted prefactors. While this approach is a priori attractive, it proved to be computationally no simpler and also has two conceptual drawbacks. Firstly, as our analytical expansions are truncated beyond a certain order, there is a possibility that they would be accidentally used for fitting in a region where the discarded terms would be significant. Secondly, using the theoretically predicted expansions for cloud and shadow as part of the fitting procedure would have removed the possibility of testing these predictions in an unbiased manner.

Chapter 5

Conclusions

5.1 Summary of results

This thesis is concerned with how polydispersity alters the phase behaviour of fluids. In particular our theoretical set-ups are relevant for the behaviour of colloids, which are typically polydisperse in the real world. Here we investigated important phenomena that would not be present in simplified monodisperse approaches. This was done both in the context of the phase separation dynamics that proceeds after a temperature quench into the coexistence region, where we have made use of the Polydisperse Lattice-Gas model, and at equilibrium in the critical region of the phase diagram, in which case we employed Fisher's 'complete scaling' mapping approach generalised to multi-component systems.

We highlight the key conclusions from our work here, referring to the conclusion sections of the individual chapters for further detail. In Chapter 2 we provided strong theoretical evidence that, due to 'slow fractionation', (i) dense colloidal mixtures phase-separate in two stages and (ii) the denser phase contains long-lived composition heterogeneities, meaning that the actual equilibrium phase compositions may be unobservable in experiments. We have developed a two-dimensional histogram method that allows us to analyse slow fractionation effects in any phase-separating mixture, regardless of the polydispersity or number of species. In Chapter 3 we simulated colloidal mixtures phase separating after a secondary temperature quench into the two- and three-phase coexistence regions.

We found several interesting effects (mostly associated with the extent to which crowding effects can slow down composition changes), including long-lived regular arrangements of secondary domains; interrupted coarsening of primary domains; wetting of fractionated interfaces by oppositely fractionated layers; 'surface'-directed spinodal 'waves' propagating from primary domain interfaces; and filamentous morphologies arising out of secondary domains. Regarding Chapter 4, we draw attention once again to Table 4.1 where we summarise our results for the critical scaling of colloidal-like multicomponent fluids at liquid-gas equilibrium. We have found new suitable observables for detecting pressure-mixing effects and obtained the critical scaling of both conventional and new phase-diagram lines. Some of the leading exponents of the scaling formulas that we have obtained and verified numerically turn out to be Fisher-renormalised, as in Ising systems with 'impurities' or 'hidden fields'.

5.2 Future work

We now discuss possible directions for future work, picking up on and extending the ideas described in Sections 2.6, 3.5, and 4.8. On the dynamics front, there remains considerable scope for extending the understanding of slow fractionation in phase-separating colloids that we have developed. As discussed in Section 2.6, we would like to investigate slow fractionation effects in a dense phase-separating polydisperse lattice-gas via Monte Carlo simulations instead of using a kinetic mean-field theory. The reason is that in the Monte Carlo case we will be able to see both 'nucleation and growth' and non-mean-field effects. (Ref. [36] would be useful here in providing the relevant equilibrium properties, while Refs. [65,66] discuss somewhat similar dynamical simulations.) It would be interesting therefore to revisit the dynamics in the various phase diagram regions defined by the quenched and annealed versions of the spinodal and cloud curves. In particular one could look at the competition between spinodal decomposition and 'nucleation and growth' mechanisms. In fact, by setting up such a Monte Carlo simulation study, we would have a more general playground for investigating slow fractionation effects. Importantly, we would still be able to make use of the two-dimensional histograms (which can be meaningfully plotted even for arbitrary number of particle species, as we showed in Chapter 2) to analyse the

dynamics. In summary, the initial questions would be: how does 'nucleation and growth' alter fractionation effects? How close to the actual equilibrium phase compositions does one get after long waiting times from a quench into the metastable region? What are the non-mean-field effects?

One could also study off-lattice effects on slow fractionation in phase-separating mixtures, asking similar questions there to those described above for lattice situations. One of the off-lattice systems to simulate could be a mixture of polymer and binary colloids [126]. For this system it would be interesting to compare with a dynamical density functional theory in the continuum, including noise [72]. The simulation could use a hard sphere plus Asakura-Oosawa (AO) potential and simulate a canonical ensemble using Langevin dynamics. As the hard sphere part of the potential would require complex adaptive time step mechanisms to capture all collisions, one might opt instead for a continuous pseudo-hard-sphere potential based on a cut-and-shifted Mie (generalised Lennard-Jones) potential with exponents, say, $(50, 49)$ as in Ref. [127].

It would also be relevant to investigate how more complex colloidal systems are affected by slow fractionation as they phase separate. Considering e.g. colloids with competing interactions, we might find an even greater variety of dynamical scenarios. This setting could be probed by considering the PLG model plus second nearest neighbour repulsive interactions. On the basis of such competing interactions one would expect to see a state with undamped periodic density fluctuations, indicating a transition to cluster or striped phases (microphase separation) [128–130]. Considering instead colloids with anisotropic interactions, one could work with either a lattice gas of Janus particles [131] or the PLG model equipped with anisotropic interactions between particles that are characterised by a finite number of orientations, similarly to the lattice-gas model of solvent plus binary mixture used in Ref. [132] (even though in this model only diagonally neighbouring particles interact anisotropically).

In a further extension beyond the context of Chapter 2 one could investigate the effects of inhomogeneous cooling. In Ref. [133] it has been shown that pattern formation can be controlled by using a phase-separation trigger propagating outwards from a point. A range of transient patterns has been found, including a random droplet pattern (similar

to what we have in Chapter 2), a concentric pattern and a dendritic pattern. (See e.g. Fig. 5.1 from Ref. [133].) The occurrence of each of these patterns depends on the speed at which the trigger propagates. One would expect, therefore, that slow-fractionation effects will also play an important role in the pattern formation. In practice we could proceed from Chapter 2 by simply making the temperature lower (than the spinodal temperature) within a circular portion of the system; the radius of this region would then be set to increase linearly in time. The proportionality constant for this increase would provide a new free parameter to play with, together with the particle-particle exchange frequency w_s.

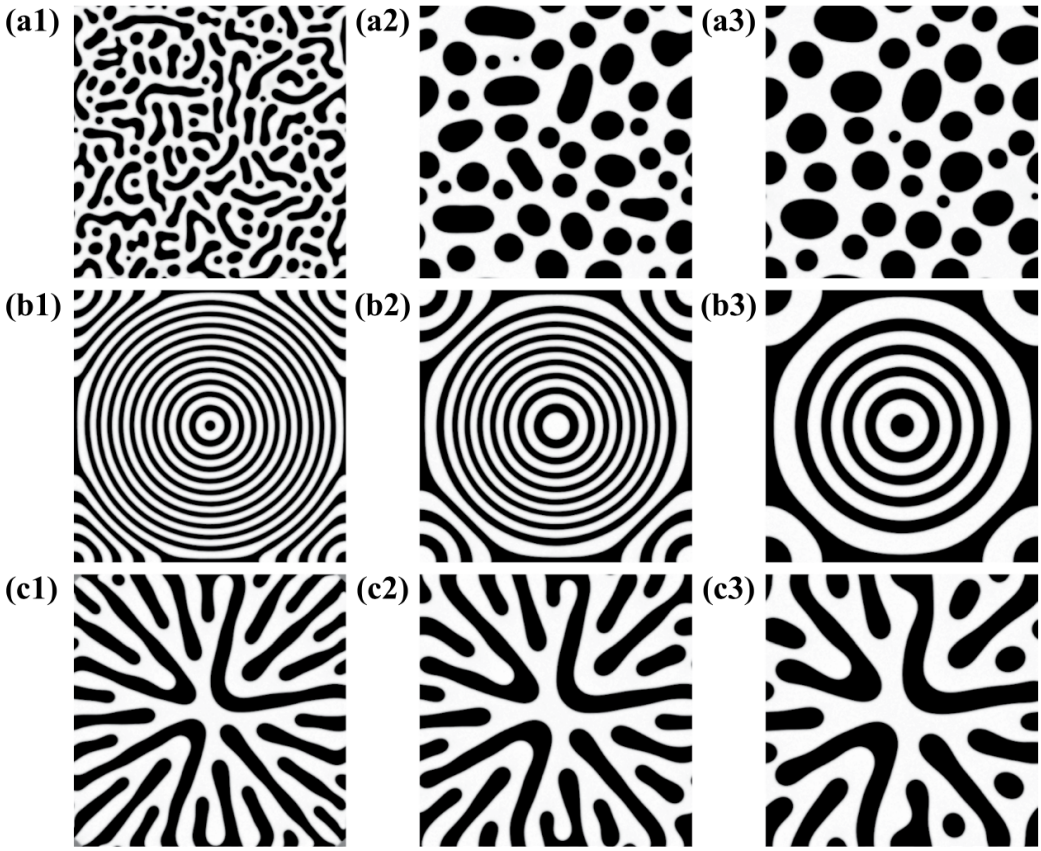

FIGURE 5.1: Time evolution of transient patterns with a propagated trigger from the centre. (a) Time evolution of the random droplet pattern. (b) Time evolution of the concentric circles pattern when the trigger speed is lower than in (a). (c) Time evolution of the dendritic pattern when the trigger speed is even lower. All images correspond to times after the trigger has reached the end of the simulation box. Figure by Rei Kurita. Source: Scientific Reports, volume 7, Article number: 6912 (2017). Link to material: https://www.nature.com/articles/s41598-017-07352-z. Under a Creative Commons Attribution 4.0 International License. Link to license: http://creativecommons.org/licenses/by/4.0/. The caption has been adapted but the figure has been taken from the original publication PDF without changes.

As discussed in Chapter 3, in the study of phase separation following a deep secondary quench we would like to find out how the occurrence or not of slow composition changes affects the time length of the coarsening-interruption plateau. Furthermore, it would be interesting to understand quantitatively how primary coarsening is restored as we approach the asymptotic regime. Also, a consistent incorporation of nucleation and growth could be even more important for the analysis of secondary quenches: in the high temperature case, where we have seen the existence of the 'dead zone', it is possible that nucleation and growth could end up destroying that effect; moreover, as discussed above the presence of spinodal waves depends on the bulk noise strength at the time of a secondary quench. As regards the case of a secondary quench into the three-phase region, we would like to investigate whether the filamentous state is also reached for $w_s = 0$ and how this is approached in comparison to the $w_s = 1$ case. One could then investigate this 'three-phase' nonequilibrium problem by implementing controlled initial geometries of the primary interfaces that include e.g. protuberances; we would thus be able to trace the filaments' formation more easily, and to study how two primary liquid domains become connected through a filament. Finally, it might be interesting to see what quantitative or – less likely, qualitative – effects on the physics presented in Chapter 3 would result from changing to an off-lattice setting.

On the equilibrium criticality front, one possible future direction would be the study of critical finite-size scaling. As a starting point one could use Ref. [134], where the author calculates the finite-size scaling for binary mixtures via a field-mixing analysis and compares with Monte Carlo simulations. This would be aided by the one-component fluid study in Ref. [135], which incorporates pressure-mixing effects. The next step therefore would be to understand in detail how such an approach might be extended to multi-component colloids. Because of pressure mixing, the critical density estimator of the one-component case, $n_c(L)$, gains a leading term $L^{-2\beta/\nu}$ (when $L \to \infty$) that dominates the previous $L^{-(1-\alpha)/\nu}$ term, where L is the linear size of the simulation box and ν is the correlation length critical exponent. This is analogous to what happens for the diameter of one-component fluids when pressure mixing is turned on. Therefore one could expect that in the case of multi-component colloids the result would change further into $L^{-2\tilde{\beta}/\nu}$,

similarly to what happens in our calculations in Chapter 4. This could help to quantify pressure mixing effects in simulations of polydisperse colloids. Also, we would expect an understanding of such finite-size scaling to be useful when studying the thermodynamic Casimir effect [136–138] in multi-component colloids.

Another possible route would consist in extending Refs. [122, 124], where the critical behaviour of the refractive index is studied for weakly compressible binary mixtures, to allow for a generic number of species and arbitrary compressibility, with controlled overall density, composition and temperature. This would be done by introducing the electric field as a fluid variable into the mapping between the Ising fields and the other fluid variables, i.e. temperature, pressure and species chemical potentials. Then a comparison could be made with the critical behaviour of the refractive index as derived from the Lorentz-Lorenz equation generalised to multi-component systems. This is an approximate equation that relates the refractive index to the composition densities [122]. In particular, fractionation effects could be investigated.

Returning to a context without electric fields, one could look at the Tolman's length (δ) of a droplet of polydisperse colloidal fluid. It measures the extent by which the surface tension (σ) of the droplet deviates from its planar value and is defined as a curvature-correction coefficient in σ [120], that is

$$\sigma(R) = \sigma_\infty \left(1 - \frac{2\delta}{R} + \dots\right) \tag{5.1}$$

where R is the droplet radius, taken equal to the radius of the surface of tension, and σ_∞ is the planar-interface surface tension. The result for the critical behaviour of the Tolman's length when pressure mixing is considered [120] becomes $\delta \sim t^{\beta-\nu} + t^{1-\alpha-\beta-\nu}$, instead of the previous $\delta \sim t^{1-\alpha-\beta-\nu}$ Notice that the leading exponent changes from -0.065 to -0.304, with $\nu = 0.630$. One could expect that in our multi-component colloidal case the leading exponent would be $2\tilde{\beta} - \beta - \nu = -0.224$, as a result of Fisher renormalisation.

The phase behaviour of a colloid with a small spread of particle sizes is also very interesting, in particular in contexts where careful sample preparation can reduce polydispersity to around 5%, but not eliminate it [50]. Usefully, their phase behaviour can be related

perturbatively to that of their monodisperse counterparts. It has been shown that this approach can remain well-behaved near the critical point [44], despite previous approaches breaking down in the critical region [37]. Therefore one could aim to compare our results for the critical scaling of arbitrary polydisperse systems in Chapter 4 with their weakly-polydisperse counterparts, with the aim of better understanding the monodisperse-to-polydisperse crossover near the CP. To do so, one would replace the Landau-like expansion of the free energy near criticality used in Ref. [44] by a non-mean-field near-critical free energy obtained from what has been presented in Chapter 4. This would be plugged into the perturbation theory equations from Ref. [44]; these are suitable for cloud and shadow curves and so in order to obtain other curves as we did here additional developments would need to be made, but still along the lines of [44]. In pursuing this route, it could be useful to incorporate the prescriptions for mapping between polydisperse and monodisperse systems, such as our mixing coefficients mapping in Appendix 4.C as well as the mapping in the opposite direction (i.e. from more to fewer species) developed in Ref. [139].

Bibliography

[1] Peter Sollich and Nigel B Wilding. Polydispersity induced solid–solid transitions in model colloids. *Soft Matter*, 7(9):4472–4484, 2011.

[2] Stefan Auer and Daan Frenkel. Suppression of crystal nucleation in polydisperse colloids due to increase of the surface free energy. *Nature*, 413(6857):711–713, 2001.

[3] SM Liddle, T Narayanan, and WCK Poon. Polydispersity effects in colloid–polymer mixtures. *Journal of Physics: Condensed Matter*, 23(19):194116, 2011.

[4] WCK Poon. The physics of a model colloid–polymer mixture. *Journal of Physics: Condensed Matter*, 14(33):R859, 2002.

[5] Priti S Mohanty, Divya Paloli, Jérôme J Crassous, Emanuela Zaccarelli, and Peter Schurtenberger. Effective interactions between soft-repulsive colloids: Experiments, theory, and simulations. *The Journal of Chemical Physics*, 140(9):094901, 2014.

[6] Peng Tan, Ning Xu, and Lei Xu. Visualizing kinetic pathways of homogeneous nucleation in colloidal crystallization. *Nature Physics*, 10(1):73–79, 2014.

[7] Emanuela Zaccarelli, Siobhan M Liddle, and Wilson CK Poon. On polydispersity and the hard sphere glass transition. *Soft Matter*, 11(2):324–330, 2015.

[8] Constantinos V Chrysikopoulos and Vasiliki I Syngouna. Effect of gravity on colloid transport through water-saturated columns packed with glass beads: Modeling and experiments. *Environmental Science & Technology*, 48(12):6805–6813, 2014.

[9] E Van den Pol, AV Petukhov, DME Thies-Weesie, DV Byelov, and GJ Vroege. Experimental realization of biaxial liquid crystal phases in colloidal dispersions of board-like particles. *Physical Review Letters*, 103(25):258301, 2009.

[10] M. A. Cohen Stuart, J. M. H. M. Scheutjens, and G. J. Fleer. Polydispersity effects and the interpretation of polymer adsorption isotherms. *Journal of Polymer Science: Polymer Physics Edition*, 18(3):559–573, 1980.

[11] S Belli, A Patti, M Dijkstra, and R Van Roij. Polydispersity stabilizes biaxial nematic liquid crystals. *Physical Review Letters*, 107(14):148303, 2011.

[12] TJ Sluckin. Polydispersity in liquid crystal systems. *Liquid Crystals*, 6(1):111–131, 1989.

[13] Peter Sollich. Nematic-nematic demixing in polydisperse thermotropic liquid crystals. *The Journal of Chemical Physics*, 122(21):214911, 2005.

[14] M. Rogosić, H.J. Mencer, and Z. Gomzi. Polydispersity index and molecular weight distributions of polymers. *European Polymer Journal*, 32(11):1337 – 1344, 1996.

[15] Justine Viéville, Matthieu Tanty, and Marc-André Delsuc. Polydispersity index of polymers revealed by dosy nmr. *Journal of Magnetic Resonance*, 212(1):169–173, 2011.

[16] RML Evans, DJ Fairhurst, and WCK Poon. Universal law of fractionation for slightly polydisperse systems. *Physical Review Letters*, 81(6):1326, 1998.

[17] Peter Sollich. Predicting phase equilibria in polydisperse systems. *Journal of Physics: Condensed Matter*, 14(3):R79, 2002.

[18] Paul Bartlett. Soft matter in the real world. *Physics World*, 11(6):23, 1998.

[19] NE Berger, RJ Lucas, and V Twersky. Polydisperse scattering theory and comparisons with data for red blood cells. *The Journal of the Acoustical Society of America*, 89(3):1394–1401, 1991.

[20] M José-Yacamán, Luis Rendón, Jesús Arenas, and Mari Carmen Serra Puche. Maya blue paint: An ancient nanostructured material. *Science*, 273(5272):223, 1996.

[21] Skelte G Anema. Effect of milk solids concentration on whey protein denaturation, particle size changes and solubilization of casein in high-pressure-treated skim milk. *International Dairy Journal*, 18(3):228–235, 2008.

[22] AL Johnson. Particle size distribution in clays. *Clays and Clay Minerals*, (1):89–91, 1952.

[23] Andrei V Lavrinenko, Wendel Wohlleben, and Reinhold J Leyrer. Influence of imperfections on the photonic insulating and guiding properties of finite si-inverted opal crystals. *Optics Express*, 17(2):747–760, 2009.

[24] Yuting Li, Steven P Armes, Xiaoping Jin, and Shiping Zhu. Direct synthesis of well-defined quaternized homopolymers and diblock copolymers via atrp in protic media. *Macromolecules*, 36(22):8268–8275, 2003.

[25] Seth Fraden. Phase transitions in colloidal suspensions of virus particles. In *Observation, Prediction and Simulation of Phase Transitions in Complex Fluids*, pages 113–164. Springer, 1995.

[26] Domenico Gazzillo and Achille Giacometti. Effects of polydispersity and anisotropy in colloidal and protein solutions: An integral equation approach. *Interdisciplinary Sciences: Computational Life Sciences*, 3(4):251–265, 2011.

[27] P Vera, V Gallardo, J Salcedo, and AV Delgado. Colloidal stability of a pharmaceutical latex: Experimental determinations and theoretical predictions. *Journal of Colloid and Interface Science*, 177(2):553–560, 1996.

[28] Min-Hye Park, Tae-Hwan Lee, Bo-Mi Lee, Jin Hur, and Dae-Hee Park. Spectroscopic and chromatographic characterization of wastewater organic matter from a biological treatment plant. *Sensors*, 10(1):254–265, 2009.

[29] Emilia Szymańska and Katarzyna Winnicka. Stability of Chitosan—A challenge for pharmaceutical and biomedical applications. *Marine Drugs*, 13(4):1819–1846, 2015.

[30] Marilyn Rayner and Petr Dejmek. *Engineering aspects of food emulsification and homogenization*. CRC Press, 2015.

[31] JJ Lietor-Santos, C Kim, ML Lynch, A Fernandez-Nieves, and DA Weitz. The role of polymer polydispersity in phase separation and gelation in colloid- polymer mixtures. *Langmuir*, 26(5):3174–3178, 2009.

[32] Jarkko Ahonen. Transport coefficients in the early universe. *Physical Review D*, 59(2):023004, 1998.

[33] David Langlois and Sébastien Renaux-Petel. Perturbations in generalized multi-field inflation. *Journal of Cosmology and Astroparticle Physics*, 2008(04):017, 2008.

[34] John Joseph Williamson. *The kinetics of phase transitions in polydisperse systems*. University of Leeds, 2013.

[35] Pablo de Castro and Peter Sollich. Phase separation dynamics of polydisperse colloids: A mean-field lattice-gas theory. *Physical Chemistry Chemical Physics*, 19:22509–22527, 2017.

[36] Nigel B. Wilding, Peter Sollich, and Matteo Buzzacchi. Polydisperse lattice-gas model. *Physical Review E*, 77:011501, 2008.

[37] R. M. L. Evans. Perturbative polydispersity: Phase equilibria of near-monodisperse systems. *The Journal of Chemical Physics*, 114(4):1915–1931, 2001.

[38] D. J. Fairhurst and R. M. L. Evans. De-mixing of polydisperse fluids: Experimental test of a universal relation. *Colloid and Polymer Science*, 282(7):766–769, 2004.

[39] Moreno Fasolo and Peter Sollich. Fractionation effects in phase equilibria of polydisperse hard-sphere colloids. *Physical Review E*, 70(4):041410, 2004.

[40] Peter Sollich and Nigel B Wilding. Crystalline phases of polydisperse spheres. *Physical Review Letters*, 104(11):118302, 2010.

[41] Paul Bartlett and Patrick B Warren. Reentrant melting in polydispersed hard spheres. *Physical Review Letters*, 82(9):1979, 1999.

[42] RML Evans and CB Holmes. Diffusive growth of polydisperse hard-sphere crystals. *Physical Review E*, 64(1):011404, 2001.

[43] John J. Williamson and R. Mike L. Evans. The effects of polydispersity and metastability on crystal growth kinetics. *Soft Matter*, 9:3600–3612, 2013.

[44] Peter Sollich. Weakly polydisperse systems: Perturbative phase diagrams that include the critical region. *Physical Review Letters*, 100(3):035701, 2008.

[45] Moreno Fasolo and Peter Sollich. Equilibrium phase behavior of polydisperse hard spheres. *Physical Review Letters*, 91(6):068301, 2003.

[46] Peter Sollich and Michael E Cates. Projected free energies for polydisperse phase equilibria. *Physical Review Letters*, 80(7):1365, 1998.

[47] Patrick B Warren. Combinatorial entropy and the statistical mechanics of polydispersity. *Physical Review Letters*, 80(7):1369, 1998.

[48] Peter Sollich, Patrick B Warren, and Michael E Cates. Moment free energies for polydisperse systems. *Advances in Chemical Physics*, 116:265–336, 2001.

[49] Patrick B. Warren. Phase transition kinetics in polydisperse systems. *Physical Chemistry Chemical Physics*, 1:2197–2202, 1999.

[50] Peter N Pusey and W Van Megen. Phase behaviour of concentrated suspensions of nearly hard colloidal spheres. *Nature*, 320(6060):340–342, 1986.

[51] N. Clarke. Early stages of phase separation from polydisperse polymer mixtures. *The European Physical Journal E*, 4(3):327–336, 2001.

[52] I. Pagonabarraga and M. E. Cates. Dynamics of polydisperse polymer mixtures. *Macromolecules*, 36(3):934–949, 2003.

[53] M. Plapp and J.-F. Gouyet. Surface modes and ordered patterns during spinodal decomposition of an *ABv* model alloy. *Physical Review Letters*, 78:4970–4973, 1997.

[54] M. Plapp and J.-F. Gouyet. Spinodal decomposition of an abv model alloy: Patterns at unstable surfaces. *The European Physical Journal B - Condensed Matter and Complex Systems*, 9(2):267–282, 1999.

[55] J. J. Williamson and R. M. L. Evans. Measuring local volume fraction, long-wavelength correlations, and fractionation in a phase-separating polydisperse fluid. *The Journal of Chemical Physics*, 141(16):164901, 2014.

[56] J. J. Williamson and R. M. L. Evans. Spinodal fractionation in a polydisperse square-well fluid. *Physical Review E*, 86:011405, 2012.

[57] Siobhan Mary Liddle. Polydispersity effects on colloidal phase transitions and kinetic arrest. 2014.

[58] AL Kuzemsky. Variational principle of bogoliubov and generalized mean fields in many-particle interacting systems. *International Journal of Modern Physics B*, 29(18):1530010, 2015.

[59] Richard P Feynman. *Statistical mechanics: A set of lectures*. Hachette UK, 1998.

[60] Werner Borchard, Stephanie Frahn, and Volker Fischer. Determination of cloud-point, shadow and other coexistence curves in multicomponent systems from measurements of phase volume ratios. *Macromolecular Chemistry and Physics*, 195(10):3311–3324, 1994.

[61] Sanjay Puri. *Kinetics of Phase Transitions*, pages 1–61. CRC Press, 2015/06/27 2009.

[62] Margit T Rätzsch, Horst Kehlen, Dieter Browarzik, and Michael Schirutschke. Cloud-point curve for the system copoly (ethylene-vinyl acetate) plus methyl acetate. Measurement and prediction by continuous thermodynamics. *Journal of Macromolecular Science—Chemistry*, 23(11):1349–1361, 1986.

[63] J-F Gouyet, Mathis Plapp, W Dieterich, and P Maass. Description of far-from-equilibrium processes by mean-field lattice gas models. *Advances in Physics*, 52(6):523–638, 2003.

[64] John R Edison. Modeling the relaxation dynamics of fluids in nanoporous materials. 2012.

[65] Kumela Tafa, Sanjay Puri, and Deepak Kumar. Kinetics of phase separation in ternary mixtures. *Physical Review E*, 64(5):056139, 2001.

[66] John R Edison and Peter A Monson. Modeling relaxation processes for fluids in porous materials using dynamic mean field theory: An application to partial wetting. *Journal of Low Temperature Physics*, 157(3-4):395–409, 2009.

[67] A.J. Bray. Theory of phase-ordering kinetics. *Advances in Physics*, 43(3):357–459, 1994.

[68] Pierre C Hohenberg and Bertrand I Halperin. Theory of dynamic critical phenomena. *Reviews of Modern Physics*, 49(3):435, 1977.

[69] John W Cahn and John E Hilliard. Free energy of a nonuniform system. I. Interfacial free energy. *The Journal of Chemical Physics*, 28(2):258–267, 1958.

[70] Umberto Marini Bettolo Marconi and Pedro Tarazona. Dynamic density functional theory of fluids. *The Journal of Chemical Physics*, 110(16):8032–8044, 1999.

[71] Andrew J Archer. Dynamical density functional theory for molecular and colloidal fluids: A microscopic approach to fluid mechanics. *The Journal of Chemical Physics*, 130(1):014509, 2009.

[72] Andrew J Archer. Dynamical density functional theory: Binary phase-separating colloidal fluid in a cavity. *Journal of Physics: Condensed Matter*, 17(10):1405, 2005.

[73] Q. Bronchart, Y. Le Bouar, and A. Finel. New coarse-grained derivation of a phase field model for precipitation. *Physical Review Letters*, 100:015702, 2008.

[74] Robert L Jack and Johannes Zimmer. Geometrical interpretation of fluctuating hydrodynamics in diffusive systems. *Journal of Physics A: Mathematical and Theoretical*, 47(48):485001, 2014.

[75] Lorenzo Bertini, Alberto De Sole, Davide Gabrielli, Giovanni Jona-Lasinio, and Claudio Landim. Macroscopic fluctuation theory. *Reviews of Modern Physics*, 87(2):593, 2015.

[76] David S Dean. Langevin equation for the density of a system of interacting Langevin processes. *Journal of Physics A: Mathematical and General*, 29(24):L613, 1996.

[77] Bongsoo Kim, Kyozi Kawasaki, Hugo Jacquin, and Frédéric van Wijland. Equilibrium dynamics of the Dean-Kawasaki equation: Mode-coupling theory and its extension. *Physical Review E*, 89(1):012150, 2014.

[78] L. Sarkisov, , and P. A. Monson*. Modeling of adsorption and desorption in pores of simple geometry using molecular dynamics. *Langmuir*, 17(24):7600–7604, 2001.

[79] Hyung-June Woo and P. A. Monson. Phase behavior and dynamics of fluids in mesoporous glasses. *Physical Review E*, 67:041207, 2003.

[80] J. R. Edison and P. A. Monson. Dynamic mean field theory for lattice gas models of fluid mixtures confined in mesoporous materials. *Langmuir*, 29(45):13808–13820, 2013. PMID: 24102541.

[81] M. Cristina Marchetti, Yaouen Fily, Silke Henkes, Adam Patch, and David Yllanes. Minimal model of active colloids highlights the role of mechanical interactions in controlling the emergent behavior of active matter. *Current Opinion in Colloid and Interface Science*, 21:34 – 43, 2016.

[82] Matteo Buzzacchi, Nigel B. Wilding, and Peter Sollich. Wetting transitions in polydisperse fluids. *Physical Review Letters*, 97:136104, 2006.

[83] Silvio Franz and Fabio Lucio Toninelli. Finite-range spin glasses in the Kac limit: Free energy and local observables. *Journal of Physics A: Mathematical and General*, 37(30):7433, 2004.

[84] T. C. B. McLeish, M. E. Cates, J. S. Higgins, P. D. Olmsted, M. E. Cates, J. Vollmer, A. Wagner, and D. Vollmer. Phase separation in binary fluid mixtures with continuously ramped temperature. *Philosophical Transactions of the Royal Society of London. Series A: Mathematical, Physical and Engineering Sciences*, 361(1805):793–807, 2003.

[85] Awaneesh Singh, A. Mukherjee, H. M. Vermeulen, G. T. Barkema, and Sanjay Puri. Control of structure formation in phase-separating systems. *The Journal of Chemical Physics*, 134(4):044910, 2011.

[86] Li-Tang Yan and Xu-Ming Xie. Lamellar morphology induced by two-step surface-directed spinodal decomposition in binary polymer mixture films. *The Journal of Chemical Physics*, 128(3):034901, 2008.

[87] Marcin Fialkowski and Robert Holyst. Quench–jump sequence in phase separation in polymer blends. *The Journal of Chemical Physics*, 117(4):1886–1892, 2002.

[88] Iulia Podariu and Amitabha Chakrabarti. Computer simulation of phase separation under a double temperature quench. *The Journal of Chemical Physics*, 126(15):154509, 2007.

[89] Ian C. Henderson and Nigel Clarke. Two-step phase separation in polymer blends. *Macromolecules*, 37(5):1952–1959, 2004.

[90] Y. C. Li, R. P. Shi, C. P. Wang, X. J. Liu, and Y. Wang. Predicting microstructures in polymer blends under two-step quench in two-dimensional space. *Physical Review E*, 83:041502, Apr 2011.

[91] Takeji Hashimoto, Masaki Hayashi, and Hiroshi Jinnai. Two-step phase separation of a polymer mixture. I. New scaling analysis for the main scattering peak. *The Journal of Chemical Physics*, 112(15):6886–6896, 2000.

[92] Masaki Hayashi, Hiroshi Jinnai, and Takeji Hashimoto. Two-step phase separation of a polymer mixture. II. Time evolution of structure factor. *The Journal of Chemical Physics*, 112(15):6897–6909, 2000.

[93] Hajime Tanaka. Double phase separation in a confined, symmetric binary mixture: Interface quench effect unique to bicontinuous phase separation. *Physical Review Letters*, 72:3690–3693, 1994.

[94] Tomoo Sigehuzi and Hajime Tanaka. Coarsening mechanism of phase separation caused by a double temperature quench in an off-symmetric binary mixture. *Physical Review E*, 70:051504, 2004.

[95] Yibao Li, Yongho Choi, and Junseok Kim. Computationally efficient adaptive time step method for the Cahn–Hilliard equation. *Computers and Mathematics with Applications*, 73(8):1855–1864, 2017.

[96] I.M. Lifshitz and V.V. Slyozov. The kinetics of precipitation from supersaturated solid solutions. *Journal of Physics and Chemistry of Solids*, 19(1):35 – 50, 1961.

[97] David A. Huse. Corrections to late-stage behavior in spinodal decomposition: Lifshitz-Slyozov scaling and monte carlo simulations. *Physical Review B*, 34:7845–7850, 1986.

[98] Peter Streitenberger. Analytical description of phase coarsening at high volume fractions. *Acta Materialia*, 61(13):5026 – 5035, 2013.

[99] Li-Tang Yan and Xu-Ming Xie. Numerical simulation of surface effects on spinodal decomposition in polymer binary mixture: Quench depth dependence. *Macromolecules*, 39(6):2388–2397, 2006.

[100] Jonathan Weiner, Kenneth H. Langley, and N. C. Ford. Experimental evidence for a departure from the law of the rectilinear diameter. *Physical Review Letters*, 32:879–881, 1974.

[101] ET Shimanskaya, IV Bezruchko, VI Basok, and YI Shimanskiı. Experimental determination of the critical exponent and of the asymmetric and non asymptotic corrections to the equation of the coexistence curve of Freon-113. *Soviet Physics–JETP*, 53:139, 1981.

[102] Marcos Ley-Koo and Melville S. Green. Revised and extended scaling for coexisting densities of SF_6. *Physical Review A*, 16:2483–2487, 1977.

[103] T. D. Lee and C. N. Yang. Statistical theory of equations of state and phase transitions. II. Lattice gas and Ising model. *Physical Review*, 87:410–419, 1952.

[104] C. N. Yang and C. P. Yang. Critical point in liquid-gas transitions. *Physical Review Letters*, 13:303–305, 1964.

[105] B. Widom. Equation of state in the neighborhood of the critical point. *The Journal of Chemical Physics*, 43(11):3898–3905, 1965.

[106] JJ Rehr and ND Mermin. Revised scaling equation of state at the liquid-vapor critical point. *Physical Review A*, 8(1):472, 1973.

[107] Young C Kim, Michael E Fisher, and G Orkoulas. Asymmetric fluid criticality. I. Scaling with pressure mixing. *Physical Review E*, 67(6):61506, 2003.

[108] Mikhail A. Anisimov and Jingtao Wang. Nature of asymmetry in fluid criticality. *Physical Review Letters*, 97:025703, 2006.

[109] M. W. Pestak, Raymond E. Goldstein, M. H. W. Chan, J. R. de Bruyn, D. A. Balzarini, and N. W. Ashcroft. Three-body interactions, scaling variables, and singular diameters in the coexistence curves of fluids. *Physical Review B*, 36:599–614, 1987.

[110] Jingtao Wang, Claudio A Cerdeirina, Mikhail A Anisimov, and Jan V Sengers. Principle of isomorphism and complete scaling for binary-fluid criticality. *Physical Review E*, 77(3, 1):031127, 2008.

[111] G Perez-Sanchez, P Losada-Perez, C A Cerdeirina, J V Sengers, and M A Anisimov. Asymmetric criticality in weakly compressible liquid mixtures. *The Journal of Chemical Physics*, 132(15):154502, 2010.

[112] M.Yu. Belyakov, E.E. Gorodetskii, V.D. Kulikov, A.R. Muratov, V.P. Voronov, B.A. Grigoriev, and A.N. Volkov. Anomalous properties of dew-bubble curves in the vicinity of liquid–vapor critical points. *Fluid Phase Equilibria*, 358:91–97, 2013.

[113] M Yu. Belyakov, E E Gorodetskii, V D Kulikov, V P Voronov, and B A Grigoriev. Scaled equation of state for multi-component fluids. *Chemical Physics*, 445:53–58, 2014.

[114] Nigel B. Wilding, Peter Sollich, Moreno Fasolo, and Matteo Buzzacchi. Phase behavior and particle size cutoff effects in polydisperse fluids. *The Journal of Chemical Physics*, 125(1):014908, 2006.

[115] Misaki Ozawa and Ludovic Berthier. Does the configurational entropy of polydisperse particles exist? *The Journal of Chemical Physics*, 146(1):014502, 2017.

[116] P Schofield, JD Litster, and John T Ho. Correlation between critical coefficients and critical exponents. *Physical Review Letters*, 23(19):1098, 1969.

[117] G. Sanchez, M. Meichle, and C. W. Garland. Critical heat capacity in a 3-methylpentane + nitroethane mixture near its consolute point. *Physical Review A*, 28:1647–1653, 1983.

[118] Michael E Fisher. Renormalization of Critical Exponents by Hidden Variables. *Physical Review*, 176(1):257–272, 1968.

[119] M.A Anisimov, E.E Gorodetskii, V.D Kulikov, A.A Povodyrev, and J.V Sengers. A general isomorphism approach to thermodynamic and transport properties of binary fluid mixtures near critical points. *Physica A: Statistical Mechanics and its Applications*, 220(3-4):277–324, 1995.

[120] M A Anisimov. Divergence of Tolman's length for a droplet near the critical point. *Physical Review Letters*, 98(3):035702, 2007.

[121] Patricia Losada-Perez, German Perez-Sanchez, Claudio A Cerdeirina, and Jan Thoen. Dielectric constant of fluids and fluid mixtures at criticality. *Physical Review E*, 81(4, 1):041121, 2010.

[122] Patricia Losada-Pérez, Christ Glorieux, and Jan Thoen. The critical behavior of the refractive index near liquid-liquid critical points. *The Journal of Chemical Physics*, 136(14):144502, 2012.

[123] Patricia Losada-Perez, German Perez-Sanchez, Jacobo Troncoso, and Claudio A Cerdeirina. Heat capacity anomalies along the critical isotherm in fluid-fluid phase transitions. *The Journal of Chemical Physics*, 132(15):154509, 2010.

[124] Asma Jamali and Hassan Behnejad. Critical behaviour of thermo-physical properties in weakly compressible liquid mixtures. *Physics and Chemistry of Liquids*, 52(4):519–532, 2014.

[125] Hassan Behnejad, Hashem Cheshmpak, and Asma Jamali. Isomorphic viscosity equation of state for binary fluid mixtures. *Acta Chimica Slovenica*, 62(4):754–760, 2015.

[126] Isla Zhang, Rattachai Pinchaipat, Nigel B. Wilding, Malcolm A. Faers, Paul Bartlett, Robert Evans, and C. Patrick Royall. Composition inversion in mixtures of binary colloids and polymer. *The Journal of Chemical Physics*, 148(18):184902, 2018.

[127] J. Jover, A. J. Haslam, A. Galindo, G. Jackson, and E. A. Müller. Pseudo hard-sphere potential for use in continuous molecular-dynamics simulation of spherical and chain molecules. *The Journal of Chemical Physics*, 137(14):144505, 2012.

[128] A. J. Archer, D. Pini, R. Evans, and L. Reatto. Model colloidal fluid with competing interactions: Bulk and interfacial properties. *The Journal of Chemical Physics*, 126(1):014104, 2007.

[129] J. Pekalski, A. Ciach, and N. G. Almarza. Periodic ordering of clusters and stripes in a two-dimensional lattice model. I. Ground state, mean-field phase diagram and structure of the disordered phases. *The Journal of Chemical Physics*, 140(11):114701, 2014.

[130] Soon-Chul Kim, Soong-Hyuck Suh, and Baek-Seok Seong. Microphase separations of the fluids with spherically symmetric competing interactions. *The Journal of Chemical Physics*, 137(11):114703, 2012.

[131] Danilo B Liarte and Silvio R Salinas. Bethe-lattice calculations for the phase diagram of a two-state Janus gas. *Journal of Statistical Mechanics: Theory and Experiment*, 2015(2):P02020, 2015.

[132] Yuri Lifanov, Bart Vorselaars, and David Quigley. Nucleation barrier reconstruction via the seeding method in a lattice model with competing nucleation pathways. *The Journal of Chemical Physics*, 145(21):211912, 2016.

[133] Rei Kurita. Control of pattern formation during phase separation initiated by a propagated trigger. *Scientific Reports*, 7(1):6912, 2017.

[134] Nigel B. Wilding. Critical end point behavior in a binary fluid mixture. *Physical Review E*, 55:6624–6631, 1997.

[135] Young C Kim and Michael E Fisher. Fluid critical points from simulations: The Bruce-Wilding method and Yang-Yang anomalies. *The Journal of Physical Chemistry B*, 108(21):6750–6759, 2004.

[136] C. Hertlein, L. Helden, A. Gambassi, S. Dietrich, and C. Bechinger. Direct measurement of critical Casimir forces. *Nature*, 451(7175):172, 2008.

[137] Andrea Gambassi. The Casimir effect: From quantum to critical fluctuations. *Journal of Physics: Conference Series*, 161(1):012037, 2009.

[138] A. Gambassi, A. Maciolek, C. Hertlein, U. Nellen, L. Helden, C. Bechinger, and S. Dietrich. Critical Casimir effect in classical binary liquid mixtures. *Physical Review E*, 80:061143, 2009.

[139] William M. Jacobs and Daan Frenkel. Predicting phase behavior in multicomponent mixtures. *The Journal of Chemical Physics*, 139(2):024108, 2013.